Distribution Agreement

In presenting this thesis or dissertation as a partial fulfillment of the requirements for an advanced degree from Emory University, I hereby grant to Emory University and its agents the non-exclusive license to archive, make accessible, and display my thesis or dissertation in whole or in part in all forms of media, now or hereafter known, including display on the world wide web. I understand that I may select some access restrictions as part of the online submission of this thesis or dissertation. I retain all ownership rights to the copyright of the thesis or dissertation. I also retain the right to use in future works (such as articles or books) all or part of this thesis or dissertation.

Signature:

_____ _____

Jian Wang Date

Novel Quantum Phenomena in Fractal Band Structures

Jian Wang
Doctor of Philosophy

Physics

Luiz H. Santos, Ph.D.
Advisor

Ajit Srivastava, Ph.D.
Committee Member

Carlos Sa de Melo, Ph.D.
Committee Member

Justin C. Burton, Ph.D.
Committee Member

Stefan Boettcher, Ph.D.
Committee Member

Accepted:

Kimberly J. Arriola, Ph.D.
Dean of the James T. Laney School of Graduate Studies

Date

Novel Quantum Phenomena in Fractal Band Structures

By

Jian Wang
B.S. University of Science and Technology of China, 2017

Advisor: Luiz H. Santos, Ph.D.

An abstract of
A dissertation submitted to the Faculty of the
James T. Laney School of Graduate Studies of Emory University
in partial fulfillment of the requirements for the degree of
Doctor of Philosophy
in Physics
2022

ABSTRACT

This dissertation investigates novel quantum phenomena in fractal electronic energy bands also known as Hofstadter bands. In two-dimensional lattices subject to an external perpendicular magnetic field, Hofstadter bands arise when the semi-classical cyclotron radius of the electron becomes comparable to the lattice constant. Hofstadter lattices exhibit a strong interplay between topological electronic states and lattice effects, suggesting rich quantum critical phenomena and novel phases of electronic matter beyond conventional quantum Hall physics. However, this regime had remained inaccessible due to limitations in accessing large magnetic flux per unit cell in conventional 2D materials at laboratory-scale fields, causing Hofstadter bands to collapse into degenerate Landau levels which have been much explored in the quantum Hall effect.

In recent years, the emergence of new 2D quantum platforms with nanometer scale unit cells, such as moiré materials and nano patterned superlattices, have led to experimental realization of Hofstadter bands. Consequently, Hofstadter physics has experienced a renaissance, emerging as an active frontier to investigate new fundamental questions in quantum matter. Exploiting these opportunities, this thesis develops a theoretical investigation of novel quantum phenomena in Hofstadter quantum materials, concerned with three central themes: (1) a study of the nature of topological quantum phase transitions, (2) a new framework to classify the poorly understood regime of superconductivity in fractal electronic systems and (3) an investigation of the nature of competing electronic orders, uncovering mechanisms to realize unconventional symmetry-broken and topological electronic orders driven entirely by repulsive interactions. The theoretical framework established in this thesis opens a new path toward the realization of novel quantum states, unleashing new paradigms in Hofstadter quantum materials.

Novel Quantum Phenomena in Fractal Band Structures

By

Jian Wang
B.S. University of Science and Technology of China, 2017

Advisor: Luiz H. Santos, Ph.D.

A dissertation submitted to the Faculty of the
James T. Laney School of Graduate Studies of Emory University
in partial fulfillment of the requirements for the degree of
Doctor of Philosophy
in Physics
2022

ACKNOWLEDGEMENT

First and foremost, I would like to thank my advisor Luiz Santos, who is always enthusiastic and patient in mentoring me throughout the program. I have learnt quite a few things from Luiz, including research methods, academic writing and communication skills, in particular, the idea that the best way to understand a theory is to re-establish it from scratch. It would be impossible for me to finish this dissertation without his continuous help and support.

I would like to thank Ajit Srivastava for helping me move from high energy to condensed matter physics during my first year at Emory. I am thankful to Stefan Boettcher for giving me good advice when I was under pressure and helping me negotiate with my parents about the importance of my PhD life. Also, I would like to thank Justin Burton and Carlos Sa de Melo for guiding me toward graduation and being on the committee. There are so many faculties and staffs who have supported me in the past five years, I cannot list all the names here but I am more than grateful.

Particular thanks goes to Daniel Shaffer for the collaboration during two research projects which are quite successful. The way that Daniel thinks about superconductivity has redefined my understanding on this subject. I am also thankful to Lakshmi Iyer and Mahajabin Rahman for making the office a lively place, where we have shared lots of interesting ideas from different culture backgrounds.

Finally, I would like to thank Qihan Liu, Wei Li and Weijie Li, who are my roommates and best friends. As a team, we have made good plans together for renting, driving, cooking and much more, without them I could not have enjoyed my life in the US.

Contents

List of Figures

5.2 RG flow of coupling constants $g_{mn}^{(\ell)j}$ with $\ell = 0, 1$ (solid and dashed lines respectively), $j = 1, 1', 2, 3, 4$ (red, light red, blue, magenta and green respectively), and $m, n = 0, \ldots, q-1$ for (a) $q = 2$ at 1/4 filling at perfect nesting $d_{ph} = 1$; and for (c) $q = 3$ at 1/6 filling with $d_{ph} = 0.8$ ($U = 1$ in arbitrary units in all plots). The instability occurs at $t_c = 0.93$ and $t_c = 1.46$ for $q = 2$ and 3 respectively. The flows for $q = 2$ and 3 are otherwise qualitatively similar, and both are similar to the flow in the absence of the magnetic field: while all coupling constants are initially positive or vanish, $g_{mn}^{(\ell)1}$ and $g_{mn}^{(\ell)1'}$ eventually change sign, leading to effective attraction in the pairing channel. The inset in (c) shows the $q = 3$ flow normalized by $g_{00}^{(0)4}$ which shows that the self-similar fixed trajectory $g_{mn}^{(\ell)j} = g_j/\sqrt{q}$ is reached at the end of the flow, as indicated by curves of the same color approaching the same value (we also find $g_1 = g_{1'}$). (b) $q = 2$ RG flow of the susceptibilities χ_I with I corresponding to SC with Cooper pairs with zero momentum ($\ell = 0$, red) or momentum $\mathbf{Q} = \frac{2\pi p}{q}\hat{\mathbf{y}}$ ($\ell = 1$, magenta), SDW (green) or CDW (blue). Initially χ_{SDW} is the fastest growing susceptibility, but eventually The $\ell = 0$ SC susceptibility takes over. The inset shows the corresponding critical exponents $\alpha_I = \left(1 - \log_{t_c - t} \chi_I\right)/2$ for the same range of RG times t. The largest exponent at the end of the flow is $\alpha_{SC,\ell=0}(t_c) \approx 0.73$. (d) Shows that analogous plots for $q = 3$, but in this case the $\ell = 0$ and 1 SC channels are degenerate so only the former is plotted; in this case red and magenta colors indicate the suscpetibilities at v = 0 and 1 VHS points respectively, which contribute to the same SC channel. The largest exponent at the end of the flow is $\alpha_{SC}(t_c) \approx 0.65$. 130

5.3 **(a)** Gap functions at the VHS obtained from the RG analysis for $q = 2$ at perfect nesting (left) and for $q = 3$ at $d_{ph} = 0.8$ in the top and bottom Hofstadter bands (right). In both cases the gap function changes sign between the two VHSs v $= 0, 1$. Here we focus on pairing with zero total momentum $\ell = 0$, with pairings for $\ell \neq 0$ determined by MTG symmetries. **(b)** Real space structure of the gap function for $q = 2$ even under $\hat{T}_1$ and $\hat{T}_2$ and odd under $\hat{C}_4$, shown within a single magnetic unit cell (the pattern repeats in all cells). **(c)** Profile of the gap function $\Delta_{R_x\hat{\mathbf{x}},s;0,s'}$ for $q = 3$ as a function of the horizontal magnetic unit cell separation R_x between Cooper pairs (with lattice constant $a = 1$). Note that the gap function oscillates between each unit cell and decays as $1/R_x^2$ at long distances. See Section 5.5 for more details. **(d)** The projection onto the Fermi surface of the gap function for $q = 2$ shown in **(b)** as a function of the angle $\theta_{\mathbf{p}}$ along the Fermi surface within the rMBZ (note that $\Delta_m^{(\ell)}$ are equal within each patch m). Note that the gap crosses zero, indicating nodes in the fermionic spectrum. **(e-f)** The projection onto the Fermi surface of the model gap function for $q = 3$ for the top (red) and bottom (blue) bands that agrees with the gap function found in the RG analysis. Note that the magnitude of the gap function never vanishes as shown in **(e)**, implying that the fermionic spectrum is fully gapped (the sharp features at $\theta_{\mathbf{p}} = 0, \pi$ are due to the corners of the Fermi surface). The phase of the projected gap functions, however, winds by $\pm 4\pi$ around the Fermi surface in the top and bottom bands respectively, as shown in **(f)**, implying each $\Delta_m^{(\ell)}$ contributes ± 2 to the Chern number. Plots **(c-e)** are given in arbitrary units as the magnitude of the gap function is not determined within the weak coupling theory. 133

List of Tables

Chapter 1

Introduction

A central theme in physics is to understand the collective behavior of phases of matter [6]. In that regard, a key aspect is that of spontaneous breaking of symmetries, which occurs when the low energy state of the system displays less degree of symmetry than the underlying interactions. A familiar, yet striking, example of this phenomenon occurs in crystals, in that, while fundamental microscopic interactions respect translation invariance, the low energy state breaks the full translation symmetry of empty space down to discrete translations respected by the emerging periodic arrangement of atoms. The existence of crystalline patterns, in turn, affects quantum mechanical properties of electrons in a solid, accounting for a wide range of metallic and insulating materials. The same mechanism applied to other symmetries dictates much of the thermodynamic properties of a zoo of macroscopic phases of matter observed in nature.

The mathematical underpinnings of spontaneous symmetry breaking were introduced by Landau and Ginzburg[7, 8] in the 1950s, who proposed the existence of an order parameter to characterize the macroscopic state of matter. An order parameter is a local field that acquires a non-zero expectation value in the symmetry broken phases and remains zero if the symmetry is preserved. In a crystal, for example,

the order parameter is encoded in the Fourier components capturing the onset of periodic density modulations, while, in a magnet, for example, the local magnetization is the order parameter. The Ginzurg-Landau approach is also very powerful in describing subtle quantum phenomena such as superconductivity, wherein the order parameter captures the onset of a collective condensate of electron pairs[8]. The Ginzburg-Landau framework is one of the theoretical pillars that allow one to classify the macroscopic behaviors of matter, draw meaningful interpretations of experimental observations, and make powerful symmetry-based predictions even when the detailed microscopic information of the system is lacking.

Enter Topological Phases of Matter

However, the ground shaking discovery of the quantum Hall effect[9–11] in the 1980s has shown that quantum matter admits unexpected phase structures that fall outside of the Ginzburg-Landau paradigm. The quantum Hall effect represents a new phase of matter wherein a two-dimensional (2D) electron gas in a perpendicular magnetic field gives rise to a nontrivial type of bulk insulator supporting chiral (that is, unidirectional) electronic states propagating along the 1D edge[12, 13]. For sufficiently low temperature, low disordered systems, the Hall conductance $\sigma = I_x/V_y$ – the ratio of the electric current to the perpendicular Hall voltage – acquires quantized values $\sigma_H = \nu e^2/h$ around stable plateaus, where $-e$ is the charge of the electron and h is Planck's constant. The integer and fractional quantum Hall effects refer to the cases where ν is integral or rational, respectively. A remarkable feature is that this sharp quantization condition takes place in a complex electronic system subject to imperfections and disorder[14, 15]. Essentially, the stability of the quantized phenomenon to perturbations of the system and the absence of a symmetry breaking mechanism establish the quantum Hall effect as a quintessential topological phenomenon[16–21].

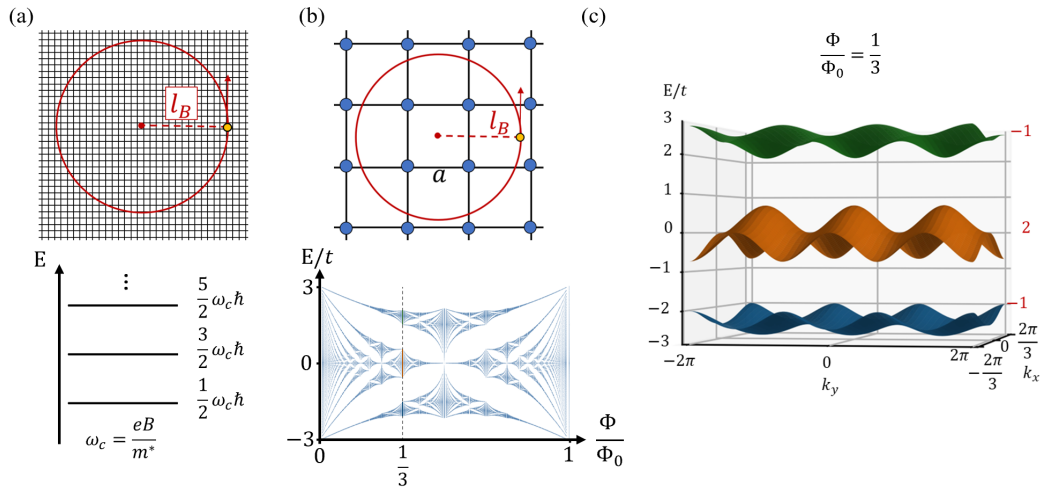

Figure 1.1: The competition between the magnetic length l_B and the lattice constant a gives rise to the Hofstadter Butterfly. **(a)** At $l_B >> a$, the energy spectrum of the 2D lattice with a uniform magnetic field is described by Landau levels $E_n = (n+1/2)\omega_c\hbar$, $n \in \mathbb{Z}$. **(b)** At $l_B \sim a$, the energy spectrum becomes fractal and self-similar by tuning the magnetic flux Φ per unit cell. The spectrum is then called the Hofstadter Butterfly. **(c)** The Hofstadter bands at $\Phi/\Phi_0 = 1/3$.

What are the mathematical underpinnings of this topological phase of matter? Key steps in elucidating the role of topology in the integer quantum Hall effect were uncovered by the seminar works of Hofstadter[4] and, subsequently, Thouless, Kohmoto, Nightingale and den Nijs (TKNN)[22]. First, Hofstadter has shown that an external magnetic field can fundamentally modify the quantum states of electrons in two dimensional lattices. Semiclassically, the field affects electronic motion through cyclotron orbits of radius $l_B = \sqrt{h/(eB)}$, denoted the magnetic length. As shown in Ref. [4] and Fig. 1.1, the competition between the length scales set by the size of the unit cell of the lattice, a and the magnetic length l_B gives rise to a rich spectrum dubbed the *Hofstadter Butterfly*. The nature of the electronic bands strongly depends on the ratio Φ/Φ_0, where $\Phi = Ba^2$ is the flux per unit cell (say, for concreteness, on the square lattice with lattice constant a) and $\Phi_0 = h/e$ is the quantum of flux. A remarkable feature discovered by Hofstadter is that the energy spectrum of this physical system is far from ordinary. In fact, the spectrum support self-similar fractal

electronic bands as shown in Fig. 1.1b.

Crucially, TKNN have taken Hofstadter's discovery one step ahead, establishing that a band insulator in which electrons fully occupy an integer number of Hofstadter bands is, in fact, a quantum Hall system whose Hall conductance is expressed as $\sigma_H = \frac{e^2}{h}C$, where $C = \sum_{E_\alpha < E_F} C_\alpha$ is an integer invariant that captures the topological aspect of the filled Hofstadter bands below the Fermi energy E_F, and the Chern number of the α-th band is defined as

$$C_\alpha = \frac{1}{2\pi}\int_{BZ} d^2k \mathcal{F}_{\alpha xy}(\mathbf{k})\,, \tag{1.1}$$

where the integral is performed in the first Brillouin zone(BZ). The Chern number is given by the integral in momentum space of the gauge invariant Berry curvature[23]

$$\mathcal{F}_{\alpha ij}(\mathbf{k}) = \partial_{k_i}\mathcal{A}_{\alpha j}(\mathbf{k}) - \partial_{k_j}\mathcal{A}_{\alpha i}(\mathbf{k}) \tag{1.2}$$

obtained from the curl of the Berry connection of the isolated band α,

$$\boldsymbol{\mathcal{A}}_\alpha(\mathbf{k}) = i\,\langle \alpha, \mathbf{k}|\,\partial_{\mathbf{k}}\,|\alpha, \mathbf{k}\rangle\ , \tag{1.3}$$

where $|\alpha, \mathbf{k}\rangle$ is the Bloch state associated with the α-th band.

The above discussion suggests the existence of a close connection between electromagnetism in real space and topological aspects of Bloch states in momentum space, with the Berry curvature playing the role a momentum space magnetic field. In particular, this connection shows that a band structure with a quantized Chern number provides a momentum space realization of a magnetic monopole[24, 25]. Since this quantized invariant is robust to perturbations that do not close the spectral gap[26–28], the identification of the quantum Hall response with topological properties of Bloch states provides a topological explanation for the stability of the quantum Hall

effect.

Despite deep conceptual advances revealed by the connections between Hofstadter system and band topology, in practical terms, the Hofstadter regime had remained inaccessible in realistic 2D systems. This was due to the fact that, in typical 2D semiconductors[14, 15, 29] as well as in atomically thin 2D materials such as graphene[30–35] and transition metal dichalcogenides[36–38], the lattice constant resides on the scale of a few Angstrons, implying that, for laboratory accessible magnetic fields, $\Phi/\Phi_0 \sim 10^{-4} - 10^{-3}$. As such, the flux quantum that penetrates the unit cell of the lattice is much smaller than h/e, or, equivalently, the magnetic length turns out to be much larger than the lattice constant. In this regime, lattice effects become relatively weak, causing Hofstadter bands to behave effectively as degenerate Landau levels[12, 14, 39], which are equally separated by an energy gap $\hbar\omega_c = \frac{\hbar eB}{m^*}$, where m^* is the effective electronic mass and $\omega_c = \frac{eB}{m^*}$ is the cyclotron frequency (see Fig. 1.1a). Since Φ scales linearly with the magnetic field, it would require an impractical field increase of 3 to 4 orders of magnitude for fluxes comparable to h/e to be realized.

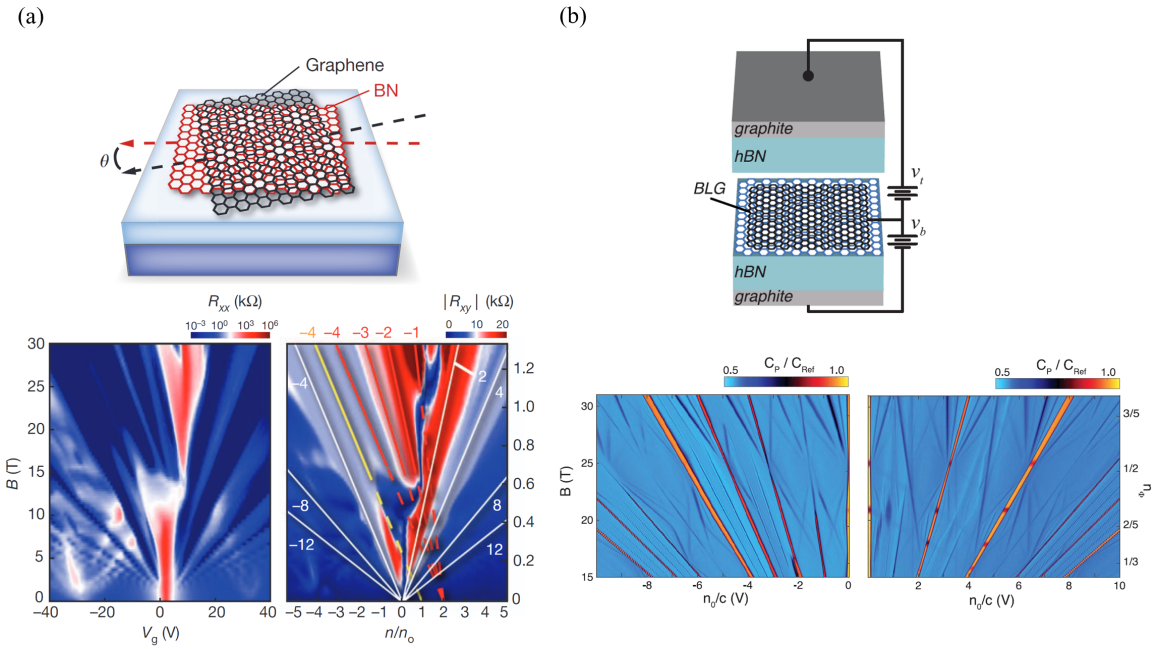

C. R. Dean et al, Nature 2013 *E. M. Spanton et al, Science 2018*

Figure 1.2: Two examples of experimental realization of Hofstadter quantum materials in moiré systems[1, 2]. The nanometer scale unit cells of moiré systems enable the realization of Hofstadter bands in experimentally accessible magnetic fields at which the magnetic flux per super unit cell Φ is comparable to the flux quantum Φ_0. The existence of Hofstadter band structures are verified by measuring **(a)** Hall conductance and **(b)** magnetocapacitance.

In recent years, however, this problem has been circumvented with the emergence of new 2D quantum platforms with nanometer scale unit cells. In particular, moiré superlattices obtained by stacking 2D graphene and other atomically thin materials with small misalignment as shown in Fig 1.2 have emerged as versatile platforms to probe new quantum phases of matter.[40–44] Due to their effective large scale unit cell, these platforms allow experimental investigation of regimes of magnetic flux comparable to quantum of flux with laboratory scale fields. Consequently, Hofstadter quantum materials have experienced a renaissance, emerging as an active frontier of investigation of fundamental questions, with synergies between experiment [1, 2, 45–55] (see Fig. 1.2) and theory[56–72].

What is this thesis about?

The interplay of electronic interactions, orbital field effects and lattice degrees of freedom make Hofstadter systems promising to the pursuit unconventional quantum phases of matter. Addressing these new opportunities, this thesis invites a new perspective on the potentialities of Hofstadter quantum materials, by presenting theoretical investigations that uncover a new body of phenomena transcending traditional quantum Hall physics, which arises due to the rich properties of these fractal electronic systems.

The first of these properties is self-similarity. In Hofstadter bands, this is manifested in the form of a nontrivial organization of Bloch electrons into q-fold degenerate states when the flux per unit cell is a rational p/q of the flux quantum. Thus the ability to tune the band structure of Hofstadter systems using the external field as a control knob is a striking feature explored in this thesis. Directly related to this, it follows that Hofstadter bands support a tunable manifold of Van Hove singularities[73]. These singularities arise from a change in topology of the Fermi surface contours and give rise to a logarithmic divergence in the electronic density of states in 2D bands[73], which enhances the effect of interactions and favors the formation of new ground states via competition of electronic instabilities[74–89]. Furthermore, Hofstadter bands display pronounced lattice effects and finite bandwidth[4, 90] that set them apart from Landau levels, as shown in Fig. 1.1b,c.

What makes Hofstadter bands so distinct from other crystalline systems? In short, the interplay of the lattice translations and the external gauge field accounts for a great deal of the rich physics encoded in such systems. That can be appreciated by recognizing that, in the presence of a vector potential $\boldsymbol{A}(\boldsymbol{r})$ associated with a magnetic field $\boldsymbol{B} = \boldsymbol{\nabla} \times \boldsymbol{A}(\boldsymbol{r})$, the momentum $\boldsymbol{p} = i\hbar\boldsymbol{\nabla}$ of a particle of charge $-e$ is changed (minimal coupling) to $\boldsymbol{p} + e\,\boldsymbol{A}(\boldsymbol{r})$. Importantly, even in the presence of a uniform magnetic field $\boldsymbol{B} = B\hat{z}$ (say, along z direction), the vector potential is a lin-

ear function of the position. Consequently, the presence of an external uniform field breaks the original translation symmetries $\hat{T}_{\hat{\mathbf{x}}}$ and $\hat{T}_{\hat{\mathbf{y}}}$ in the absence of a field. The effect of the shift in the vector potential can be compensated by a gauge transformation, leading to *magnetic translation symmetry* operators $\hat{T}_x$ and $\hat{T}_y$ that commute with the Hamiltonian. However, these new symmetry generators satisfy a modified commutation relation

$$\hat{T}_x \hat{T}_y = e^{i2\pi\Phi/\Phi_0} \hat{T}_y \hat{T}_x \tag{1.4}$$

that captures the Aharonov-Bohm effect associated with the motion of an electron around the unit cell of the lattice, which is pierced by the flux Φ as shown in Fig. 1.3. The resulting *Magnetic Translation Group* (MTG)[91–93] and its non-Abelian character endow Hofstadter bands with rich electronic states. In particular, for $\frac{\Phi}{\Phi_0} = \frac{p}{q}$, Eq. (1.4) implies that the irreducible representation of the MTG on single particle states are q-dimensional, giving rise to q-fold degenerate energy spectrum.

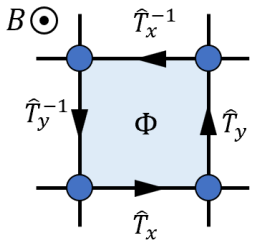

Figure 1.3: Due to the magnetic flux Φ penetrating the unit cell, the election hoppings in the x and y directions are associated with Aharanov-Bohm phases and no longer commute. The motion of an electron around the unit cell is associated with a total Aharanov-Bohm phase $e^{i2\pi\Phi/\Phi_0}$, giving rise to a modified commutation relation Eq. (1.4).

In this thesis we investigate novel collective behavior of electrons in Hofstadter systems that is intimately related to these properties of the MTG. In particular, we show a pathway to superconducting phases driven entirely by repulsive interactions and classify novel topological phase transitions induced coupling to lattice effects.

1.1 Three Themes

This thesis investigates three themes in Hofstadter quantum materials, concerned with (1) the nature of topological quantum phase transitions, (2) a classification of superconducting states and (3) microscopic mechanisms for charge and spin density waves, as well as unconventional superconductivity driven entirely by repulsive interactions.

Theme 1: Quantum Phase Transitions in Hofstadter Systems

Jian Wang and Luiz H. Santos, *Classification of Topological Phase Transitions and van Hove Singularity Steering Mechanism in Graphene Superlattices*, Phys. Rev. Lett. **125** 236805 (2020).

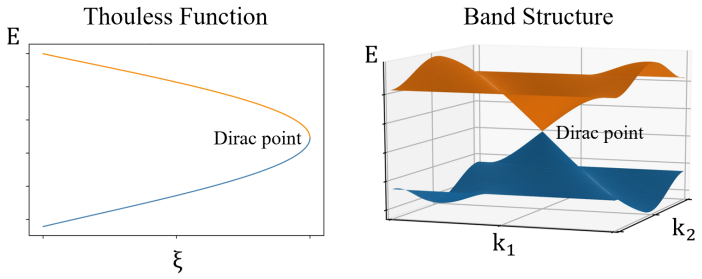

Figure 1.4: Quantum criticality in the honeycomb Hofstadter lattice is classified with a universal spectrum function named Thouless function.

Chapter 3 of the thesis discusses certain universal properties of quantum phase transitions in Hofstadter-Chern insulators[60, 94–107]. As the magnetic length becomes comparable to the lattice constant, topological phases in Hofstadter bands become strongly coupled to the underlying lattice[45, 72, 95, 108–120]. As such, the questions raised in this portion of the thesis are *(1) Can lattice degrees of freedom induce topological quantum phase transitions that are intrinsically distinct from traditional quantum Hall plateau transitions in Landau levels?* If so, *(2) what is*

the underlying mechanism that changes the topological properties of Hofstadter-Chern insulators? (3) What constitutes the universality class of such topological phase transitions?

In answering these questions, this thesis establishes a theoretical framework describing quantum phase transitions in Hofstadter-Chern insulators on the paradigmatic honeycomb lattice. The response of the system to lattice effects encoded in modulations of the hopping parameters is studied analytically and numerically. Analytical results are extracted from the self-similarity of the bands. The critical point is described by a universality class of multi-component Dirac fermions transforming under the action of MTG, which accounts for the existence of large jumps in the Hall resistivity that are distinct from conventional plateau transitions. Furthermore, the work establishes a new connection between the energy scale of these unconventional critical points and a regime of Van Hove singularities in Hofstadter-Chern bands, which provides a new mechanism to understand the emergence of topological quantum criticality in a fractal spectrum.

Theme 2: Theory of Hofstadter Superconductors

Daniel Shaffer, Jian Wang, and Luiz H. Santos, *Theory of Hofstadter Superconductors*, Phys. Rev. B **104** 184501 (2021).

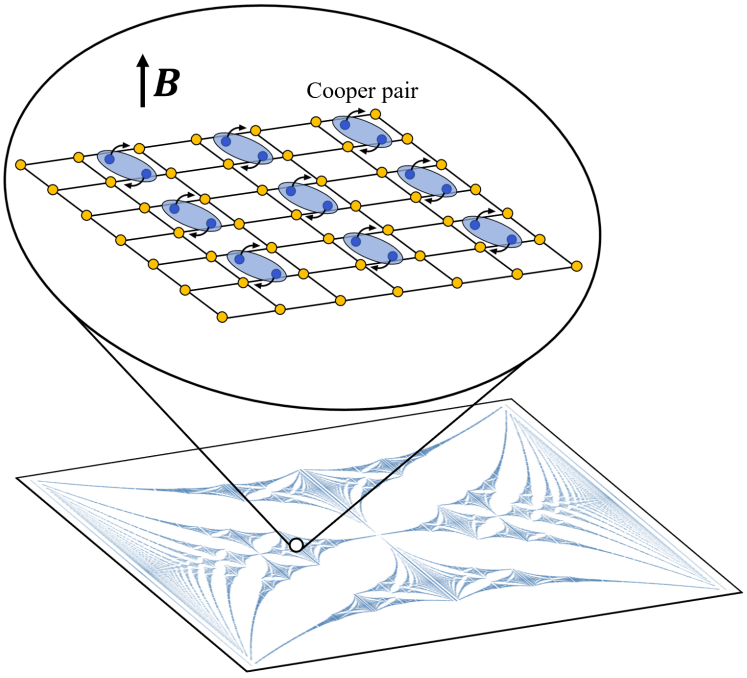

Figure 1.5: Electronic pairing states in Hofstadter bands gives rise to unconventional superconductivity at high magnetic fields.

Chapter 4 of the thesis addresses the nature of superconductivity in Hofstadter systems by raising a question of principle: *if a superconducting state arises in a Hofstadter lattice, what forms of electronic pairing are compatible with self-similar electronic bands? What are the symmetry broken and topological properties of such Hofstadter superconductors?*

To answer these questions, this chapter starts by providing a comprehensive study of the irreducible representations of the MTG acting on charge $2e$ pairing fields. The analysis shows that the order parameter of Hofstadter superconductors is multi-dimensional due to the onset of pairing correlations across momentum resolved patches of the Brillouin zone. This new group-theoretical analysis, furthermore, forms the basis for a Ginzburg-Landau theory of Hofstadter superconductors, which is shown to possess a very rich phase diagram. A central result is established, namely, that MTG is necessarily broken when superconducting correlations develop in Hofstadter

bands, a distinguishing property of Hofstadter superconductors that is in contrast with weakly interacting Hofstadter-Chern insulators. In particular, the study identifies a new class of charge $2e$ condensate dubbed $\mathbb{Z}_q$ *Hofstadter superconductor*, which arises when MTG is broken down to a cyclic $\mathbb{Z}_q$ subgroup. Our analytical results show that this class of states support unconventional excitations, such as Bogoliubov Fermi surfaces[121–132] and chiral Majorana edge states[133], which are distinct from fermionic excitations in conventional superconductors.

Theme 3: Competing Orders in Hofstadter Quantum Materials

Daniel Shaffer, Jian Wang, and Luiz H. Santos, *Unconventional Self-Similar Hofstadter Superconductivity from Repulsive Interactions*, arXiv:2204.13116 (2022).

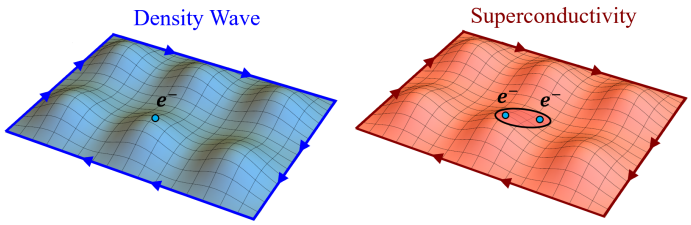

Figure 1.6: In a Hofstadter lattice with repulsive Hubbard interaction, unconventional superconductivity and density waves emerge as competing ordered states of electrons.

Complex quantum materials can be characterized by rich phase diagrams, which manifest an intricate competition between different electronic ground states. While the study of competing orders has been devoted to several correlated materials, such as high temperature superconductors[113, 134–141], the similar analysis in Hofstadter systems has escaped previous consideration.

In Chapter 5, a new theory of competing electronic orders is developed in Hofstadter systems. In particular, the role of repulsive interactions is analysed when

the Fermi energy lies in the vicinity of Van Hove singularities. Unlike Landau levels, Hofstadter bands have finite bandwidth and display a rich manifold of Van Hove singularities, whose number (proportional to q) can be tuned as a function of the magnetic flux $\Phi = 2\pi(p/q)h/e$ per unit cell. Exploring this control knob, a weak coupling renormalization group (RG) analysis[142–144] is performed for the fermionic Hofstadter-Hubbard model on the square lattice, establishing a rich competition of electronic orders, from which *electronic pairing emerges as a low energy instability.* This scenario of competing orders near VHSs underlies several proposed mechanisms of unconventional superconductivity through repulsive interactions, for example in cuprates[74–76], doped graphene[77–80] and moiré graphene superlattices[81–89]. The work in this thesis extends this analysis to the new realm of Hofstadter electronic bands, uncovering a new microscopic mechanism for the realization of reentrant superconductivity[145–156] in Hofstadter materials, which could be within near-term experimental reach in moiré superlattices.

This theory gives an original contribution in that it incorporates the constraints of the MTG to fermionic RG. Specifically, it establishes that, as high energy electronic states are integrated out, the emerging low energy theory displays an emergent self-similarity in that the RG equations admit fixed trajectories equivalent to those in the zero field system[74, 75, 157]. Using these new methods, it is found that Hofstadter Fermi liquids can undergo instability towards nodal d-wave superconductivity near 1/4 and 3/4 fillings in the π-flux lattice (when the flux per unit cell is $\Phi = h/2e$), as well as chiral topological superconductivity with Chern number $\mathcal{C} = \pm 6$ near 1/6 and 5/6 fillings in the $\pm 2\pi/3$-flux lattice (when the flux per unit cell is $\Phi = \pm h/3e$). Besides superconductivity, the RG analysis uncovers charge and density wave states, establishing Hofstadter quantum materials as a promising platform to explore novel quantum interacting phases of matter.

Chapter 2

Hofstadter Model: Background

In this section, we will discuss the Hofstadter model which will be used throughout this thesis. The Hofstadter model is established by Douglas Hofstadter[4] to describe the motion of electrons in two-dimensional materials under a strong perpendicular magnetic field $\mathbf{B}$ (strong in the sense that the magnetic length scale $l_B = \sqrt{h/(eB)}$ is comparable to the lattice constant). Astonishingly, Hofstadter found that the electronic energy dispersion forms a fractal spectrum, exhibiting a self-similar pattern resembling a butterfly(see Fig. 2.2). Hofstadter's Butterfly arises from the interplay between Landau levels and lattice structures. Compared with a Landau level, a Hofstadter band has a finite band width and a nontrivial Chern number[22, 57], giving rise to rich quantum phase transitions induced by tuning lattice parameters. By turning on interactions, Hofstadter bands can support novel topological phases beyond quantum Hall insulators. These above arguments will be further exploited in Chapter 3-5.

2.1 Square Lattice

We start with a square lattice in a perpendicular magnetic field $\mathbf{B} = B\hat{\mathbf{z}}$ as shown in Fig. 2.1. Neglecting spin-orbital effects, the system is described by the tight-binding

Hamiltonian of spinless electrons with nearest-neighbor hoppings:

$$H = -\sum_{\langle \mathbf{r}\mathbf{r}' \rangle} t\, e^{2\pi i A_{\mathbf{r}\mathbf{r}'}} c^{\dagger}_{\mathbf{r}} c_{\mathbf{r}'} + h.c.\,, \tag{2.1}$$

where the lattice vector $\mathbf{r} = (x, y)$ and $A_{\mathbf{r}\mathbf{r}'} = \int_{\mathbf{r}}^{\mathbf{r}'} \mathbf{A} \cdot d\mathbf{r}/\Phi_0$ with the flux quantum $\Phi_0 = 2\pi\hbar/e = 2\pi$. We work in the Landau gauge with vector potential $\mathbf{A} = xB\hat{y}$ and set the lattice constant $a = 1$ so that $x, y \in \mathbb{Z}$. For the nearest neighbor atoms we have $A_{\mathbf{r}\mathbf{r}'} = x(1 - \delta_{yy'})\Phi/\Phi_0$, thus the magnetic gauge breaks the lattice translation symmetry T_x but still preserves T_y. If the flux per unit cell is a rational multiple of the flux quantum, say $\Phi/\Phi_0 = p/q$, we recognize a reminiscent symmetry $\hat{T}_x = T_x e^{2\pi i B y/\Phi_0}$ called the magnetic translation symmetry. $\hat{T}_x$ and the unbroken translation $T_y = \hat{T}_y$ along the y direction generate the non-Abelian magnetic translation group (MTG) satisfying $\hat{T}_x \hat{T}_y = \omega_q^p \hat{T}_y \hat{T}_x$ with $\omega_q = e^{2\pi i/q}$ being the q^{th} root of unity. With the commuting operators $(\hat{T}_x)^q = (T_x)^q$ and $\hat{T}_y$ from the MTG, we define the magnetic unit cell as shown in Fig. 2.1, where each site is a effective magnetic sub-lattice. We correspondingly define operators $c_{\mathbf{R},s} = c_{s\hat{\mathbf{x}}+\mathbf{R}}$ with $s = 0, \ldots, q-1$ being the sub-lattice index defined modulo q and $\mathbf{R} = (qj, y)$ with $j, y \in \mathbb{Z}$ labeling the extended unit lattice cites. With the sub-lattice notations, the Hamiltonian Eq. (5.1) is rewritten as the following:

$$H \quad = -t \sum_{\mathbf{R}} [\sum_{s=0}^{q-2} (c^{\dagger}_{\mathbf{R},s+1} c_{\mathbf{R},s} + c^{\dagger}_{\mathbf{R}+\hat{y},s} c_{\mathbf{R},s} e^{2\pi \mathrm{i} s \frac{p}{q}}) + c^{\dagger}_{\mathbf{R}+q\hat{\mathbf{x}},0} c_{\mathbf{R},q-1}] + \mathrm{h.c.} \tag{2.2}$$

Bloch's theorem then applies to the above Hamiltonian and we can write it down in momentum space using $c_{\mathbf{k}s} = \frac{1}{\sqrt{N}} \sum_{\mathbf{R}} e^{-i\mathbf{k}\cdot(s\hat{\mathbf{x}}+\mathbf{R})} c_{s\hat{\mathbf{x}}+\mathbf{R}}$, with N being the total number of unit cells and where the quasi-momentum $\mathbf{k}$ is defined on the magnetic

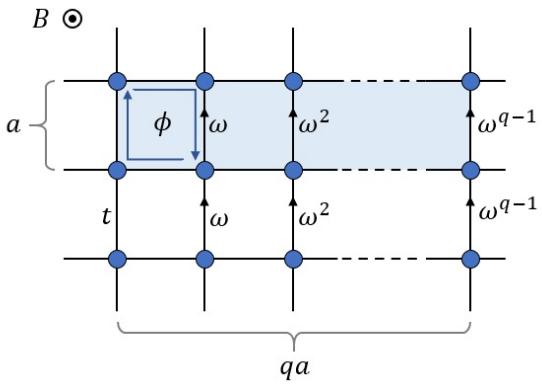

Figure 2.1: Hofstadter model on the square lattice. The uniform magnetic field $\mathbf{B}$ is perpendicularly applied to the square lattice, giving a magnetic flux $\Phi = (p/q)\Phi_0$ penetrating each unit cell. The magnetic unit cell is shown in light blue. The Aharonov–Bohm phases related to the magnetic translations are shown to the right of the arrows which indicate the direction of the electron hoppings, here $\omega = \exp(i2\pi p/q)$.

Brillouin zone (MBZ) $\mathbf{k} = (k_x, k_y) \in [-\pi/q, \pi/q) \times [-\pi, \pi)$. In this basis

$$H = -\sum_{\mathbf{k}s}(2t\cos(k_y + sQ) + \mu)c^\dagger_{\mathbf{k}s}c_{\mathbf{k}s} - \sum_{\mathbf{k}\langle ss'\rangle} te^{-ik_x(s-s')}c^\dagger_{\mathbf{k}s}c_{\mathbf{k}s'}\,, \tag{2.3}$$

and the magnetic translation symmetries act as $\hat{T}_x c_{\mathbf{k}s}\hat{T}_x^\dagger = e^{-ik_x}c_{\mathbf{k}+\mathbf{Q},s+1}$ and $\hat{T}_y c_{\mathbf{k}s}\hat{T}_y^\dagger = e^{-ik_y}c_{\mathbf{k}s}$, with $\mathbf{Q} = \frac{2\pi p}{q}\hat{\mathbf{y}}$. Note that the k-space Hamiltonian is $q \times q$.

The Hofstadter Hamiltonian H can then be diagonalized as $H_0 = \sum_{\mathbf{k}\alpha\sigma}\varepsilon_\alpha(\mathbf{k})d^\dagger_{\mathbf{k}\alpha}d_{\mathbf{k}\alpha}$ using a unitary transformation

$$d_{\mathbf{k}\alpha\sigma} = \sum_s \mathcal{U}^s_\alpha(\mathbf{k})c_{\mathbf{k}s}\,. \tag{2.4}$$

We present the numerical result for the band structure at $\Phi/\Phi_0 = 1/3$ in Fig. 2.2a. Note that there is a gauge freedom in choosing the U(1) phases in $\mathcal{U}^s_\alpha(\mathbf{k})$. Although the Hofstadter Hamiltonian is gauge invariant, the phases must be fixed if the U(1) gauge symmetry is broken, for example, in the case when a superconducting order parameter $\langle d_{-\mathbf{k}\alpha}d_{\mathbf{k}\beta}\rangle$ is induced by the interactions, as discussed in Chapter 4

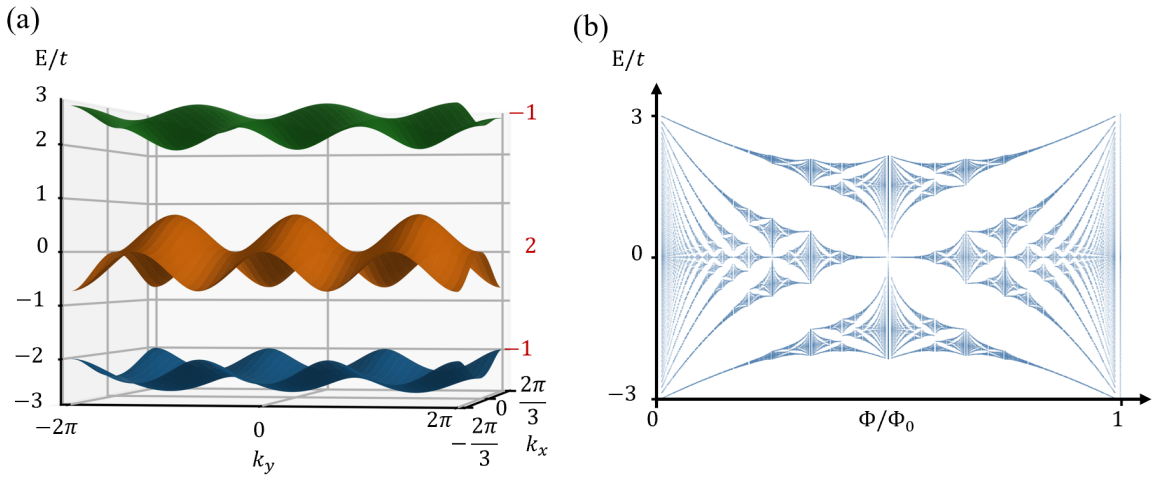

Figure 2.2: **(a)** The band structure of the Hofstadter model on a square lattice at $\Phi/\Phi_0 = 1/3$. The Chern numbers of the bands are shown in red. **(b)** The Hofstadter butterfly for the square lattice. The energy levels develops into a fractal spectrum by tuning the magnetic flux per unit cell.

and 5. For concreteness, we take $\mathcal{U}_\alpha^{s+1}(\mathbf{k}+\mathbf{Q}) = \mathcal{U}_\alpha^s(\mathbf{k})$, which endures a canonical transformation under MTG for the band operators: $\hat{T}_x d_{\mathbf{k}\alpha\sigma}\hat{T}_x^\dagger = e^{-ik_x} d_{\mathbf{k}+\mathbf{Q},\alpha,\sigma}$ and $\hat{T}_y d_{\mathbf{k}\alpha\sigma}\hat{T}_y^\dagger = e^{-ik_y} d_{\mathbf{k}\alpha\sigma}$. Furthermore, we fix the remaining gauge freedom by taking $\mathcal{U}_\alpha^1(\mathbf{k}) \in \mathbb{R}$. This choice makes it clear that the $\hat{T}_x$ symmetry implies a q-fold degeneracy of each band, $\varepsilon_\alpha(\mathbf{k}) = \varepsilon_\alpha(\mathbf{k}+\mathbf{Q})$. This q-fold degeneracy is a generic feature of Hofstadter bands.

2.2 Honeycomb Lattice

We then consider the Hofstadter model on a honeycomb lattice. Similar to the square lattice, we neglect spin and write down the tight-binding Hamiltonian with nearest-neighbor hoppings as follows:

$$H = -\sum_{\langle \mathbf{r}\mathbf{r}' \rangle} t\, e^{2\pi i A_{\mathbf{r}\mathbf{r}'}} a_{\mathbf{r}}^\dagger b_{\mathbf{r}'} + h.c.\,, \tag{2.5}$$

where $a_{\mathbf{r}}$ and $b_{\mathbf{r}}$ labels the two triangle sub-lattices, the lattice vector $\mathbf{r} = m\mathbf{a}_1 + n\mathbf{a}_2$, $m, n \in \mathbb{Z}$ and $A_{\mathbf{r}\mathbf{r}'} = \int_{\mathbf{r}}^{\mathbf{r}'} \mathbf{A}\cdot d\mathbf{r}/\Phi_0$. We set the lattice constant to be 1 and the

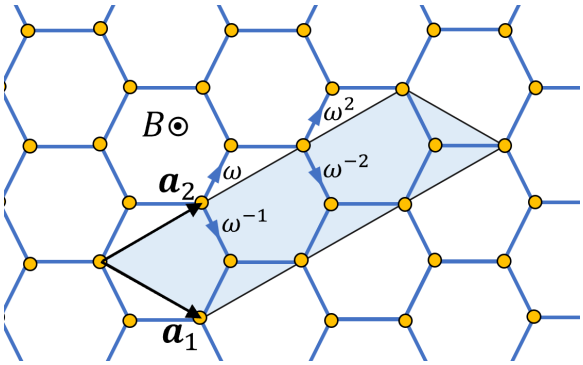

Figure 2.3: Hofstadter model on the honeycomb lattice at flux $\Phi = (1/3)\Phi_0$ per unit cell. The magnetic unit cell is shown in light blue. The Aharonov–Bohm phases related to the magnetic translations are shown to the right of the arrows which indicate the direction of the electron hoppings, here $\omega = \exp(i2\pi/3)$.

lattice basis to be $\mathbf{a}_1 = (3/2, -\sqrt{3}/2)$, $\mathbf{a}_2 = (3/2, \sqrt{3}/2)$ as shown in Fig.2.3. We choose a gauge $\mathbf{A} = (0, x + \sqrt{3}y, 0)B = (0, 3nB, 0)$ and set the flux per unit cell to be $\Phi = (p/q)\Phi_0$ to write down the following Hamiltonian:

$$H = -t \sum_{\mathbf{r}(m,n)} (a^\dagger_{\mathbf{r}} b_{\mathbf{r}} + \omega^{-n} a^\dagger_{\mathbf{r}} b_{\mathbf{r}+\mathbf{a}_1} + \omega^n a^\dagger_{\mathbf{r}} b_{\mathbf{r}+\mathbf{a}_2}) + \text{h.c.} \tag{2.6}$$

where $\omega = \mathrm{e}^{2\pi i p/q}$. Note that the position of atom $b_{\mathbf{r}}$ is actually $\mathbf{r} + (-1, 0)$, we have neglect the integral along $(-1, 0)$ and other constant contributions to the integral $A_{\mathbf{r}\mathbf{r}'}$ since they can be eliminated by a gauge transformation on the lattice basis.

The gauge $\mathbf{A}$ breaks the lattice translation symmetry $T_{\mathbf{a}_2}$ and preserves $T_{\mathbf{a}_1}$. We then write down the magnetic translations $\hat{T}_1 = T_{\mathbf{a}_1}, \hat{T}_2 = T_{\mathbf{a}_2} e^{2\pi i B n/\Phi_0}$ and define the magnetic unit cell by the commuting MTG operators $\hat{T}_1$ and $(\hat{T}_2)^q = (T_{\mathbf{a}_2})^q$. The Hamiltonian is then written as the following:

$$H = -t \sum_{\mathbf{r}} [\sum_{s=0}^{q-1} (a^\dagger_{\mathbf{r}s} b_{\mathbf{r}s} + \omega^{-s} a^\dagger_{\mathbf{r}s} b_{\mathbf{r}+\mathbf{a}_1,s}) + \sum_{s=0}^{q-2} \omega^s a^\dagger_{\mathbf{r}s} b_{\mathbf{r},s+1} + \omega^{q-1} a^\dagger_{\mathbf{r},q-1} b_{\mathbf{r}+q\mathbf{a}_2,0}] + \text{h.c.} \tag{2.7}$$

Bloch's theorem then applies to the above Hamiltonian and we can write it down in

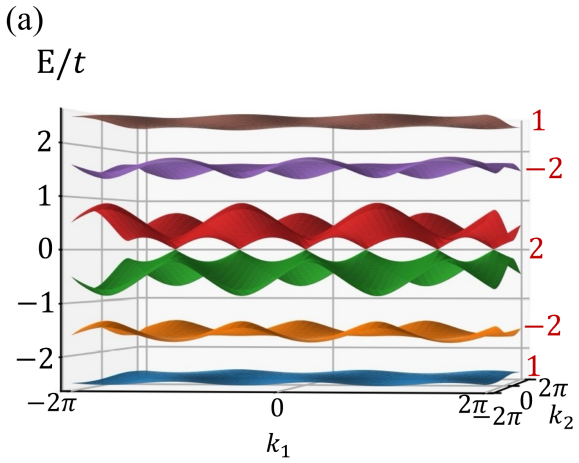

Figure 2.4: The band structure of the Hofstadter model on a honeycomb lattice at $\Phi/\Phi_0 = 1/3$. The Chern numbers of the bands are shown in red.

momentum space using $a_{\mathbf{k}s} = \frac{1}{\sqrt{N}} \sum_{\mathbf{R}} e^{-i\mathbf{k}\cdot(s\hat{\mathbf{x}}+\mathbf{R})} a_{s\mathbf{a}_2+\mathbf{R}}$, (the same for $a_{\mathbf{k}s}$) with N being the total number of unit cells and where the quasi-momentum $\mathbf{k}$ is defined on the magnetic Brillouin zone (MBZ) $\mathbf{k} = k_1\mathbf{g}_1 + k_2\mathbf{g}_2$, where $\mathbf{g}_2$, $\mathbf{g}_2$ are the reciprocal lattice basis and $k_1, k_2 \in [-\pi, \pi)$. In this basis

$$H = -t \sum_{\mathbf{k},r,s} h_{rs}(\mathbf{k}) a_{\mathbf{k}}^{(r)\dagger} b_{\mathbf{k}}^{(s)} + \text{h.c.} \tag{2.8}$$

where the non-zero $h_{rs}(\mathbf{k})$ are given as the following:

$$\begin{aligned} h_{ss} &= 1 + \mathrm{e}^{\mathrm{i}k_1}\omega^{-s} \quad s = 0, ..., q-1 \\ h_{s,s+1} &= \mathrm{e}^{\mathrm{i}k_2/q}\omega^{s} \quad s = 0, ..., q-2 \\ h_{q-1,0} &= \mathrm{e}^{\mathrm{i}k_2/q}\omega^{q-1} \end{aligned} \tag{2.9}$$

Note that $H(\mathbf{k})$ as given below

$$H(\mathbf{k}) = -t \begin{pmatrix} O & h(\mathbf{k}) \\ h^\dagger(\mathbf{k}) & O \end{pmatrix} \tag{2.10}$$

has a chiral symmetry that reads

$$\{H, \mathcal{C}\} = 0$$
$$\mathcal{C} = \begin{pmatrix} \mathbb{1} & O \\ O & -\mathbb{1} \end{pmatrix} = \mathbb{1} \otimes \hat{\tau}_z, \tag{2.11}$$

implying the following equation for the eigen energies, $\varepsilon_\alpha(\mathbf{k}) = -\varepsilon_{q-\alpha}(\mathbf{k})$. In Fig. 2.4 below, we show the honeycomb-lattice Hofstadter bands and their Chern numbers at flux $\Phi = (1/3)\Phi_0$. Note that the bands are connected through 6 Dirac cones at zero energy. The structures associated with these Dirac cones will be further studied in Chapter 3.

Chapter 3

Quantum Phase Transitions in Hofstadter Systems

3.1 Overview

The Hofstadter model realizes an epitome of topological band structures in two-dimensional lattices[4, 22, 26–28]. As discussed in Chapter 2, Hofstadter band structures arise from the competition between two length scales: the lattice constant a and the magnetic length scale $l_B = \sqrt{h/(eB)}$, which is the radius of the semi-classical cyclotron motion of the electron in a magnetic field $\mathbf{B}$. When the magnetic field is strong enough, l_B is comparable to the lattice constant a, thus the lattice potential affects the electronic states strongly and establishes an energy spectrum far from ordinary. When the magnetic flux per unit cell Φ is a rational fraction p/q, $p, q \in \mathbb{Z}$, of the flux quantum $\phi_0 = h/e$, the Aharanov-Bohm phase associated with the motion of the electron forces the number of the electronic bands to be a multiple of q. By tuning the strength of the magnetic field, the energy landscape of the Hofstadter system develops into a self-similar fractal spectrum named the Hofstadter butterfly[4] as shown in Fig. 1.1. Unlike the Landau levels[12, 14, 39] which are flat and have

identical Chern numbers, the Hofstadter bands have finite bandwidths[4, 158, 159] and highly nontrivial structures of Chern numbers[22, 26–28, 57, 160, 161], allowing for topological states of electrons beyond the traditional quantum Hall phenomena established for 2D electron gas[14, 15, 29].

As such, Hofstadter systems has long been regarded by the theorist as an arena to realize novel topological orders by populating the Hofstadter bands with electrons. Upon integer fillings of the Hofstadter bands, the spectrum is gapped and give rises to integer Hofstadter-Chern insulators (IHCI) with Hall conductance proportional to the gap Chern number[22, 28, 72, 117, 162]. At fractional fillings, the single-particle states are compressible and correspond to gapless conducting phases. However, much like the fractional quantum Hall effect[10, 11, 14], the Chern-Simons interaction between electrons will gap the system and give rise to fractional Hofstadter-Chern insulators (FHCI)[72, 111–120, 163, 164] with Hall conductance proportional to $C/(2C+1)$, where C is the gap Chern number of the quasi-particle spectrum[163–165]. The experimental realization of Hofstadter systems had been considered impossible because the unit cells of regular 2D materials are too small[14, 15, 29–38], where the lattice constants are about a few angstroms implying that, for laboratory accessible magnetic fields, $\Phi/\Phi_0 \sim 10^{-4} - 10^{-3}$. However, recent progress in the fabrication of superlattices with nanometer scale unit cells[40–44] has led to the experimental realization of integer[45, 108–110] and fractional[95] HCIs, thereby opening remarkable prospects to explore the non-trivial interplay between lattice effects and electronic topology that is inaccessible in regular 2D lattices.

Topological ground states supported in Chern bands have been broadly studied using different approaches including numerical methods[111–115, 166–168], composite fermions[72, 117–119, 163, 164] and Lieb-Schultz-Mattis type constraints.[169] On the other hand, the fundamental influence of lattice parameters on topological phase transitions (TPTs) in IHCIs and FHCIs has received significantly less attention.[56–

58] The complexity of the Hofstadter spectrum and the finite bandwidth of Chern bands that reflects their dependence on the lattice parameters and on the intra-cell magnetic flux appears to stand in the way of an overarching understanding of lattice-tuned phase transitions, which are distinct from plateau transitions tuned by the magnetic field.[170, 171].

As such, we raise the following questions in this portion of the thesis: *(1) Can lattice degrees of freedom induce topological quantum phase transitions that are intrinsically distinct from traditional quantum Hall plateau transitions in Landau levels?* If so, *(2) what is the underlying physical mechanism that changes the topology of Hofstadter-Chern insulators? (3) What constitutes the universality class of such TPTs?*

In answering these questions, we establish in this Chapter a theoretical framework describing quantum phase transitions in Hofstadter-Chern insulators on the paradigmatic honeycomb lattice. The response of the system to lattice effects encoded in modulations of the hopping parameters is studied analytically and numerically. In this chapter we provide a classification of TPTs in IHCIs and FHCIs and present a mechanism for quantum criticality tuned by lattice parameters with a fixed background magnetic field. Numerical studies[56, 58] strongly support the existence of continuous TPTs tuned by the amplitude of a square lattice weak potential projected on the lowest LL. This work, on the other hand, employs an effective tight-binding description (i.e. "strong" potential) of a honeycomb superlattice with the magnetic field incorporated via Peierls substitution and discusses topological transitions tuned by hopping amplitudes of the lattice. Graphene superlattices realized via nanolithography [172–177] not only provide a motivation for this study but also offer promising testbeds of these ideas in future experiments.

The main results established in this chapter are:

- We have shown that lattice-tuned TPTs on the honeycomb lattice with a fixed

rational intra-cell magnetic flux $\phi = (p/q)\phi_0$ are characterized by q-component Dirac fermions located in high-symmetry momenta of the magnetic Brillouin zone. We have derived a universal spectrum function called the Thouless function, which implicitly sets the momentum dependence of *all* the Hofstadter-Chern bands of the system. By analyzing the saddle points and extremals of the Thouless function, the number of flavors and their momentum space distribution are derived analytically.

- We have established a new connection between the energy scales of the van Hove singularities, which are topologically protected saddle points in Bloch bands[73], and the onset of the TPTs near charge neutrality. This result provides a new understanding to the emergence of topological quantum criticality in a fractal spectrum.

- We have extended our theoretical framework to FHCI transitions and have identified multiple candidate TPTs between Abelian FHCI states.

- We have made measurable predictions about the existence of TPTs with large jumps in the Hall resistivity that are distinct from conventional quantum Hall plateau transitions.

3.2 Model

Our setting is a honeycomb superlattice in an external perpendicular magnetic field, $B = \partial_x A_y - \partial_y A_x$, described by the single-particle nearest neighbor effective Hamiltonian

$$H = -\sum_{<\mathbf{r},\mathbf{r}'>} t_{\mathbf{r},\mathbf{r}'}\ e^{\mathrm{i}\frac{2\pi}{\phi_0}\int_{\mathbf{r}}^{\mathbf{r}'} d\mathbf{x}\cdot\mathbf{A}(\mathbf{x})}\, a^{\dagger}_{\mathbf{r}} b_{\mathbf{r}'} + \mathrm{H.c.} \tag{3.1}$$

$a^\dagger_{\mathbf{r}} = a^\dagger_{m,n}$ and $b^\dagger_{\mathbf{r}} = b^\dagger_{m,n}$ are spin polarized fermionic creation operators on the two sublattices, $\mathbf{r} = m\mathbf{a}_1 + n\mathbf{a}_2$, $m, n \in \mathbb{Z}$ is the lattice vector with basis vectors $\mathbf{a}_1 = a\,(3/2, -\sqrt{3}/2)$ and $\mathbf{a}_2 = a\,(3/2, \sqrt{3}/2)$, and $t_{\mathbf{r},\mathbf{r}'} = \{t_1, t_2, t_3\}$ are nearest neighbor real hopping elements, as shown in Fig. 3.1a. Working in the gauge $\mathbf{A} = \hat{y}(x + \sqrt{3}y)B$ with rational flux $\phi = B\,\frac{\sqrt{3}}{2}a^2 = (p/q)\phi_0$ ($p, q \in \mathbb{Z}_+$ and coprime), the real space Hamiltonian takes the following form

$$H = -\sum_{m,n} a^\dagger_{m,n}\left(t_3 + \omega^{-n} t_1 \hat{T}_{\mathbf{a}_1} + \omega^n t_2 \hat{T}_{\mathbf{a}_2}\right) b_{m,n} + \text{H.c.} \tag{3.2}$$

$\omega = e^{2\pi \mathrm{i}\frac{p}{q}}$ and $\hat{T}_{\mathbf{a}_{1,2}}$ are the translation operators on the $\mathbf{a}_{1,2}$ directions. The gauge fixing breaks the lattice translation symmetry $\hat{T}_{\mathbf{a}_2}$ and preserves $\hat{T}_{\mathbf{a}_1}$. We recognize the magnetic translations $\hat{T}_1 = \hat{T}_{\mathbf{a}_1}, \hat{T}_2 = \hat{T}_{\mathbf{a}_2} e^{2\pi i B n/\phi_0}$ that commute with the Hamiltonian Eq. (3.2), but yield a different commutation relation between each other:

$$\hat{T}_1 \hat{T}_2 = \omega \hat{T}_2 \hat{T}_1. \tag{3.3}$$

We can thus define a effective magnetic unit cell by expanding the original unit cell q times in the $\mathbf{a}_2$ direction by noticing that the operators $\hat{T}_1$ and $(\hat{T}_2)^q = (\hat{T}_{\mathbf{a}_2})^q$ commute(see Fig. 3.1a). The magnetic unit cell establishes an effective tight-binding description with $2q$ sites per magnetic unit cell, $(a^s_{\mathbf{r}}, b^s_{\mathbf{r}})$, where $s = 0, ..., q-1$, and lattice translation vectors $\{\tilde{\mathbf{a}}_1, \tilde{\mathbf{a}}_2\} = \{\mathbf{a}_1, q\,\mathbf{a}_2\}$. In momentum space, we readily find

$$H = -\sum_{\mathbf{k}\in \mathrm{MBZ}} \psi^\dagger_{\mathbf{k}} \begin{pmatrix} 0 & h_{\mathbf{k}} \\ h^\dagger_{\mathbf{k}} & 0 \end{pmatrix} \psi_{\mathbf{k}} = -\sum_{\mathbf{k}\in \mathrm{MBZ}} \psi^\dagger_{\mathbf{k}} \tau_1 \otimes h_{\mathbf{k}} \psi_{\mathbf{k}}\,, \tag{3.4}$$

in the Fourier basis $\psi_{\mathbf{k}} = (a^0_{\mathbf{k}}, ..., a^{q-1}_{\mathbf{k}}, b^0_{\mathbf{k}}, ..., b^{q-1}_{\mathbf{k}})^T$. The non-zero elements $h_{\mathbf{k}}$ given as follows:

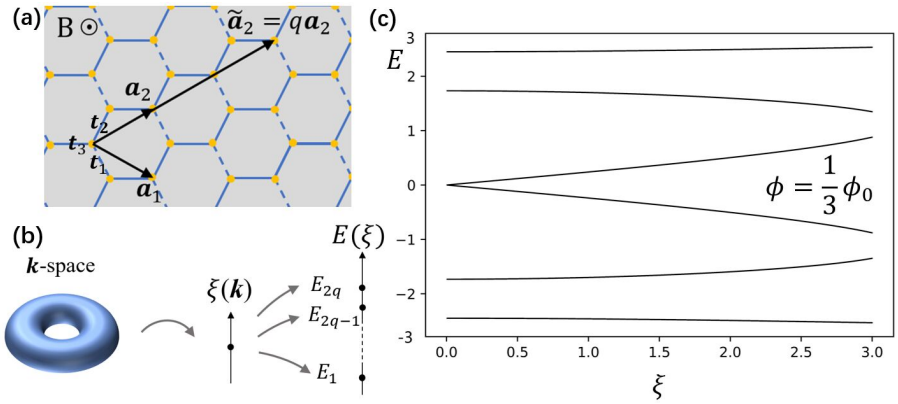

Figure 3.1: textbf(a) Honeycomb superlattice with lattice constant a in the nms and magnetic unit cell q times extended along $\mathbf{a}_2$. **(b)** Momentum dependence on the Thouless function ξ. **(c)** Spectrum as function of ξ for $\phi = (1/3)\phi_0$.

$$
\begin{aligned}
(h_{\mathbf{k}})_{ss} &= t_3 + t_1\, e^{ik_1}\, \omega^{-s}\,, \quad s = 0, ..., q-1\,, \\
(h_{\mathbf{k}})_{s,s+1} &= t_2\, \omega^{s}\,, \quad s = 0, ..., q-2\,, \\
(h_{\mathbf{k}})_{q-1,0} &= t_2\, \omega^{q-1}\, e^{ik_2}\,,
\end{aligned}
\tag{3.5}
$$

where $\mathbf{k} = k_1\, \tilde{\mathbf{g}}_1 + k_2\, \tilde{\mathbf{g}}_2$, with $k_i \in [-\pi, \pi)$, denotes the momenta inside the magnetic Brillouin zone (MBZ) with $\tilde{\mathbf{g}}_1 = \frac{1}{3}\hat{x} - \frac{1}{\sqrt{3}}\hat{y}$ and $\tilde{\mathbf{g}}_2 = \frac{1}{q}(\frac{1}{3}\hat{x} + \frac{1}{\sqrt{3}}\hat{y})$ being the reciprocal vectors in Cartesian coordinates satisfying $\tilde{\mathbf{a}}_i \cdot \tilde{\mathbf{g}}_j = \delta_{ij}$.

3.3 Self-similarity of the Hofstadter Spectrum

In this section, we establish a universal function for the Hofstadter spectrum on the honeycomb lattice that will be useful in understanding the self-similarity of the Hofstadter bands. Aiming at a non-perturvative description of the Hofstadter-Chern bands beyond the isotropic lattice $t_1 = t_2 = t_3$[158, 161, 178], we establish the spectral

function $\mathcal{P}(E) = \det(E\,\mathrm{I} - H)$,

$$\mathcal{P}(E) = \sum_{n=1}^{q} a_n(\{t_i\})\, E^{2n} - \xi^2(\{t_i\}, k_1, k_2)\,, \tag{3.6a}$$

$$\xi(\{t_i\}, k_1, k_2) = |t_1^q\, e^{\mathrm{i}q\,k_1 - \mathrm{i}\pi\,(q-1)} + t_2^q\, e^{\mathrm{i}k_2} + t_3^q| \geq 0\,. \tag{3.6b}$$

Notice that Eq.(3.6) encodes a remarkable property of the Hofstadter spectrum [originally noticed by Thouless in a different context[179] (see also[158])], namely, that the momentum dependence of the bands is "compressed" in a single function $\xi(\mathbf{k})$, i.e. $E_\alpha(\mathbf{k}) = E_\alpha(\xi(\mathbf{k}))$ for $\alpha = 1, ..., 2q$. Figs. 3.1b and 3.1c show how the energy bands depend on the "Thouless function" ξ, which we notice is related to the graphene band in zero magnetic field[30] upon the replacements $(k_1, k_2) \to (q\,k_1 - \pi(q-1), k_2)$ and $\{t_i\} \to \{t_i^q\}$.

We prove explicitly that the momentum dependence of the spectral function appears only in the zero-order coefficient, $a_0 = -\xi^2 = (-1)^{q-1}\det(H)$. By examining the matrix elements given by Eq. (3.5), we notice that the dependence on k_2 appears only in $(H_\mathbf{k})_{q-1,q} = (h_\mathbf{k})_{q-1,0}$ and $(H_\mathbf{k})_{q,q-1} = (h_\mathbf{k}^\dagger)_{0,q-1}$. As such, these two elements only contribute to the coefficient $a_0 = -\xi^2 = (-1)^{q-1}\det(H)$ of the characteristic polynomial:

$$\begin{aligned}
a_0 \quad &= (-1)^{q-1}\det(H) \\
&= -\prod_{s=0}^{q-1} |t_3 + t_1\omega^s \mathrm{e}^{-ik_1}|^2 - |\mathrm{e}^{ik_2}\prod_{s=0}^{q-1} t_2\omega^s|^2 - (\mathrm{e}^{ik_2}\prod_{s=0}^{q-1} t_2\omega^s(t_3 + t_1\omega^s\mathrm{e}^{-ik_1}) + \mathrm{h.c.}) \\
&= -t_3^{2q} - t_1^{2q} - (t_3^q t_1^q(-1)^{q-1}\mathrm{e}^{-iqk_1} + \mathrm{h.c.}) - t_2^{2q} \\
&\quad -(t_2^q t_3^q \mathrm{e}^{ik_2} + t_2^q t_1^q(-1)^{q-1}\mathrm{e}^{i(k_2 - qk_1)} + \mathrm{h.c.}) \\
&= -|t_1^q \mathrm{e}^{i((q-1)\pi - qk_1)} + t_2^q \mathrm{e}^{-ik_2} + t_3^q|^2 \\
&= -\xi^2
\end{aligned} \tag{3.7}$$

Now we transform to another gauge $\mathbf{A}' = \hat{y}(x - \sqrt{3}y)B$, which extends the honeycomb unit cell in the $\mathbf{a}_1$ direction instead of $\mathbf{a}_2$. Consequently, we have exchanged the momentum components k_1 and k_2 so that now the only k_1-dependent coefficient is a_0. Therefore, we have proven that the only $\mathbf{k}$-dependent coefficient in the characteristic polynomial is $a_0 = -\xi^2$. The momentum independent coefficients $a_n(\{t_i\})$, $n = 1, ..., q$ can be determined recursively via Faddeev–LeVerrier algorithm. We present our results for $p = 1$, $q = 3, 4, 5$ as examples:

For $p/q = 1/3$:

$$\begin{aligned} a_1 &= 3(t_1^4 + t_2^4 + t_3^4 + t_2^2 t_3^2 + t_1^2 t_2^2 + t_1^2 t_3^2) \\ a_2 &= -3(t_1^2 + t_2^2 + t_3^2) \\ a_3 &= 1\,. \end{aligned} \tag{3.8}$$

For $p/q = 1/4$:

$$\begin{aligned} a_1 &= (t_1^6 + t_2^6 + t_3^6) + t_1^4(t_2^2 + t_3^2) + t_2^4(t_1^2 + t_3^2) + t_3^4(t_1^2 + t_2^2) + 2t_1^2 t_2^2 t_3^2 \\ a_2 &= -6(t_1^4 + t_2^4 + t_3^4) - 8(t_1^2 t_2^2 + t_1^2 t_3^2 + t_2^2 t_3^2) \\ a_3 &= 4(t_1^2 + t_2^2 + t_3^2) \\ a_4 &= -1\,. \end{aligned} \tag{3.9}$$

For $p/q = 1/5$:

$$
\begin{aligned}
a_1 &= 5(t_1^8 + t_3^8 + t_2^8) + 5(t_1^6(t_2^2 + t_3^2) + t_2^6(t_3^2 + t_1^2) \\
&+ t_3^6(t_1^2 + t_2^2)) + 5(t_1^4 t_2^4 + t_2^4 t_3^4 + t_1^4 t_3^4) \\
&+ \frac{15 + 5\sqrt{5}}{2} t_1^2 t_2^2 t_3^2 (t_1^2 + t_2^2 + t_3^2) \\
a_2 &= -10(t_1^6 + t_2^6 + t_3^6) - 15(t_1^4(t_2^2 + t_3^2) + t_2^4(t_1^2 + t_3^2) + t_3^4(t_1^2 + t_2^2)) \\
&- \frac{45 + 5\sqrt{5}}{2} t_1^2 t_2^2 t_3^2 \\
a_3 &= 10(t_1^4 + t_2^4 + t_3^4) + 15(t_1^2 t_2^2 + t_1^2 t_3^2 + t_2^2 t_3^2) \\
a_4 &= -5(t_1^2 + t_2^2 + t_3^2) \\
a_5 &= 1 \,. \qquad (3.10)
\end{aligned}
$$

The mapping from Thouless function $\xi(\{t_i\}, k_1, k_2)$ to the bands $\{E_\alpha(\xi), \alpha = 1, ..., 2q\}$ imposes strong constraints upon the Hofstadter-Chern bands. Notice importantly $\nabla E_\alpha[\xi(\mathbf{k})] = dE/d\xi \nabla \xi(\mathbf{k})$, such that Thouless function determines the position of the band extremal and saddle points of all bands for the system with arbitrary rational flux $\phi = \frac{p}{q}\phi_0$. We show in Fig. 3.2 the extremal and saddle points of $\xi(\{t_i\}, k_1, k_2)$ for $q = 1$ in the two relevant hopping parameter regime $t_2 = t_3 = 1, t_1 < 2$ and $t_1 > 2$. The behavior of the energy bands $E_\alpha(\xi)$ for $q > 1$ can thus be similarly derived upon the appropriate replacement $(k_1, k_2) \to (q\, k_1 - \pi(q-1), k_2)$ and $\{t_i\} \to \{t_i^q\}$. Moreover, due to particle-hole symmetry, we are led to consider only the bands above charge-neutrality and define the band index $\beta \equiv \alpha - q$. Therefore, when $0 < t_1 < 2^{1/q}$, the band minimum (maximum) and maximum (minimum) for β odd (even) occur, respectively at $\xi(\mathbf{k}_{0\pm}^{(n)}) = \xi_{min} = 0$ and $\xi(\mathbf{k}_{max}^{(n)}) = \xi_{max} > 0$, where $\mathbf{k}_{0\pm}^{(n)} = ([\pm \arccos(-t_1^q/2) + \frac{\pi(2n+q-1)}{q}], \pm 2 \arccos(-t_1^q/2))$ and, furthermore, $\mathbf{k}_{max}^{(n)} = (\pi(2n+q-1)/q, 0)$. When $t_1 > 2^{1/q}$, $\xi(\mathbf{k}) > 0$ and the minimal of the β-odd bands and the maximal of the β-even bands are fixed in $\mathbf{k}$-space at the $\mathbf{M}_2^{(n)}$ points. We can further infer (i) that when $t_1 < 2^{\frac{1}{q}}$, the isolated energy bands

satisfy $dE/d\xi = 0$ at $\xi_{\min} = 0$ so as to prevent the discontinuity in $\nabla E(\mathbf{k}_{0\pm}^{(n)})$ and (ii) that the $t_1 < 2^{\frac{1}{q}}$ Chern transitions in the system happen at $\xi(\mathbf{k}_{max}^{(n)}) = \xi_{max} = |2+t_1^q|$, where $|dE/d\xi| \to \infty$ indicates the presence of q Dirac cones in the points $\mathbf{k}_{max}^{(n)}$ of the the magnetic Brillouin zone.

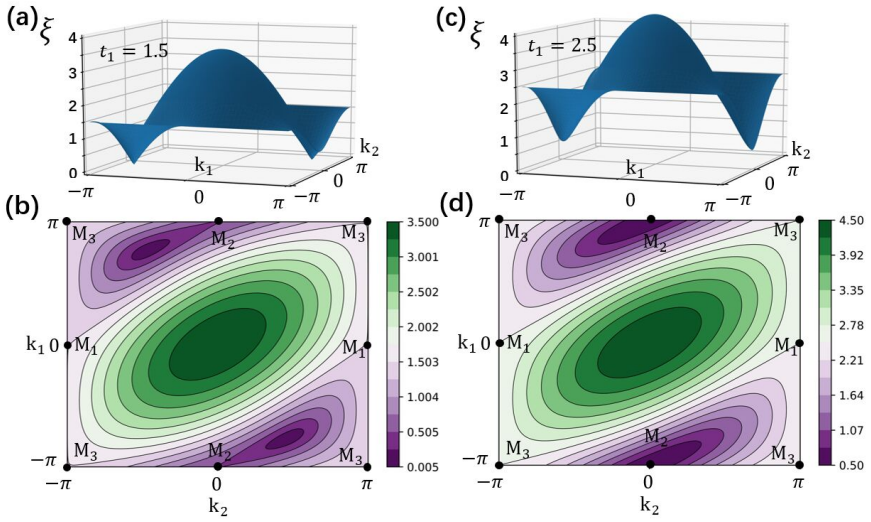

Figure 3.2: **(a)** Thouless function $\xi(\mathbf{k})$ with $q = 1$ (or equivalently $B = 0$) in the first Brillouin zone at $(t_1, t_2, t_3) = (1.5, 1, 1)$. **(b)** Contour plot of $\xi(\mathbf{k})$ with $q = 1$ at $(t_1, t_2, t_3) = (1.5, 1, 1)$. $\xi_{min} = 0$ at the Dirac points $\mathbf{k}_{0-} = -(\arccos(-0.75), 2\arccos(-0.75)) = (-2.41, 1.44)$ and $\mathbf{k}_{0+} = (2.41, -1.44)$. **(c)** $\xi(\mathbf{k})$ with $q = 1$ in the first Brillouin zone at $(t_1, t_2, t_3) = (2.5, 1, 1)$. **(d)** Contour plot of $\xi(\mathbf{k})$ with $q = 1$ at $(t_1, t_2, t_3) = (2.5, 1, 1)$. $\xi_{min} > 0$ at $\mathbf{M}_2 = (-\pi, 0)$. The behavior for $q > 1$ follows upon replacing $(k_1, k_2) \to (q\,k_1 - \pi(q-1), k_2)$ and $\{t_i\} \to \{t_i^q\}$.

3.4 Integer Hofstadter-Chern Insulator Transitions

In this section, we establish a classification of TPTs in the parameter space (t_1, t_2, t_3) taking advantage of the properties of Thouless function discussed in the previous section. On general grounds, consider a TPT tuned by the hopping parameters where two Chern bands touch at (ξ_F, E_F), where $\xi_F \neq 0$ and $E_F \neq 0$ is the Fermi energy. ($(\xi_F = 0, E_F = 0)$ band touchings will be discussed shortly after.) Let $\mathcal{P}(E) = \sum_{n=1}^{q} c_n \left(E^2 - E_F^2\right)^n - (\xi^2 - \xi_F^2)$ be the Taylor expansion of the characteristic polynomial Eq.(3.6a) about the band touching point. The even powers of E in Eq.(3.6a)

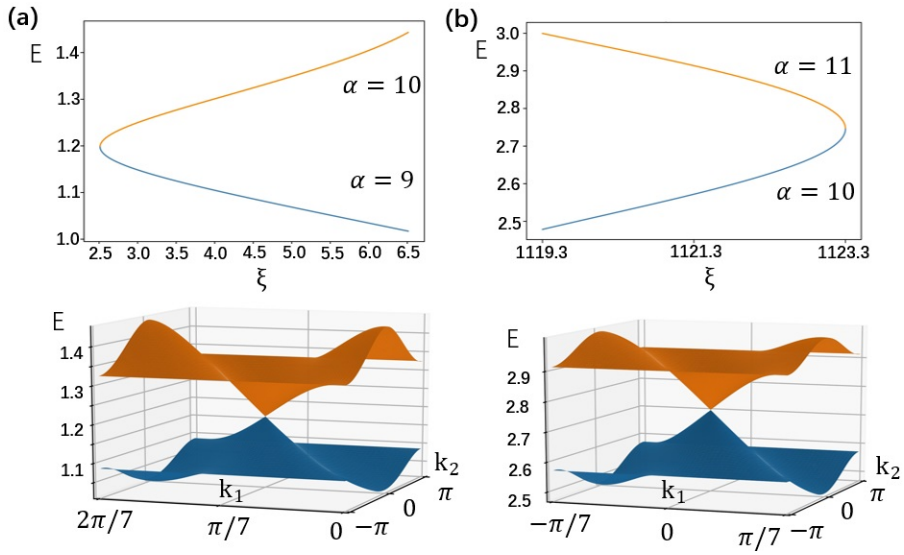

Figure 3.3: TPTs of the $\phi = (1/7)\phi_0$ lattice (α denotes band index). **(a)** At $(t_1, t_2, t_3) = (1.24, 1, 1)$, 7 Dirac cones (only one shown) form at $\mathbf{k}^{(n)}_{min} = (-\pi/7 + 2\pi n/7, 0)$, $n = 0, ..., 6$. **(b)** At $(t_1, t_2, t_3) = (2.73, 1, 1)$, 7 Dirac cones (only one shown) form at $\mathbf{k}^{(n)}_{max} = (2\pi n/7, 0)$, $n = 0, ..., 6$.

reflect the spectral particle-hole symmetry, and, since $\pm E_F \neq 0$ are doubly degenerate roots of the characteristic polynomial, it follows that $\mathcal{P}(E) = (E^2 - E_F^2)^2\, g(E)$, where $g(E)$ is a polynomial in E of order $2(q-2)$. This readily implies the coefficient $c_1 = 0$, leading to the relation in the vicinity of the touching point,

$$\xi \approx \xi_F + 2c_2 E_F^2 \xi_F^{-1} (E - E_F)^2\,, \quad \xi_F \neq 0\,. \tag{3.11}$$

Consequently, the sign of c_2 determines whether the transition occurs through the quadratic minimum ($\xi_F = \xi_{min} > 0$) or maximum ($\xi_F = \xi_{max} > 0$) of the Thouless function. Furthermore, upon expanding near the extremal points, i.e., $\xi(\mathbf{k}) \approx \xi_{min(max)} + \frac{a}{2}(\mathbf{k} - \mathbf{k}_{min(max)})^2$ [with $a > 0 (< 0)$ being the non-zero curvature at the quadratic minima (maxima)], and substituting onto Eq.(3.11), we obtain the dispersion

$$E - E_F = \pm v_F^* |\mathbf{k} - \mathbf{k}_{min(max)}|\,, v_F^* = (a\xi_F / 4c_2 E_F^2)^{1/2}\,, \tag{3.12}$$

characteristic of a Dirac cone centered at $\mathbf{k}_{min(max)}$. It can be shown that higher order band touchings are forbidden. Importantly, we establish below that ξ has q minima and maxima, implying a q-component Dirac transition. Fig. 3.3 presents two IHCI TPTs for $\phi = \phi_0/7$ that confirm the general behavior described in Eq.(3.11) and Eq.(3.12). The considerations above, therefore, uncover a non-trivial link between the classification of critical points and the global properties of the Thouless function, which we now address in detail.

Eq.(3.6a) establishes a one-to-one correspondence between the zero modes of ξ and band touchings at $E = 0$, where $E \approx \pm\xi/a_1^{1/2}$. Then, we directly determine from Eq.(3.6b) that the band structure with isotropic hoppings supports $2q$ Dirac touchings at $E = 0$[180–182] located at

$$\mathbf{K}_{\pm}^{(n)} = \left(\pm\frac{2\pi}{3q} + \frac{\pi}{q}(2n + q - 1)\,, \mp\frac{2\pi}{3} \right)\,, \tag{3.13}$$

for $n = 0, \cdots, q-1$, and, furthermore, that these band touchings persist as long as

$$\left| |t_i|^q - |t_j|^q \right| \leq |t_k|^q \leq \left| |t_i|^q + |t_j|^q \right| \tag{3.14}$$

where i, j, k are identified with any of the distinct values of $1, 2, 3$. Eq.(3.14) is the condition for $\xi = 0$, which, reproduces the stability of the pair of Dirac cones in graphene bands when $q = 1$.[183, 184] The global properties of the Thouless function lead to a remarkably simple classification of critical points:

(I) When condition (3.14) holds, $\xi \geq 0$ and there are $2q$ Dirac band touchings at $(\xi = 0, E = 0)$ as a consequence of particle-hole symmetry. Furthermore, TPTs at non-zero Fermi energy occur through q Dirac band touchings located at $\mathbf{k}_{max}^{(n)} = (\pi(2n + q - 1)/q, 0)\,,\ n = 0, ..., q-1$, where $\xi(\mathbf{k}_{max}^{(n)}) = \xi_{max}$. However, $\xi = \xi_{min} = 0$ transitions are forbidden at $E \neq 0$ by particle-hole symmetry.

(II) Outside the parameter space (3.14), $\xi > 0$ and the spectrum has a gap at half fill-

ing. The $2q$ zero modes of ξ merge pairwise forming q quadratic minima at one of the saddle points $\mathbf{M}_1^{(n)} = (\pi(2n+q-1)/q\,, -\pi\,)$, $\mathbf{M}_2^{(n)} = (-\pi/q + \pi(2n+q-1)/q\,, 0)$ or $\mathbf{M}_3^{(n)} = (-\pi/q + \pi(2n+q-1)/q\,, -\pi)$, for $n = 0, ..., q-1$. Then, $E_F \neq 0$ critical points are realized by q Dirac band touchings located either at ξ_{min} or ξ_{max}. Taking, for concreteness,

$$t_2 = t_3 = 1\,, \quad t_1 > 0\,, \tag{3.15}$$

leads to case (I) for $0 < t_1 \leq 2^{1/q}$ and case (II) when $t_1 > 2^{1/q}$, where the q degenerate minima of ξ are located at $\mathbf{k}_{min}^{(n)} = \mathbf{M}_2^{(n)}$, for $n = 0, ..., q-1$. The TPTs of Fig. 3.3 correspond to case (II) with the hopping parameters Eq.(3.15).

(III) The q Dirac fermions at quantum criticality are constrained by the action of magnetic translation, under which $(k_1, k_2) \to (k_1 + \frac{2\pi}{q}, k_2)$, and they account for the transfer of Chern number $\Delta\, C = \pm q$ between the bands, according to standard parity anomaly considerations.[185] We have performed extensive numerical calculations that confirm the properties (I), (II) and (III).

We now address an explanation on why transitions at $(\xi, E) = (0, E_F \neq 0)$ are forbidden in case (I). Let us begin by considering the band touchings at the particle-hole symmetric points $E = 0$. As discussed in the paragraph starting before Eq. (3.13), $E = 0$ band touchings occur whenever condition Eq. (3.14) is satisfied. So, as a consequence of particle-hole symmetry, there is an entire parameter regime where the two center bands touch at $E = 0$ forming $2q$ Dirac points localized at the zeros of ξ [the isotropic case was explicitly given in Eq. (3.13)]. To understand why $(\xi, E) = (0, E_F \neq 0)$ transitions do not occur, let us assume otherwise that two bands touch at such a point. The characteristic polynomial can be expressed as $\mathcal{P}(E) = c_2(E^2 - E_F^2)^2 - \xi^2 + \mathrm{O}((E^2 - E_F^2)^4)$, leading to the relation in the vicinity of this hypothetical touching point:

$$E = \pm\alpha\xi, \quad \alpha = (4c_2E_F^2)^{-1/2}\,, c_2 > 0\,.$$

So the assumed transition would have the same characteristics of the $2q$ Dirac touchings at $E = 0$. However, there is no particle-hole symmetry that protects these $E \neq 0$ transitions in parameter regime given by condition (3.14). Therefore, we find that the $(\xi, E) = (0, E_F \neq 0)$ transitions do not occur when condition (3.14) holds.

3.5 Van Hove Singularity Steering Mechanism

Having classified the IHCI critical points, we address in this section the *mechanism* underlying such phenomenon, which must account for $\Delta C = \pm q$ transitions in a spectrum composed primarily of bands which $C \sim O(1)$.

We argue and numerically demonstrate that $\Delta C = \pm q$ TPTs occur when Chern bands cross the energy scales associated with the van Hove singularities[73] of the DF band close to charge neutrality.

Van Hove singularities(VHSs) are topologically protected saddle points in Bloch bands, their energies correspond to the universal divergences in the density of states of the spectrum. For 2D lattices, the topological protection of VHSs is intuitively understood as the loss of connectedness when the energy contours travel through the energy scale of a Bloch band on the 2D Brillouin zone, which is homeomorphic to a torus. The divergence of the VHS in 2D is logarithm[73], which reads

$$g(E) \propto \log(\frac{\Lambda}{|E - E_{\text{VHS}}|}), \tag{3.16}$$

where Λ is an energy cutoff around the VHS. Further more, VHSs characterize the transition from particle-like to hole-like dispersions in the energy spectrum. In the vicinity of the VHS energies, the behavior of the electrons change drastically. These properties inspire us to relate the TPTs under the tuning of hopping parameters to the shift of VHSs across the spectrum. In what follows, we shall demonstrate how the VHS "steers" the TPTS across Hofstadter-Chern bands using the hopping t_1 in

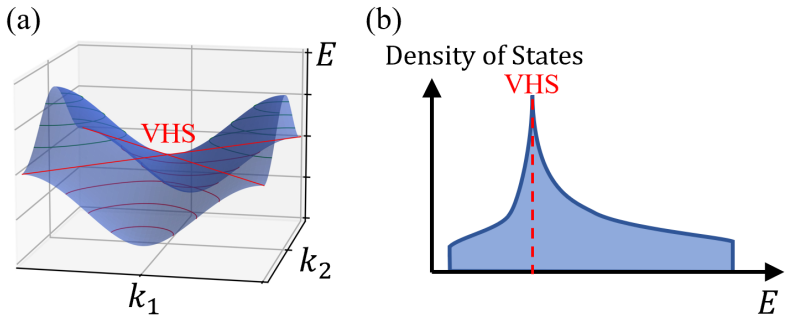

Figure 3.4: **(a)** The VHS in a 2D Bloch band, characterized by the loss of connectedness of the energy contours. **(b)** The logarithmic divergence of the DOS at VHS energy.

(3.15) as the tuning parameter.

To unearth the connection between VHS and TPTs, we consider two Hofstadter systems, denoted A and B, with fluxes $\phi_A = p_A/q_A$ and $\phi_B = p_B/q_B$ [henceforth we set $h = e = 1$ such that $\phi_0 = 1$ and $\phi \sim \phi$ mod (1)]. Furthermore, we impose the conditions (a) $|(\phi_A - \phi_B)/\phi_0| << 1$ and (b) $q_B \gtrapprox q_A$, which associate the spectrum of B with sub-bands of the A system that arise due to a small residual flux. By this construction, the B bands away from the VHS energy $E^A_{\rm VHS}$ behave as pseudo-LLs (pLL) of the A system with $C_{\rm pLL} \sim O(1)$. Consequently, we argue, and numerically confirm, that $E^A_{\rm VHS}$ provides the natural energy scale supporting non-trivial VHS-Chern bands of B with $C_{\rm VHS} \sim O(q_B)$. Therefore, the dependence of $E^A_{\rm VHS}$ on hopping parameters reveals the location of the non-trivial TPTs of B characterized by $\Delta C = \pm q_B$.

To gain further insight on the relation between VHS and TPTs, we initially consider system A with $t_i = 1$, which displays $2q_A$ DFs at half-filling with $E^A_{Dirac}(\mathbf{k}) \approx \xi_A(t_i = 1; \mathbf{k} - \mathbf{K}_\pm)/a_1^{1/2}$; see Eq.(3.13). Due to particle-hole symmetry, we focus on $E \geq 0$ bands. General considerations give the Dirac-like density of states (DOS) $D_A \propto E$ near charge neutrality, which is cut off by the VHS energy $E^A_{\rm VHS}$ that distinguishes electron-like from the hole-like states. Fig. 3.5a displays the DOS of this band for $\phi_A = 1/4$, which supports 8 Dirac fermions and has $E^A_{\rm VHS} \approx 0.15$. Notice

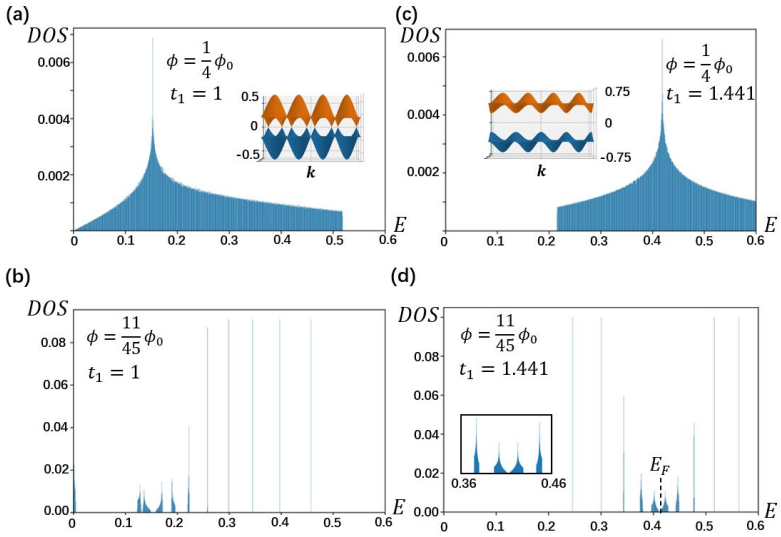

Figure 3.5: **(a)** DOS of the Dirac center band at $\phi_A = (1/4)\phi_0$ and $(t_1, t_2, t_3) = (1, 1, 1)$. Inset: 8 gapless DFs with locations given by Eq.(3.13). **(b)** DOS at $\phi_B = (11/45)\phi_0$ and $(t_1, t_2, t_3) = (1, 1, 1)$ reflecting the reconstruction of the Dirac band in (a). **(c)** DOS of the Dirac center band at $\phi_A = (1/4)\phi_0$ and $(t_1, t_2, t_3) = (1.441, 1, 1)$. Inset: 8 gapped DFs with the gap-opening threshold $t_1 = 2^{1/4} \approx 1.19$. **(d)** DOS at $\phi_B = (11/45)\phi_0$ and $(t_1, t_2, t_3) = (1.441, 1, 1)$ reflecting the reconstruction of the gapped Dirac band in (c). Inset shows emergent Dirac fermions at the critical point.

that, compared to the graphene bands[30], the magnetic field pushes the VHS substantially closer to charge neutrality due to the splitting of the spectrum into $2q_A$ bands. Furthermore, conditions (a) and (b) ensure the spectrum of B near half-filling can be understood as the response of the DF band of A to a weak "residual" magnetic field, which is expected to give rise to relativistic-like (non-relativistic-like) LLs for $E \lesssim (\gtrsim) E^A_{\text{VHS}}$. However, the B bands close to E^A_{VHS} deviate substantially from the LL behavior, confirming the behavior described in the paragraph above. This is illustrated in Fig. 3.5b where the said bands of the $\phi_B = 11/45$ system show more pronounced bandwidths and narrower gaps.

To understand how E^A_{VHS} tracks the TPTs of the B system, we study the the dependence of Thouless function on the hopping parameters. The property $E_\alpha(\mathbf{k}) = E_\alpha(\xi(\mathbf{k}))$ establishes that the VHS of the Chern bands locate on the saddles of ξ. Direct calculation shows that ξ is degenerate on all the saddle points $\mathbf{M}^{(n)}_{1,2,3}$ when

$t_1 = 1$ and, furthermore, that the degeneracy is partially broken for $t_1 \neq 1$.[186] For $1 < t_1 < 2^{1/q}$ (case (I) above), the VHS splits into a large peak at $E^A_{\mathrm{VHS},1} \equiv E^A(\mathbf{M}_1^{(n)})$ and a small peak at $E^A_{\mathrm{VHS},2} \equiv E^A(\mathbf{M}_2^{(n)})$. The latter disappears in the lower band edge, for $t_1 > 2^{1/q}$ (case (II) above), where an energy gap forms (Fig. 3.5c). Moreover, Fig. 3.5d (see inset) displays the onset of a TPT as the result of the VHS-Chern bands being steered by the $E^A_{\mathrm{VHS},1}$ energy scale.

The striking relationship between VHS and TPTs is shown in Fig. 3.6, where the bands of the $\phi_B = p_B/q_B = 11/45$ system near charge neutrality are plotted in the interval $t_1 \geq 1$. These bands originate as sub-bands of the $\phi_A = p_A/q_A = 1/4$ Dirac band in response to a small flux deviation $\delta\phi = -1/180$, as per conditions (a) and (b). We observe that the B bands formed near the band edges of system A behave as pLLs with vanishing bandwidth and $C_{\mathrm{pLL}} = -4$, while the VHS-Chern bands carrying $C_{\mathrm{VHS}} \sim O(q_B)$ form in the vicinity of E^A_{VHS}. Because E^A_{VHS} changes with the hopping parameters, the change in t_1 away from the isotropic point steers the VHS-Chern bands of B along the solid green ($E^A_{\mathrm{VHS},1}$) and purple ($E^A_{\mathrm{VHS},2}$) lines. This VHS steering mechanism reveals a sequence of TPTs (up arrows) characterized by $\Delta C = \pm 45$, with 45 emerging DFs located at the extremal points of the Thouless function of the system B, confirming the general properties (I), (II) and (III).

The Chern numbers in this section are numerically calculated via the algorithm developed in [187]. The idea is to approach the integral of the Berry curvature[23] efficiently by a discrete summation over the BZ. Consider the standard definition of the band Chern number[22]:

$$C_n = \frac{1}{2\pi} \int_{BZ} d^2k \mathcal{F}_{nxy}(\mathbf{k}) \,, \tag{3.17}$$

where the integral is perform in the first Brillouin zone. The Chern number is given

by the integral in momentum space of the gauge invariant Berry curvature

$$\mathcal{F}_{nij}(\mathbf{k}) = \partial_{k_i}\mathcal{A}_{nj}(\mathbf{k}) - \partial_{k_j}\mathcal{A}_{ni}(\mathbf{k}) \tag{3.18}$$

obtained from the curl of the Berry connection of the isolated band n,

$$\mathcal{A}_n(\mathbf{k}) = i\,\langle n, \mathbf{k}|\,\partial_{\mathbf{k}}\,|n, \mathbf{k}\rangle\ , \tag{3.19}$$

where $|n, \mathbf{k}\rangle$ is a Bloch state in the n-th band. In the discrete BZ, $\mathcal{A}_n(\mathbf{k})$ is replaced by the discrete gauge potential

$$A_{n\mu}(\mathbf{k}) = \ln[\langle n, \mathbf{k}|n, \mathbf{k} + \Delta k_\mu\rangle]\Delta k_\mu/2\pi \tag{3.20}$$

and $\mathcal{F}_{n12}(\mathbf{k})$ is replace by the discrete field strength

$$F_{n12}(\mathbf{k}) = \Delta_1 A_2(\mathbf{k}) - \Delta_2 A_1(\mathbf{k}) + i2\pi o_{n12}(\mathbf{k}) \tag{3.21}$$

where $\Delta_\mu f(\mathbf{k}) = [f(\mathbf{k} + \Delta k_\mu) - f(\mathbf{k})]/\Delta k_\mu$ is the difference along $\hat{\mu}$ direction. The integer value field $o_{n12}(\mathbf{k})$ equals to the winding number of the phase of $|n, \mathbf{k}\rangle$ around the minimal loop on the discrete BZ[187]. The numerical Chern number $\tilde{C}_n$ is given by the summation of $F_{n12}(\mathbf{k})$ over the discrete BZ:

$$\tilde{C}_n = \frac{1}{2\pi i}\sum_{\mathbf{k}\in BZ} F_{n12}(\mathbf{k}) \tag{3.22}$$

or equivalently

$$\tilde{C}_n = \sum_{\mathbf{k}\in BZ} o_{n12}(\mathbf{k}) \tag{3.23}$$

When Δk_μ is small enough, the numerical Chern number $\tilde{C}_n$ equals to the Chern number C_n. In practice, the Chern number is found by increasing the density of the

discrete BZ until the numerical result becomes robust. The results in this Chapter have been verified in a 500×500 discrete BZ with $\Delta k_1 = \Delta k_2 = \pi/250$.

Once the Chern number is found, the change of the Hall conductance at the TPT is expressed as $\sigma_H = \frac{e^2}{h} C$, where $C = \sum_{E_n < E_F} C_n$ is the gap Chern number below the Fermi energy E_F[22]. Recall that in our system $\Delta C = \pm q$, for a large q the Hall conductance changes drastically, giving rise to a measurable effect distinct from the conventional quantum Hall plateau transitions.

3.6 Fractional Hofstadter-Chern Insulator Transitions

In this section, we extend our analysis to FHCI transitions tuned by the hopping parameters in partially filled Chern bands via the standard representation of an FHCI with Hall conductance $\sigma_{xy}(C) = C/(2C+1)$ in terms of a composite fermion system [163–165] in an IHCI with $\sigma_{xy}^{CF} = C$[72, 117], which is subject to a mean field residual flux

$$\phi_{CF} = \phi - \phi_{CS}\,, \tag{3.24}$$

where $\phi = B\,\frac{\sqrt{3}}{2}a^2$ and $\phi_{CS} = 4n$ (the factor of 4 accounts for 2 attached flux quanta and 2 sites per unit cell) are, respectively, the intra-cell fluxes due to the external magnetic field and the Chern-Simons gauge field at lattice filling n, for $0 \leq n \leq 1$. Then, a TPT at fixed B and n between FHCIs with $\sigma_{xy}(C_1) = C_1/(2C_1+1)$ and $\sigma_{xy}(C_2) = C_2/(2C_2+1)$ can be effectively described by a $C_1 \to C_2$ composite fermion transition subject to the constraint $|C_2 - C_1| = q_{cf}$ (recall property (III)), where $\phi_{CF} = p_{cf}/q_{cf}$ is the flux of the composite fermion state. Furthermore, the relationship Eq.(3.24) between B and n allows the identification of candidate TPTs between Abelian FHCI states. In closing we present two such FHCI transitions re-

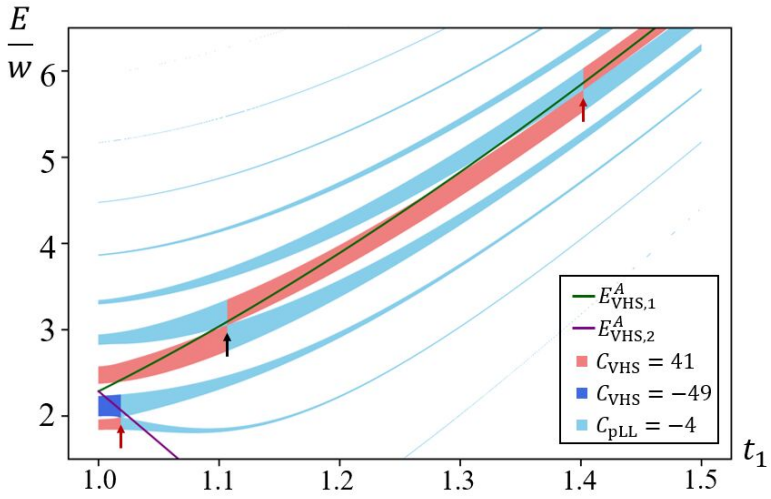

Figure 3.6: TPTs of system B ($\phi_B = 11/45$) steered by the VHS's of system A ($\phi_A = 1/4$). 11 B bands form near charge neutrality by splitting of the Dirac band of A in response to a flux deviation $\delta\phi = -1/180$, where 9 of these bands are shown. All energies are rescaled by the average band separation w of the B system with $t_1 = 1$. The Chern numbers of the bands are indicated by color coding. $E^A_{\mathrm{VHS},1}$ and $E^A_{\mathrm{VHS},2}$ are represented, respectively, by solid green and purple lines. The composite fermion (IHCI) TPTs at $n = 47/90$ and $n = 50/90$ ($n = 49/90$) are marked by vertical red (black) arrows.

alized when $\phi_{CF} = 11/45$, which are shown by vertical red arrows in Fig. 3.6. The first TPT is observed at $(t_1 \approx 1.02, n = 47/9, \phi = 1/3)$ and represents a transition between FHCIs with $\sigma_{xy}(37) = 37/75$ and $\sigma_{xy}(-8) = 8/15$. On the second transition at $(t_1 \approx 1.44, n = 50/90 = 5/9, \phi = 7/15)$, the Hall conductance jumps from $\sigma_{xy}(25) = 25/51$ to $\sigma_{xy}(-20) = 20/39$. In this section we present more examples of the relationship between the VHS of the Dirac fermion band near charge neutrality of system A and the onset of topological phase transitions of system B, where the fluxes of A and B are close to each other. We first recall that the VHS of the $B = 0$ (alternatively, $q = 1$) graphene band splits into two when the hopping parameter t_1 is tuned away from the isotropic lattice $t_1 = t_2 = t_3 = 1$. These VHS energies above

charge neutrality, $E_{\mathrm{VHS},1}$ and $E_{\mathrm{VHS},2}$, are given by

$$E_{\mathrm{VHS},1} = E(\mathbf{M}_1) = E(\mathbf{M}_3) = |t_1|, \tag{3.25}$$
$$E_{\mathrm{VHS},2} = E(\mathbf{M}_2) = |2 - t_1| \quad (t_1 < 2)\,.$$

If $t_1 > 2$, the Dirac points are gaped and $E_{\mathrm{VHS},2}$ disappears at the lower band edge. As an example, the DOS of the graphene band at different t_1 values is shown in Fig. 3.7.

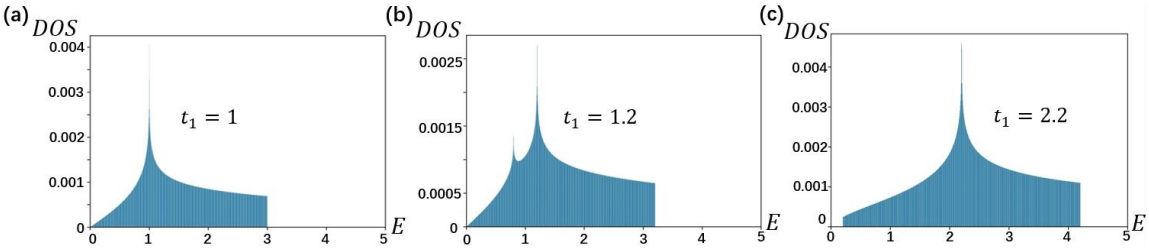

Figure 3.7: **(a)** The $B = 0$ density of states at $(t_1, t_2, t_3) = (1, 1, 1)$. **(b)** The $B = 0$ density of states at $(t_1, t_2, t_3) = (1.2, 1, 1)$. The VHS split into two for $0 < t_1 < 2$. **(c)** The $B = 0$ density of states at $(t_1, t_2, t_3) = (2.2, 1, 1)$. The Dirac point is gaped and only $E_{\mathrm{VHS},1}$ is left.

The pattern of VHS splitting due to tuning the hopping parameters also persists to the Chern bands as a consequence of the implicit momentum dependence on Thouless function. In fact, the phenomenon associated with the VHS steering of Chern bands is observed either when $\phi_A = 0$ or when there is a non-trivial flux per unit cell. As argued in the main text, the following conditions must be satisfied: (a) For the steered system B (which undergoes Chern transitions) and the steering system A (which provides the "background" van Hove singularities), $[(\phi_B - \phi_A)/\phi_0] \ll 1$ and (b) $q_B \gtrapprox q_A$. We can understand the phase transitions of the system with $\phi_B = 1/q_B$ (with $q_B > 1$), in terms of the VHS of system A in zero magnetic field. Below, we give concrete examples, one in Fig. 3.8, which shows the Chern transitions of the $\phi_B = 1/7$ system and the second one in Fig. 3.9, which corresponds to a composite fermion transition at $\phi_{CF} = 1/15$ and $n = 19/30$. In both cases, we see a clear

relationship between the onset of phase transitions and the VHS of the $B = 0$ band. Furthermore, we point out that the VHS steering mechanism extends to some degree beyond the Dirac bands near charge neutrality discussed in the main text, as shown in Fig. 3.10 for $\phi_A = 1/3$ and $\phi_B = 12/35$, albeit the mechanism for higher bands seems more sensitive to the narrow bandwidth of the Chern bands.

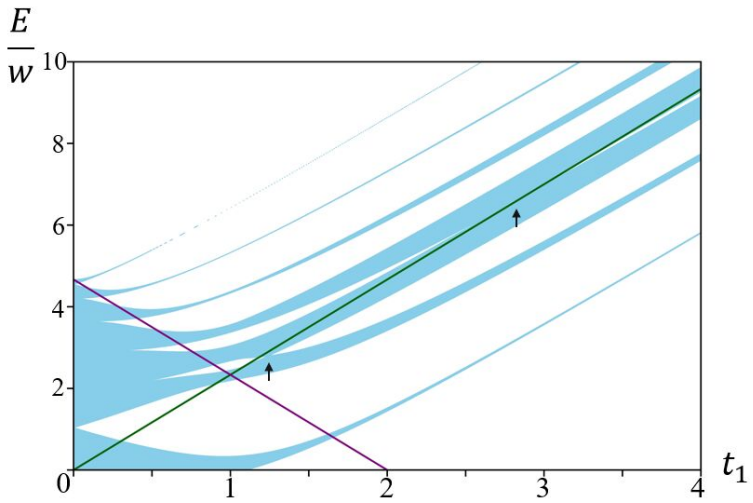

Figure 3.8: $\phi = 1/7$ TPTs steered by the $B = 0$ VHS's. The green line shows the van Hove singularity $E_{\mathrm{VHS},1}$ and the purple line showing $E_{\mathrm{VHS},2}$. Here $w = 3/7$ is the average energy separation of bands of the $\phi = 1/7$ spectrum at $t_1 = t_2 = t_3 = 1$. The TPTs are pointed out with black arrows.

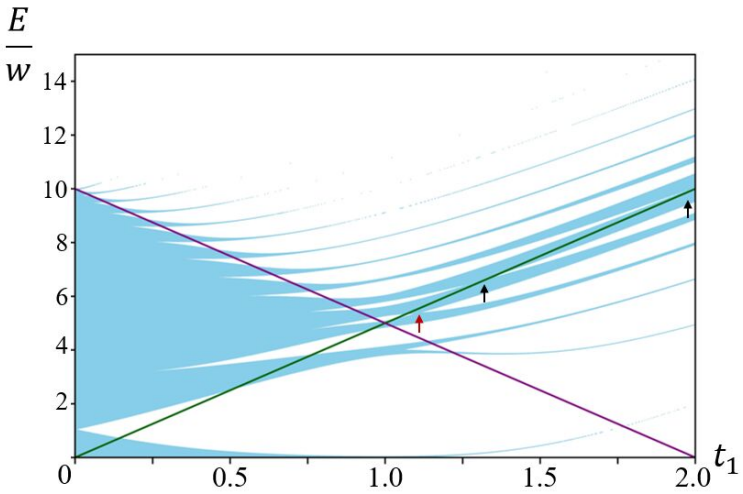

Figure 3.9: $\phi_B = 1/15$ TPTs steered by the $B = 0$ VHS's. The green line shows the van Hove singularity $E_{\text{VHS},1}$ and the purple line showing $E_{\text{VHS},2}$. Here $w = 1/5$ is the average energy separation of bands of the $\phi = 1/15$ spectrum at $t_1 = t_2 = t_3 = 1$. The phase transitions are pointed out with vertical arrows, with the red arrow indicating the composite fermion phase transition.

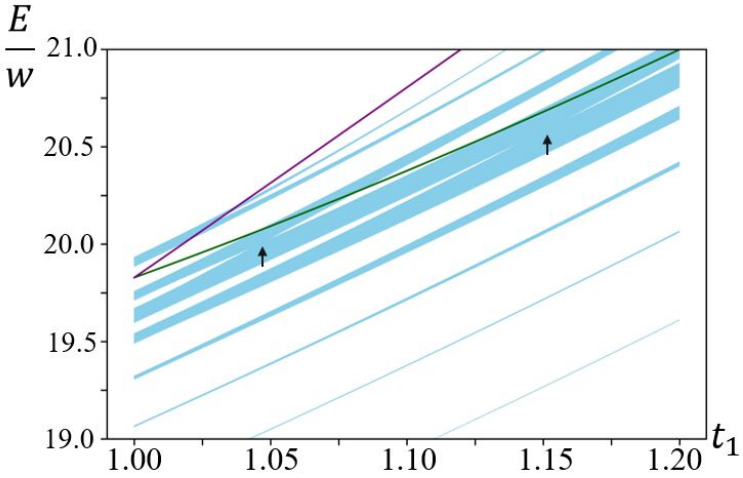

Figure 3.10: $\phi_B = 12/35$ TPTs steered by the $\phi_A = 1/3$ VHS's of the 2nd band above charge neutrality as an example of the non-Dirac steering. The green line shows the van Hove singularity $E_{\text{VHS},1}$ and the purple line showing $E_{\text{VHS},2}$. Here $w = 3/35$ is the average energy separation of bands of the $\phi_B = 12/15$ spectrum at $t_1 = t_2 = t_3 = 1$. The TPT is pointed out with the black arrow. Notice that the band touchings deviates a little bit from $E_{\text{VHS},1}$ suggesting a more complex mechanism behind the non-Dirac TPTs, presumably associated with a narrower band.

3.7 Summary and Discussion

The main contributions presented in this chapter are:

- We established a universal spectral function called the Thouless function encoding the self-similarity of the Hofstadter bands on a honeycomb lattice. Using the Thouless function, we established an analytical framework to classify multi-flavor Dirac fermion critical points describing hopping-tuned TPTs of integer and fractional Hofstadter-Chern insulators in honeycomb superlattices. Our classification sets firm constraints on the number of Dirac flavors as well as their momentum space distribution in terms of the hopping parameters, the magnetic flux per unit cell and the electron density.

- We found critical points realizing large transfers of Chern number across the TPTs that are distinct from conventional quantum Hall plateau transitions, which can in principle be detected via Hall conductivity measurements. The multi-flavor DFs associated with the critical points has provided an ideal platform for the Hofstadter superconductivity, which exhibits rich phase diagram at large magnetic fields, see follow up study in[61, 188].

- We proposed a new mechanism relating the energy scales of the van Hove singularities to the onset of the TPTs near charge neutrality. This result provides a new understanding to the emergence of topological quantum criticality in a fractal spectrum.

This work opens many interesting directions to study quantum critical phenomena in superlattices. Besides nanopatterned graphene superlattices [172–177] that served as a motivation for our work, van der Waals heterostructures in external magnetic field[45, 95, 108, 109] provide promising platforms to realize topological quantum criticality via strain induced tuning of the effective hopping parameters. Also, the

interplay of magnetic field and higher order VHS's[189, 190] can potentially provide even richer critical phenomena.

Chapter 4

Theory of Hofstadter Superconductors

4.1 Overview

Superconductivity is a phase of matter where upon cooling below a critical temperature T_c, electrons form a collective condensate that is capable of carrying currents with no dissipation. Discovered more than a century ago by Onnes, superconductivity has remained an evergreen subject of condensed matter physics. In addition to zero-dissipation, superconductors are also known to exhibit the Meissner effect[191], namely, an applied magnetic field is completely expelled from the interior of a superconductor. With these two central properties, the phenomenon of superconductivity had long been a puzzle to condensed matter physicists until 45 years after its discovery, when Bardeen, Cooper and Schrieffer resolved the underlying mechanism with the remarkable BCS theory[192], in which phonons provide the fundamental interaction for electron pairing, giving rise to a rigid condensate of electron pairs against perturbations. However, as most of the research had focused on the conventional superconductors that are described by the BCS theory, starting in the 1970s, a number

of unconventional forms of superconductivity have been discovered in connection with electronic interactions[79, 193–197]. Unconventional superconductors can violate the BCS description in many aspects. For example, some of them have extremely high T_c[134, 136, 138, 198], some others reemerge in high magnetic fields where conventional superconductivity is destroyed, which is known as re-entrant superconductivity [62, 145–156, 199]. Moreover, a class of unconventional superconductors are found to be topological, for the presence of chiral Majorana excitations on the boundary of the systems[200–204].

In the 1990s, a deep connection between unconventional superconductivity and fractional quantum Hall effect[10, 11, 14, 15] has been revealed. The properties of fractional quantum Hall states arise from correlations between bound states of electrons and magnetic fluxes[163–165]. When a electron is attached with a even number of flux quanta, it becomes a quasi particle dubbed a composite fermion. The energy spectrum of electrons thus reorganizes into that of composite fermions with a changed net magnetic field. While most of the fractional quantum Hall states are associated with energy spectrum in which composite fermions fill up an integer number of Landau levels, in the even denominator fractional quantum Hall states, such as the 5/2 state[205–218], the attachment of two flux quantum per active electron produces a state of composite fermions that experience zero average magnetic field, yielding a free particle spectrum similar to a 2D metal. Remarkably, Moore and Read[219] pointed out that the condensation of composite fermions into a chiral p-wave superconductor would account for the universal properties of such paired fractional quantum Hall states, in particular, this novel superconductivity turned out to be topological.

Recent experimental progress in realizing Hofstadter bands in moiré materials[1, 2, 45, 47–49, 109] invites into consideration the nature of electronic pairing in a scenario where magnetic fields and lattice effects are strongly coupled, producing drastic deviations from the Landau level regime. Concerning with the possibility of uncon-

ventional superconductivity in Hofstadter bands, we address a fundamental question in this chapter: *what is the effect of the fractal band structure on electronic pairing, regardless of the underlying microscopic mechanism of the superconducting state?* To answer this question, we establish a theoretical framework to classify the electronic pairing states in Hofstadter bands with a symmetry-based approach, and show that such Hofstadter superconductivity supports rich phase diagrams and unconventional excitations. Our findings contributes to further current knowledge about the relationship between topological superconductivity and fractal band structures.

Hofstadter systems possess rich single particle properties. In contrast to flat Landau levels obtained as the limit of Hofstadter bands when the flux per unit cell Φ is orders of magnitudes lower than the flux quantum Φ_0, Hofstadter bands have finite bandwidths and are characterized by a wider range of Chern numbers, which gives way to unconventional quantum critical phenomena controlled by lattice effects [58, 60]. Moreover, Hofstadter band structure non-trivially depends on the magnetic flux per unit cell, which can be controlled by tuning the strength of the external magnetic field. All these properties combined make the microscopic analysis of the electron pairing problem rich, yet involved. However, we show in this chapter that it is possible to extract universal properties of Hofstadter superconductors despite the complexity of the single particle states. To that purpose, we pursue a symmetry based approach that captures the essential features of Hofstadter systems and, thus, leads to a general framework describing the thermodynamic properties of superconductivity in a regime dominated by the strong interplay between magnetic fields and lattice effects.

In this chapter, we focus on describing the symmetry properties of the pairing order parameter $\hat{\Delta}_{ab} \propto \langle \psi_a \psi_b \rangle$ under U(1) and magnetic translation symmetries for a general Hofstadter lattice with magnetic flux $\Phi = (p/q)\Phi_0$ per unit cell, with p and q coprime integers. In Hofstadter models, the magnetic translation group (MTG)

is generated by non-commuting lattice translation operators in the presence of a magnetic field [91–93] and plays an essential role in our symmetry analysis of the superconducting order parameter. A key result of this chapter is establishing the properties of the irreducible representations (irreps) of the MTG furnished by the charge $2e$ pairing fields $\hat{\Delta}$, and showing that they are different from the well-known q-dimensional irreps of the MTG furnished by single particle Bloch states [91–93]. Specifically, while the irreps furnished by the pairing order parameter have the same dimension q for odd q, for even q there are four distinct irreps of dimension $q/2$. In fact, as pointed out in [220], the possibility of such charge 2e irreps has already been identified mathematically in [91] but were originally rejected as unphysical. We show that this property stems from the interplay between the generators of the U(1) group and the MTG, which are *simultaneously* broken in the Hofstadter charge 2e condensate. We emphasize that having a charge 2e order parameter is key to our findings. In particular, the paired states in fermionic Hofstadter systems analyzed here have different symmetry properties under the action of the MTG from those occurring in the *bosonic* Hofstadter model [55, 221–224] for which the order parameter $\langle b^\dagger \rangle$ is a charge 1e operator that furnishes irreps analogous to single particle Bloch states.

From the study of group representations stems a comprehensive Ginzburg-Landau phenomenological theory of Hofstadter superconductors for generic magnetic flux. The analysis shows that Hofstadter condensates are characterized by multi-component order parameters, uncovering an ideal scenario to explore a number of unconventional superconducting orders [193, 194] such as pair-density waves [64, 67, 225–228], multi-band chiral topological condensates beyond conventional chiral p-wave superconductors [200], as well as condensates with gapless fermionic excitations such as symmetry-protected critical points and Bogoliubov Fermi surfaces [121–132]. As such, our work in this chapter provides a symmetry-based framework to study thermodynamic phases

– and their corresponding phase transitions – realized by charge 2e condensates in the presence of large magnetic flux and lattice effects, establishing superconductivity in Hofstadter systems as a fertile setting to explore symmetry broken and topological orders.

Moreover, the analysis of irreps of the MTG shows that the Hofstadter superconducting phase behaves as a vortex lattice, in the sense that the phase of the components of the order parameter winds as a parallel transport takes place around the unit cell. Therefore, these findings provide a general framework that justifies the numerical observation of vortex lattices in fermionic [64, 67] and bosonic [55] Hofstadter systems. However, we note that the order parameter $\hat{\Delta}$ need not vanish anywhere in space, unlike in heterostructures combing quantum Hall systems and regular Abrikosov vortex lattices [66, 229–234]. In the limit $q \to \infty$, we expect the vortex lattice to approach the Abrikosov vortex lattice at the upper critical field H_{c2}.

The group theory classification of Hofstadter pairing discussed in this chapter sheds light on earlier studies of pairing in fermionic Hofstadter systems done mostly in the context of synthetic gauge fields in optical lattices of cold atoms [62, 64, 66, 67, 225, 226, 226, 227, 235–239]. All of these works carried out numerical analyses restricted to small values of q, with $\Phi = (p/q)\Phi_0$ being the flux per unit cell. Refs. [62, 64, 67] considered the role of MTG symmetries, noting that it implies the presence of order parameters with multiple finite pairing momenta similar to Fulde-Ferrell-Larkin-Ovchinnikov and pair-density wave phases [64, 67], and indicates translational symmetry breaking [228, 240–247]. Furthermore, earlier numerical observation [67] that some magnetic translation symmetries may also be broken is corroborated by our group theory analysis that shows that at least one magnetic translation symmetry is *necessarily* broken in the paired state, resulting in q- or $q/2$-fold degenerate ground states for odd and even q respectively [1]. We also show that the phase relations

[1] A similar result was found in [55] for charge 1e condensates in synthetic magnetic fields

between order parameters with different pairing momenta found in [64] for $q = 3$ and $q = 4$ result from an unbroken cyclic $\mathbb{Z}_q$ subgroup of the MTG, which also implies the coexistence of these order parameters as discussed in [64, 67, 225–227, 237]. We establish exact results for the phase relations for all values of q and note that at least a part of the MTG is broken in the paired state. The latter is reflected in the fact that the irreducible representations (irreps) of the MTG furnished by the order parameters of the paired state are multi-dimensional.

This chapter is organized as follows. In Sec. 4.2 we set our notation, review the action of the MTG on single particle electronic states, emphasising – see Fig. 4.1 – that the q dimensional irrep of the single particle states gives rise to q Fermi surface patches, which forms the low energy space for electronic pairing. We then discuss the constraints imposed by the MTG on interactions projected onto Hofstadter bands, thus providing an effective microscopic description for the pairing instability of Hofstadter electrons. In Sec. 4.3, we present a comprehensive classification of the MTG irreps furnished by the pairing matrix $\hat{\Delta}$. We show that the dimension of the irreps depends upon the parity of q: while the irreps furnished by the pairing order parameter have dimension q for odd q, for even q there are four distinct irreps of dimension $q/2$. We emphasize that while we use an effective microscopic model projected to a single band for illustration purposes, our symmetry-based analysis generalizes when multiple bands are present, including the strong-coupling regime. In particular, Sec. 4.4 presents a phenomenological Ginzburg-Landau theory of Hofstadter superconductors described by a multi-component order parameter, which reflects the multi-dimensionality of the irreps discussed in Sec. 4.3. We analytically and numerically analyse the phase diagram of some representative cases, discussing their symmetry breaking patterns. In particular, we discuss a class of $\mathbb{Z}_q$-symmetric Hofstadter superconductors formed when the MTG breaks down to a discrete $\mathbb{Z}_q$ subgroup resulting in ground state degeneracy equal to the dimension of the irrep. The remaining subgroup

may also be broken in the ground state, as we find numerically for $q \geq 5$, further enlarging the degeneracy of the ground state.

Finally, in Sec. 4.5 we analyse the spectrum of fermionic excitations of such $\mathbb{Z}_q$-symmetric Hofstadter superconductors, deriving some general results about the bulk topology and nature of quantum critical points. First, we show that chiral Hofstadter superconductors provide a natural setting for realizing topological superconductivity with tunable Chern numbers. We demonstrate, under general conditions, that particle-hole and parity symmetries constraint the change of the Chern number across quantum critical points to even values $\Delta C \in 2\mathbb{Z}$, implying the conservation of Chern number parity and therefore the non-Abelian character of bulk fermionic states. Furthermore, we show that when Hofstadter superconductors with $\mathbb{Z}_q$ MTG symmetry also possess parity symmetry, their spectrum *necessarily* supports Bogoliubov Fermi surfaces (BFS). For odd q, there is only one BFS, which is stable even if the $\mathbb{Z}_q$ symmetry is broken as long as particle-hole and parity symmetries are preserved and protected by the same topological invariant as constructed in [123]; for even q, there are two degenerate BFS when the gap function belongs to two out of the four irreps, but that are unstable if the $\mathbb{Z}_q$ symmetry is broken. The stability of the doubly degenerate BFS for even q is therefore protected by a new topological invariant that only exists in the presence of the $\mathbb{Z}_q$ symmetry, as we establish.

4.2 Hofstadter Systems and the Magnetic Translation Group

We consider a 2D electronic system in a perpendicular magnetic field $\mathbf{B}$ on a lattice with basis lattice vectors $\mathbf{a}_1$ and $\mathbf{a}_2$. We assume $\mathbf{a}_1$ points along the x-direction. As spin will play no role in the analysis of the MTG, we will consider spin polarized fermions for simplicity, but note that the analysis applies to systems with both spins

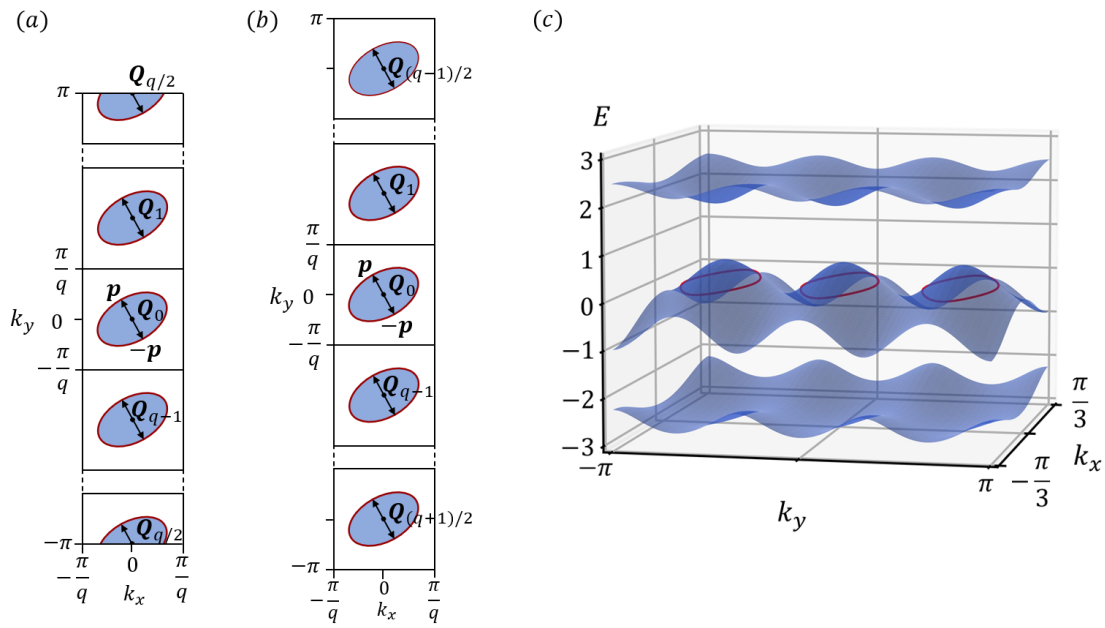

Figure 4.1: Brillouin zone and Fermi surfaces for a square lattice for (a) even and (b) odd q, and (c) the Hofstadter bands for the original Hofstadter tight binding model on a square lattice [3–5] for $q = 3$. A single band in the absence of the magnetic field splits into q bands, q-fold symmetric under translations by $\mathbf{Q}$. The red contours indicate the Fermi level that we take to be at $E = 0$. The Brillouin zone is folded along the k_x direction by a factor of q relative to the Brillouin zone in the absence of the magnetic field. Due to the $\hat{T}_1$ magnetic translation symmetry, the band structure repeats q times along the k_y direction. As a result, there are q copies of a Fermi surface centered at momenta $\mathbf{Q}_\ell = \ell\mathbf{Q}$. The interactions are projected onto the single band that crosses the Fermi level.

included. The primitive vectors of the reciprocal lattice are then $\mathbf{b}_1$ and $\mathbf{b}_2 = b_2\hat{\mathbf{y}}$ and we work with the vector potential $\mathbf{A} = xB\mathbf{a}_2/a_{2y}$ in the Landau gauge, where a_{2y} is the y component of $\mathbf{a}_2$. We further assume that the magnetic flux per unit cell is a rational multiple of the flux quantum: $\Phi = \frac{p}{q}\Phi_0$, with $\Phi_0 = h/e$. The unit cell is therefore extended by a factor of q along the x axis, and the Brillouin zone is folded along the $\hat{\mathbf{b}}_1$ direction by the same factor (see Fig.4.1). After the folding, in general each energy band in the absence of the magnetic field is split into q Hofstadter subbands [3, 4, 90–93] carrying non-trivial Chern numbers that depend on the particular lattice [22, 28].

The q-fold splitting of the bands can be understood from a symmetry perspec-

tive. The non-trivial vector potential breaks the translation symmetry T_1 of the lattice along the x direction, but the system remains symmetric under *magnetic* translation $\hat{T}_1$ that is a composition of T_1 and the gauge transformation $\mathbf{A}(x) \to \mathbf{A}(x) - Ba_1\mathbf{a}_2/(2a_{2y})$. Importantly, the two magnetic translation symmetries $\hat{T}_1$ and $\hat{T}_2 = T_2$ do not commute but satisfy $\hat{T}_1\hat{T}_2 = \omega_q^p \hat{T}_2\hat{T}_1$ where $\omega_q^p = e^{2\pi ip/q}$ is a q^{th} root of unity. Together $\hat{T}_1$ and $\hat{T}_2$ generate the magnetic translation group (MTG), which includes a subgroup of $U(1)$ transformations generated by the commutator $\hat{T}_1\hat{T}_2\hat{T}_1^{-1}\hat{T}_2^{-1} = \omega_q^p$. As a result of the non-commutativity of the MTG, its irreducible representations (irreps) formed by the electron states are q dimensional [91–93], and as a result the bands in the absence of the magnetic field split into q sub-bands with dispersions $\varepsilon_\alpha(\mathbf{k})$, the index $\alpha = 0, \ldots, q-1$ labeling the sub-bands being defined modulo q.[2] We assume that the dispersion is symmetric under inversion, $\varepsilon_\alpha(\mathbf{k}) = \varepsilon_\alpha(-\mathbf{k})$, which is necessary for the pairing instability.

We define $d_{\alpha\mathbf{k}}$ to be the second-quantized annihilation operators corresponding to the α sub-band. With our gauge choice, the quasimomentum component k_x can be restricted to $\left(-\frac{\pi}{q}, \frac{\pi}{q}\right]$ due to the folding of the Brillouin zone. Under the magnetic translations,

$$\begin{aligned} \hat{T}_1 d_{\alpha,\mathbf{k}} \hat{T}_1^\dagger &= e^{-ik_x} d_{\alpha,\mathbf{k}+\mathbf{Q}} \\ \hat{T}_2 d_{\alpha,\mathbf{k}} \hat{T}_2^\dagger &= e^{-i\mathbf{k}\cdot\mathbf{b}_2} d_{\alpha,\mathbf{k}} \end{aligned} \tag{4.1}$$

where $\mathbf{Q} = \frac{2\pi p}{q}\hat{\mathbf{b}}_2$. Notice that $\hat{T}_1$ therefore acts as a translation operator also on the reciprocal lattice, but along a perpendicular direction. As a result, each sub-band is q-fold degenerate within the Brillouin zone, $\varepsilon_\alpha(\mathbf{k}) = \varepsilon_\alpha(\mathbf{k} + \mathbf{Q})$, which reflects the fact that with a different gauge the unit cell could be extended along $\mathbf{a}_2$ instead of $\mathbf{a}_1$, with the Brillouin zone folded in the $\hat{\mathbf{b}}_2$ direction. Since the dispersion is gauge

[2]The irreducible representations of the MTG can also be considered as projective irreducible representations of the regular translation group.

invariant it must remain the same with both choices, and is therefore periodic in both directions (see Fig 4.1). Consequently, the Brillouin zone can be further folded along $\hat{\mathbf{b}}_2$, producing the reduced Brillouin zone in which each band is q-fold degenerate at each momentum (the unit cell in real space is correspondingly extended by a factor of $q \times q$). We therefore define $d_{\alpha,\mathbf{p},\ell} = d_{\alpha,\mathbf{p}+\ell\mathbf{Q}}$ with $\mathbf{p}$ restricted to the reduced Brillouin zone with the patch index $\ell = 0, \ldots, q-1$ (defined modulo q) labeling the degeneracy. With this relabeling and using Eq.(4.1), the magnetic translation symmetries act as matrices in patch indices

$$\begin{aligned} \hat{T}_1 d_{\alpha,\mathbf{p},\ell} \hat{T}_1^\dagger &= (\mathcal{T}_1)_{\ell\ell'} d_{\alpha,\mathbf{p},\ell'} \\ \hat{T}_2 d_{\alpha,\mathbf{p},\ell} \hat{T}_2^\dagger &= (\mathcal{T}_2)_{\ell\ell'} d_{\alpha,\mathbf{p},\ell'} \,, \end{aligned} \tag{4.2}$$

(with implicit summation over ℓ' on the RHS), with $\mathcal{T}_1 = e^{-ip_x}\hat{\tau}$ and $\mathcal{T}_2 = e^{-i\mathbf{p}\cdot\mathbf{b}_2}\hat{\sigma}^*$, where

$$\begin{aligned} \hat{\tau}_{\ell\ell'} &= \delta_{\ell,\ell'-1} \\ \hat{\sigma}_{\ell\ell'} &= \omega_q^{\ell p} \delta_{\ell\ell'} \end{aligned} \tag{4.3}$$

are the $q \times q$ shift and clock matrices, respectively. The transformation properties of electron operators described in Eq. (4.2) will play a central role in understanding the properties of the superconducting state; in particular, they will lead to a general understanding of the irreps realized by the superconducting gap function to be discussed in Sec. 4.3 that we will see are distinct from the single electron irreps relevant for the Hofstadter bands constructed in [91–93].

Projected Interactions

Although our symmetry analysis of superconductivity presented below is quite general and can be easily extended to include pairing between multiple bands α relevant in the strong-coupling regime, since the MTG symmetries act trivially on the band index as seen in Eqs. (4.1-4.2), it is sufficient to consider the pairing instability of the Fermi surfaces restricted to a single band α in the weak-coupling regime. We therefore consider a scenario where the chemical potential lies within a single band α and project general momentum-conserving pairing interaction Hamiltonian onto this band (with the α band index henceforth omitted)

$$H_{int} = \sum g^{(\ell)}_{nm}(\mathbf{p};\mathbf{p}') d^{\dagger}_{\mathbf{p},\ell+n} d^{\dagger}_{-\mathbf{p},-n} d_{\mathbf{p}',\ell+m} d_{-\mathbf{p}',-m} \,, \tag{4.4}$$

where $\ell, n, m = 0, \ldots, q-1$, with ℓ labeling the total momentum of the interacting pair. The sum is over all momenta and indices. Momentum conservation means that the interactions respect the $\hat{T}_2 = T_2$ symmetry. However, according to Eq. (4.2), $\hat{T}_1$ places the additional constraint

$$g^{(\ell)}_{nm} = g^{(\ell+2)}_{n-1,m-1} \tag{4.5}$$

on the couplings [3]. With this, the normal state is invariant under the MTG and the global $U(1)$ transformation associated with charge conservation. As we will see in Sec. 4.3, the fact that the MTG contains $U(1)$ transformations implies that paired states that break the $U(1)$ symmetry necessarily break the MTG down to a smaller subgroup.

[3] There are additional constraints from Hermiticity: $g^{(\ell)}_{nm}(\mathbf{p};\mathbf{k}) = g^{(\ell)*}_{mn}(\mathbf{k};\mathbf{p})$. Moreover, anti-commutation relations imply that we can further take $g^{(\ell)}_{nm}(\mathbf{p};\mathbf{k}) = -g^{(\ell)}_{-\ell-n,m}(-\mathbf{p};\mathbf{k}) = -g^{(\ell)}_{n,-\ell-m}(\mathbf{p};-\mathbf{k}) = g^{(\ell)}_{-\ell-n,-\ell-m}(-\mathbf{p};-\mathbf{k})$.

4.3 Symmetry Analysis of Pairing in Hofstadter Systems

We describe the state obtained by pairing of spin polarized electrons in a single Hofstadter band with the standard mean-field pairing Hamiltonian obtained using the Hubbard-Stratonovich transformation:

$$H = \sum_{\ell,\mathbf{p}} \varepsilon(\mathbf{p}) d^\dagger_{\mathbf{p},\ell} d_{\mathbf{p},\ell} + \frac{1}{2} \sum_{\ell,\ell',\mathbf{p}} \left[\hat{\Delta}_{\ell\ell'}(\mathbf{p}) d^\dagger_{\mathbf{p},\ell} d^\dagger_{-\mathbf{p},\ell'} + h.c. \right] + \\ + H_{\Delta^2} \tag{4.6}$$

where $\varepsilon(\mathbf{p})$ is the electron dispersion and $\hat{\Delta}(\mathbf{p})$ are gap functions that are $q \times q$ matrices.

Note that

$$H_{\Delta^2} = \sum_{\ell,n,m,\mathbf{p},\mathbf{p}'} \hat{\Delta}^\dagger_{\ell+m,-m}(\mathbf{p}) \left[g^{-1}(\mathbf{p};\mathbf{p}') \right]^{(\ell)}_{mn} \hat{\Delta}_{\ell+n,-n}(\mathbf{p}') \tag{4.7}$$

is a term quadratic in the gap function and involving the inverse of the coupling tensor:

$$\sum_{j\mathbf{q}} g^{(\ell)}_{mj}(\mathbf{p};\mathbf{q}) \left[g^{-1}(\mathbf{q};\mathbf{p}') \right]^{(\ell')}_{jn} = \delta_{\ell\ell'} \delta_{mn} \delta_{\mathbf{p}\mathbf{p}'} \tag{4.8}$$

We arranged the rest of the terms into the Bogoliubov-de Gennes (BdG) Hamiltonian:

$$H = \frac{1}{2} \sum_{\ell,\ell',\mathbf{p}} \Psi^\dagger_{\ell,\mathbf{p}} \left[\mathcal{H}_{BdG}(\mathbf{p}) \right]_{\ell\ell'} \Psi_{\ell',\mathbf{p}} + H_{\Delta^2} \tag{4.9}$$

where

$$\mathcal{H}_{BdG}(\mathbf{p}) = \begin{pmatrix} \varepsilon(\mathbf{p}) & \hat{\Delta}(\mathbf{p}) \\ \hat{\Delta}^\dagger(\mathbf{p}) & -\varepsilon(-\mathbf{p}) \end{pmatrix} \tag{4.10}$$

We have defined Nambu spinors $\Psi_{\mathbf{p},\ell} = (d_{\mathbf{p},\ell}, d^\dagger_{-\mathbf{p},\ell})$. The unphysical redundancy

of the BdG formalism is encoded in the anti-unitary particle hole symmetry (PHS) of the BdG Hamiltonian, which acts as $\mathcal{C} = \tau^x \mathcal{K}$ on the Nambu spinors where τ^j are Pauli matrices acting on the particle/hole sectors and $\mathcal{K}$ is complex conjugation. Under the PHS, $\mathcal{C}^{-1}\mathcal{H}_{BdG}(\mathbf{p})\mathcal{C} = -\mathcal{H}_{BdG}(-\mathbf{p})$, which implies that $\hat{\Delta}(\mathbf{p}) = -\hat{\Delta}^T(-\mathbf{p})$ consistent with anti-commutation relations.

In the mean field treatment, the gap function has to be solved for self-consistently by minimizing the free energy. The free energy is obtained from Eq. (4.6) by integrating out the $\Psi_{\ell,\mathbf{p}}$ fields from the partition function. The standard procedure using the Matsubara formalism yields

$$\mathcal{F} = -T \sum_{\omega,\mathbf{p}} \mathrm{Tr}\left[\log \beta \mathcal{G}^{-1}(i\omega, \mathbf{p})\right] + H_{\Delta^2} \tag{4.11}$$

where $\omega = (2\pi n + 1)T$ with integer n are the Matsubara frequencies and we defined the Gor'kov Green's function

$$\begin{aligned} \mathcal{G}(i\omega, \mathbf{p}) &= (i\omega - \mathcal{H}_{BdG}(\mathbf{p}))^{-1} = \\ &= \begin{pmatrix} \hat{G}(i\omega, \mathbf{p}) & \hat{F}(i\omega, \mathbf{p}) \\ \hat{F}^\dagger(i\omega, \mathbf{p}) & -\hat{G}^T(-i\omega, -\mathbf{p}) \end{pmatrix} \end{aligned} \tag{4.12}$$

Minimizing $\mathcal{F}$ with respect to $\hat{\Delta}^\dagger$ we obtain the gap equation

$$\hat{\Delta}_{\ell+n,-n}(\mathbf{p}) = T \sum_{\omega \mathbf{p}' m} g^{(\ell)}_{nm}(\mathbf{p}; \mathbf{p}') \hat{F}_{\ell+m,-m}(i\omega, \mathbf{p}') \tag{4.13}$$

Close below T_c we can expand the free energy and the Green's functions in powers of the gap function. In particular, to leading order

$$\hat{F}(i\omega, \mathbf{p}) = -\hat{G}^{(0)}(i\omega, \mathbf{p}) \hat{\Delta}(\mathbf{p}) \hat{G}^{(0)T}(-i\omega, -\mathbf{p}) \tag{4.14}$$

where $\hat{G}^{(0)}$ is the normal Green's function in the absence of pairing, i.e. when $\hat{\Delta} = 0$. While the equations above hold for the multi-band case as well, the linearized gap equation simplifies significantly in the single-band case as the normal state Green's function becomes

$$\hat{G}^{(0)} = \frac{\mathbb{1}}{i\omega - \varepsilon(\mathbf{p})} \tag{4.15}$$

which is proportional to the identity matrix. Carrying out the Matsubara sum in the usual weak coupling approximation yields the linearized gap equation:

$$\hat{\Delta}_{\ell+n,-n}(\mathbf{p}) = -\nu \log \frac{1.13\Lambda}{T} \sum_{\mathbf{p}'m} g^{(\ell)}_{nm}(\mathbf{p};\mathbf{p}')\hat{\Delta}_{\ell+m,-m}(\mathbf{p}') \tag{4.16}$$

where ν is the density of states at the Fermi level and Λ is the high energy cutoff.

In principle the parameters α, β_{MN} and $\kappa_{jj'}$ in Eq. (4.46) can be obtained from the microscopic free energy Eq. (4.11) by expanding the trace logarithm, plugging in the solutions of the gap equation Eq. (4.13) and summing over the momentum and patch indices (in order to obtain $\kappa_{jj'}$ we need to additionally allow $\hat{\Delta}$ to have spatial variations). Explicitly, assuming $\varepsilon(\mathbf{p})$ is approximately isotropic, in the single-band case we have

$$\begin{aligned} \alpha &= \sum H_{\Delta^2} - \nu \log \frac{1.13\Lambda}{T} \mathrm{Tr}\left[\hat{\Delta}^{(L)\dagger}\hat{\Delta}^{(L)}\right] \\ \beta_{MN} &= \frac{7\zeta(3)\nu}{32\pi^2 T^2} \sum \mathrm{Tr}\left[\hat{\Delta}^{(L+M)\dagger}\hat{\Delta}^{(L-M)}\hat{\Delta}^{(L+N)\dagger}\hat{\Delta}^{(L-N)}\right] \end{aligned} \tag{4.17}$$

Note that while only α explicitly depends on the interactions $g^{(\ell)}_{nm}$ via the H_{Δ^2} term, all terms depend on the interactions implicitly via $\hat{\Delta}^{(L)}$. All the parameters also depend on the band structure and temperature. In the multi-band case the traces include summations over the additional indices and the Green's functions can no longer be pulled out of the trace, resulting in more involved expressions.

The solutions of the linearized gap equation Eq.(4.16) can be classified by the

irreducible representations (irreps) of the symmetry groups of the system according to which they transform [193]. Our goal in what follows is therefore to determine the transformation properties of the gap functions under the MTG symmetries, and thus the irrep of the MTG the gap functions belong to. Although the irreps of the MTG formed by *single* electron Bloch states are well-known to be q dimensional [91–93], we show that the *paired* states transform according to different irreps depending on the parity of q [220]: a single irrep of dimension q for odd q, or four irreps of dimension $q/2$ for even q. As a result, symmetry dictates that the linearized gap equation falls apart into q or $q/2$ independent equations for odd and even q respectively, with solutions that have the same T_c [193]. Any linear combination of these independent solutions remains a solution of the linearized gap equation, but this degeneracy is lifted by non-linear terms in the full gap equation or, equivalently, by higher order terms in the free energy that we study in Sec. 4.4.

In order to address these questions, we first review the general symmetry action on the BdG Hamiltonian in Sec. 4.3.1. We will then utilize this formalism in Sec. 4.3.2 to address the role of MTG on the pairing Hamiltonian and construct the corresponding irreps furnished by the gap functions.

4.3.1 Symmetry Action on the Gap Function and the Linearized Gap Equation

We now review how symmetries other than the PHS act on the BdG Hamiltonian and in particular how they act on the gap functions $\hat{\Delta}$ [193, 202, 203]. First, recall a $U(1)$ symmetry $U(\theta)$ acts on the annihilation operators as $d_{\mathbf{p},\ell} \to e^{i\theta} d_{\mathbf{p},\ell}$. By requiring that the Hamiltonian in Eq. (4.10) is invariant under this transformation, we conclude that the gap function transforms as

$$\hat{\Delta}(\mathbf{p}) \xrightarrow{U(\theta)} e^{2i\theta} \hat{\Delta}(\mathbf{p}) \,, \tag{4.18}$$

which implies that the $U(1)$ symmetry is broken down to a $\mathbb{Z}_2$ symmetry in the SC state.

More generally, suppose that $S(\mathbf{p})$ is some (possibly momentum dependent) unitary matrix representing a symmetry acting on the normal state Hamiltonian. In the *normal state*, we then have a family of symmetries $S(\mathbf{p}, \theta_0) = U(\theta_0/2)S(\mathbf{p})$ parameterized by θ_0. Since the gap function breaks the $U(1)$ symmetry, at most one member of this family may remain unbroken, and so we have to consider each possibility in our analysis. By the same argument as for the $U(1)$ symmetry itself, we find that $S(\mathbf{p}, \theta_0)$ acts on the gap function as

$$\hat{\Delta}(\mathbf{p}) \xrightarrow{S(\theta_0)} e^{i\theta_0} S(\mathbf{p})\hat{\Delta}(\mathbf{p})S^T(-\mathbf{p})\,. \tag{4.19}$$

Requiring the gap function to be invariant under this symmetry, we note that the phase θ_0 is not arbitrary but instead determined by the possible solutions of

$$S(\mathbf{p})\hat{\Delta}(\mathbf{p})S^T(-\mathbf{p}) = e^{-i\theta_0}\hat{\Delta}(\mathbf{p})\,. \tag{4.20}$$

Typically there is only a finite set of allowed θ_0, which determine the irrep to which $\hat{\Delta}$ belongs. In particular, $e^{i\theta_0}$ determine the characters of the irrep [203], and for finite irreps there is only a finite set of characters. For example, if $S^q(\mathbf{p}) = 1$, we must have $\theta_0 = \frac{2\pi}{q}N$ with N being some integer. This is the case for the MTG symmetries: $\hat{T}_1^q = \hat{T}_2^q = 1$. Using Eqs. (4.2) and (4.19), we find that under $\hat{T}_1(\theta_1) = U(\theta_1/2)\hat{T}_1$ and $\hat{T}_2(\theta_2) = U(\theta_2/2)\hat{T}_2$ the gap function transforms as

$$\hat{\Delta} \xrightarrow{\hat{T}_1(\theta_1)} e^{i\theta_1}\hat{\tau}\hat{\Delta}\hat{\tau}^T\,, \tag{4.21a}$$

$$\hat{\Delta} \xrightarrow{\hat{T}_2(\theta_2)} e^{i\theta_2}\hat{\sigma}\hat{\Delta}\hat{\sigma}\,, \tag{4.21b}$$

where $\hat{\tau}$ and $\hat{\sigma}$ are the shift and clock matrices defined in Eq. (4.3). More explicitly,

the elements of $\hat{\Delta}$ transform as

$$\hat{\Delta}_{\ell\ell'} \xrightarrow{\hat{T}_1(\theta_1)} e^{i\theta_1}\hat{\Delta}_{\ell-1,\ell'-1} \tag{4.22a}$$

$$\hat{\Delta}_{\ell\ell'} \xrightarrow{\hat{T}_2(\theta_2)} e^{i\theta_2}\omega_q^{p(\ell+\ell')}\hat{\Delta}_{\ell\ell'}\,. \tag{4.22b}$$

As mentioned above, θ_1 and θ_2 in Eqs. (4.22a-4.22b) are restricted to the values:

$$\begin{aligned}\theta_1 &= -\frac{2\pi p}{q}M\,,\\ \theta_2 &= -\frac{2\pi p}{q}L\,,\end{aligned} \tag{4.23a}$$

where M, L are integers defined modulo q. In particular, note that $e^{i\theta_j}$ $(j = 1, 2)$ are actually elements of the MTG since $\hat{T}_2\hat{T}_1\hat{T}_2^{-1}\hat{T}_1^{-1} = U(-2\pi p/q)$, a $U(1)$ transformation acting as Eq. (4.88) on the gap function.

The first important conclusion is that there is no non-zero $\hat{\Delta}$ that satisfies both (4.22a) and (4.22b) for $q > 2$ ($q = 2$ is an exception, as we will discuss below), for any choice of θ_1 and θ_2. This means that any pairing order *necessarily* breaks at least some MTG symmetries. A similar result was shown for the superfluid bosonic condensate in a strong magnetic field, essentially the bosonic version of the Hofstadter model, in Ref. [55]. We note that the transformation properties of the bosonic fields considered in Ref. [55] under the MTG differ from Eqs. (4.22a-4.22b), i.e. they belong to a different irreducible representation (see Sec. 4.3.2 below). The essential reason for the symmetry breaking is however the same: in both cases, either the superfluid or superconducting condensates break the $U(1)$ symmetry, and since the MTG contains a subgroup of $U(1)$, it too must be broken. The fact that the MTG contains a subgroup of $U(1)$, in turn, is a consequence of the non-trivial commutation relations of the magnetic translations.

Before moving on to the analysis of the irreps realized by the gap function in

the next subsection, let us consider the implications of the MTG symmetries for the linearized gap equation Eq. (4.16). The first observation is that only gap function elements $\hat{\Delta}_{\ell+\ell'}$ with the same value of $L = \ell + \ell'$ appear on both sides of the equation, and, as a result, the linearized gap equation splits into q independent equations for each value of L, which corresponds to the L^{th} anti-diagonal of the matrix $\hat{\Delta}$ and labels the total momentum of the Cooper pairs along the $\hat{\mathbf{b}}_2$ direction. This decoupling is a consequence of momentum conservation along that direction due to the $\hat{T}_2 = T_2$ symmetry. As such, for a particular L, the decoupled solution is a matrix with non-zero elements only along the L^{th} anti-diagonal:

$$\hat{\Delta}^{(L)} = \begin{pmatrix} & & & \hat{\Delta}_{0,L} & & & \\ & & \hat{\Delta}_{1,L-1} & & & & \\ & \iddots & & & & & \\ \hat{\Delta}_{L,0} & & & & & & \\ & & & & & \hat{\Delta}_{L+1,q} & \\ & & & & \iddots & & \\ & & & \hat{\Delta}_{q,L+1} & & & \end{pmatrix} \tag{4.24}$$

We refer to such a matrix as an L^{th} anti-diagonal matrix. From Eq. (4.22b),

$$\hat{\Delta}^{(L)} \xrightarrow{\hat{T}_2(\theta_2)} e^{i\theta_2}\omega_q^{pL}\hat{\Delta}^{(L)} \tag{4.25}$$

thus enforcing the condition $e^{i\theta_2} = \omega_q^{-pL}$, which identifies the L index in Eq. (4.23a) with the momentum of the Cooper pair. As such, $\hat{\Delta}^{(L)}$ are precisely the gap functions symmetric under $\hat{T}_2(\theta_2)$ symmetry with $\theta_2 = -\frac{2\pi p}{q}L$. Conversely, $\hat{\Delta}^{(L)}$ break $\hat{T}_2(\theta_2)$ for any other value of θ_2 and they also break $\hat{T}_1(\theta_1)$ for any value of θ_1 (with the exception of the case $q = 2$ discussed below).

We will consider gap functions symmetric under $\hat{T}_1(\theta_1)$ symmetries in Sec. 4.4

when we study the effect of non-linear terms in the gap equation, but for the purposes of the linearized gap equation it is sufficient to look at $\hat{\Delta}^{(L)}$. The effect of the $\hat{T}_1$ symmetry on $\hat{\Delta}^{(L)}$ is to shift it to $\hat{\Delta}^{(L-2)}$. More precisely, we *define* $\hat{\Delta}^{(L)}$ such that

$$\hat{\Delta}^{(L)} \xrightarrow{\hat{T}_1(0)} \hat{\Delta}^{(L-2)} \tag{4.26a}$$

$$\hat{\Delta}^{(L)} \xrightarrow{\hat{T}_2(0)} \omega_q^{pL} \hat{\Delta}^{(L)} \,. \tag{4.26b}$$

Eqs. (4.22a,4.26a) in particular imply that $\hat{\Delta}^{(L)}_{\ell\ell'} = \hat{\Delta}^{(L-2)}_{\ell-1,\ell'-1}$.

At this stage, it becomes necessary to distinguish between the cases of even and odd q. In the latter case, note that applying $\hat{T}_1$ to $\hat{\Delta}^{(0)}$ generates all of $\hat{\Delta}^{(L)}$ since $L+1 \equiv L + 2\frac{q+1}{2} \bmod q$; the parity of L, in other words, is not well-defined [4]. For odd q, we therefore define

$$\Delta_\ell \equiv \hat{\Delta}^{(L)}_{\left[\frac{L+\ell}{2}\right]_q, \left[\frac{L-\ell}{2}\right]_q} \tag{4.27}$$

that are independent of L. Here $[\ell/2]_q = \ell/2$ if ℓ is even but $[\ell/2]_q = (\ell+q)/2$ if ℓ is odd. As a concrete example, for $q = 3$ there is a single irrep with three irrep components $\hat{\Delta}^{(L)}$ given by

$$\hat{\Delta}^{(0)} = \begin{pmatrix} \Delta_0 & 0 & 0 \\ 0 & 0 & \Delta_2 \\ 0 & \Delta_1 & 0 \end{pmatrix}, \hat{\Delta}^{(1)} = \begin{pmatrix} 0 & 0 & \Delta_1 \\ 0 & \Delta_0 & 0 \\ \Delta_2 & 0 & 0 \end{pmatrix}, \hat{\Delta}^{(2)} = \begin{pmatrix} 0 & \Delta_2 & 0 \\ \Delta_1 & 0 & 0 \\ 0 & 0 & \Delta_0 \end{pmatrix}. \tag{4.28}$$

For even q, however, $\hat{\Delta}^{(L)}$ are not all generated by applying $\hat{T}_1$ to $\hat{\Delta}^{(0)}$; rather, $\hat{\Delta}^{(L)}$ split into two groups for even and odd L,

$$\begin{aligned} \hat{\Delta}^{(0)} &\xrightarrow{\hat{T}_1(0)} \hat{\Delta}^{(q-2)} \xrightarrow{\hat{T}_1(0)} \hat{\Delta}^{(q-4)} \xrightarrow{\hat{T}_1(0)} \ldots \\ \hat{\Delta}^{(1)} &\xrightarrow{\hat{T}_1(0)} \hat{\Delta}^{(q-1)} \xrightarrow{\hat{T}_1(0)} \hat{\Delta}^{(q-3)} \xrightarrow{\hat{T}_1(0)} \ldots \end{aligned} \tag{4.29}$$

[4] For example, for $q = 3$, the $L = 0, 1, 2$ values, under the action of T_1, are cycled as $0 \to 2 \to 1 \to 0 \to \ldots$; for $q = 5$, $0 \to 2 \to 4 \to 1 \to 3 \to 0 \to \ldots$, *etc.*

that are not mapped to each other by $\hat{T}_1$ or any other MTG symmetry (in Sec.4.3.2 we show that each of these two groups actually splits into two more, resulting in 4 irreps for even q). For even q we therefore define

$$\Delta_\ell \equiv \hat{\Delta}^{(L)}_{\frac{L+\ell}{2},\frac{L-\ell}{2}} \tag{4.30}$$

but with ℓ defined modulo $2q$ and restricted to be of the same parity as L, i.e. $\ell = 0, 2, \ldots, 2(q-1)$ for even L and $\ell = 1, 3, \ldots, 2q-1$ for odd L. With the indices $\frac{L\pm\ell}{2}$ defined modulo q this can be seen to properly index all the elements of $\hat{\Delta}^{(L)}$. As another concrete example, for $q = 2$ we have

$$\hat{\Delta}^{(0)} = \begin{pmatrix} \Delta_0 & 0 \\ 0 & \Delta_2 \end{pmatrix} \tag{4.31}$$

and

$$\hat{\Delta}^{(1)} = \begin{pmatrix} 0 & \Delta_3 \\ \Delta_1 & 0 \end{pmatrix} \tag{4.32}$$

In terms of the functions Δ_ℓ, the linearized gap equation for each value of L becomes

$$\Delta_\ell(\mathbf{p}) = -\nu \log \frac{1.13\Lambda}{T} \sum_{\mathbf{p}'\ell'} g^{(L)}_{\left[\frac{\ell-L}{2}\right]_q,\left[\frac{\ell'-L}{2}\right]_q}(\mathbf{p};\mathbf{p}')\Delta_{\ell'}(\mathbf{p}') \tag{4.33}$$

Because the interactions satisfy Eq. (4.5) due to the $\hat{T}_1$ symmetry, for odd q we can take $g^{(L)}_{[(\ell-L)/2]_q,[(\ell'-L)/2]_q} = g^{(0)}_{[\ell/2]_q,[\ell'/2]_q}$. Recall that $[\ell/2]_q = \ell/2$ if ℓ is even but $[\ell/2]_q = (\ell+q)/2$ if ℓ is odd; note that for even L, ℓ is also even. For even q and even L we can take $g^{(L)}_{(\ell-L)/2,(\ell'-L)/2} = g^{(0)}_{\ell/2,\ell'/2}$; for odd L, we instead take $g^{(L)}_{(\ell-L)/2,(\ell'-L)/2} = g^{(1)}_{(\ell-1)/2,(\ell'-1)/2}$. Recall that for even q, ℓ and ℓ' are both defined modulo $2q$ and restricted to have the same parity as L.

The second important conclusion that follows from these considerations of $\hat{T}_1$ symmetry is that, for odd q, each of the L equations Eq. (4.33) that the linearized gap

equation Eq. (4.16) decouples into are the *same* equation; for even q, the equations are the same for a given parity of L but may be different for even and odd L. This means in particular that the T_c determined by these equations is also the same, and moreover any linear combination

$$\hat{\Delta} = \sum_L \eta_L \hat{\Delta}^{(L)} \tag{4.34}$$

with some complex coefficients η_L is another solution of the linearized gap equation. As we will see in Sec. 4.4, this includes gap functions symmetric under $\hat{T}_1(\theta_1)$ and indeed any other element of the MTG symmetries. This large degeneracy of solutions of the linearized gap equation is lifted when non-linear terms are included, as we also show in Sec. 4.4. The higher order terms thus determine which MTG symmetries, if any, remain unbroken in the ground state.

4.3.2 Gap Functions as Irreducible Representations of the Magnetic Translation Group

The symmetry analysis of the previous section shows that pairing matrix $\hat{\Delta}$ belongs to a multidimensional irrep, with $\hat{\Delta}^{(L)}$ forming the components of the irrep, as described in Eq. (4.34). The dimension of the irrep, i.e. the number of its components, is thus q for odd q and $q/2$ for even q. The fact that the linearized gap equation Eq. (4.16) decouples into q equations, all or half of which are degenerate (i.e. have the same T_c) for odd and even q respectively, is a general consequence of this fact. The existence of non-trivial irreps implies that $\hat{\Delta}$ must break at least part of the MTG symmetries, as only gap functions belonging to a trivial irrep, which is one dimensional, respect all the symmetries. While the analysis of irreps of the MTG acting on single particle Bloch states is well-known [91–93], a comprehensive study of these irreps in the context of charge 2e condensates is lacking. The goal of this section is therefore to classify

pairing functions that furnish the irreps of the MTG. In the course of this analysis, we will encounter an interesting dependence on dimension of the irreps as a function of parity of q, which fundamentally contrasts with the well-known irreps furnished by one particle states.

A representation is a group homomorphism $\Gamma : G \to GL(V)$ between the symmetry group G – the MTG in our case – and the group of linear transformations $GL(V)$ that act on a particular vector space V. For irreps realized by $\hat{\Delta}$, $\hat{\Delta}^{(L)}$ form the basis of this vector space. The linear transformations in question, $\Gamma(S)$ for an element S of the MTG, act on the gap function via Eq. (4.19). The representation is reducible if there is a non-trivial subspace of V that is mapped to itself under the action of any symmetry operation. To clarify the terminology, we say that $\hat{\Delta}$ belongs to, realizes, or transforms as the irrep, and that $\hat{\Delta}^{(L)}$ are the components of the irreps. The homomorphism is always understood to be the one determined by Eq. (4.19). For the components $\hat{\Delta}^{(L)}$ of the irrep, the transformations are explicitly given by Eqs. (4.26a) and (4.26b).

In order to explicitly construct an irrep, the general procedure [93] is to start with some fixed gap function $\hat{\Delta}^{(0)}$ symmetric under a particular symmetry, $\hat{T}_2(0)$ in our case, and then apply all other symmetries to obtain the vector space and the rest of the irrep components $\hat{\Delta}^{(L)}$. In our case it was sufficient to apply $\hat{T}_1(0)$, and we thus proved in Sec. 4.3.1 that the representation realized by $\hat{\Delta}^{(L)}$ with $L = 0, 1, \ldots, q-1$ and satisfying the defining relations Eqs. (4.26a-4.26b) is irreducible of dimension q for odd q. However, in the even q case, the representation reduces to irreps of dimension $q/2$ with a basis still given by $\hat{\Delta}^{(L)}$, but with L restricted to be even or odd. In what follows, we provide additional information to fully specify the irreps for even q.

Before discussing the irreps for even q in more detail, let us note that the fact that they are $q/2$ dimensional irreps is in contrast with the earlier result found by Brown

and Zak in Refs. [91–93]. The reason for this difference is that the MTG contains a subgroup of the $U(1)$ gauge symmetry that gives rise to charge conservation; therefore, in order to specify the irrep of the MTG, it is necessary to specify the irrep of the $U(1)$ subgroup, which is equivalent to specifying the charge of the particle modulo q. In Refs. [91–93], the authors were interested in Bloch states, i.e. single particle states with elementary charge. They therefore required that the MTG element

$$\hat{L} = \hat{T}_2\hat{T}_1\hat{T}_2^{-1}\hat{T}_1^{-1} = U(-2\pi p/q) \tag{4.35}$$

is represented by $\Gamma(U(-2\pi p/q)) = e^{\frac{2\pi i p}{q}}$. This is simply the Aharonov-Bohm phase picked up by an electron moving around a loop encircling the original, non-magnetic, unit cell described by the operation $\hat{L}$. Applying $\hat{L}$ on the gap function via Eq. (4.19), however, yields a different result, since from Eq. (4.88) we have

$$\hat{\Delta}^{(L)} \xrightarrow{\hat{T}_2\hat{T}_1\hat{T}_2^{-1}\hat{T}_1^{-1}} e^{-2\frac{2\pi p}{q}i}\hat{\Delta}^{(L)}\,, \tag{4.36}$$

consistent also with Eqs. (4.22a-4.22b), and corresponding to an Aharonov-Bohm phase picked up by a particle of charge $2e$. This is of course as one would expect for a Cooper pair.

Although Refs. [91–93] rejected irreps with $\Gamma(U(\theta)) = e^{iQ\theta}$ with $Q \neq 1$ as unphysical, here we find that they naturally correspond to irreps realized by condensates of charge Q. Indeed, there always exists the trivial irrep under which the MTG elements are mapped to the identity, and it corresponds to $Q = 0$. This general observation has been made earlier in Ref. [220] in the context of states of pairs of electrons, though it did not explicitly discuss superconductivity. The main conclusion is that the irreps realized by the gap functions $\hat{\Delta}$ cannot be classified by the same irreps as considered in Refs. [91–93] in the context of single particle states. This is also the main difference between the fermionic Hofstadter SC problem and the bosonic

Hofstadter superfluid considered in Refs. [55, 221–224].

We also note that Eq. (4.36) implies that the phase of $\hat{\Delta}^{(L)}$ winds as one goes around the non-magnetic unit cell, indicating that the Hofstadter SC phase is a vortex lattice. Thus, our irrep analysis provides a general framework that justifies the numerical observation of vortex lattices in fermionic [64, 67] and bosonic [55] Hofstadter systems. Unlike regular Abrikosov vortices, however, note that $\hat{\Delta}^{(L)}$ need not vanish anywhere in space. A similar phenomenon occurs in Josephson vortices that also have a non-vanishing gap in their cores [136]. In the limit $q \to \infty$, we expect the vortex lattice to approach the Abrikosov vortex lattice at the upper critical field H_{c2}.

Irreps for Even q

Although the MTG irreps realized by $\hat{\Delta}^{(L)}$ are distinct from the single particle irreps of the MTG, for odd q they are qualitatively similar as they are of the same dimension. For even q, on the other hand, we saw that the parity of L is well defined, and $\hat{\Delta}^{(L)}$ split into two $q/2$ dimensional irreps for each parity of L, as in Eq. (4.29). The irreps for even q are thus qualitatively different. As we will now show, there are in fact four such irreps. One can anticipate that there must be four $q/2$ irreps from a version of Schur's orthogonality relations proven in Refs. [93, 220] that state that the sum of the squares of the dimensions of all distinct irreps for a fixed value of the $U(1)$ charge must equal the order of the MTG, i.e. the number of its elements, that is q^2. There is thus only one irrep for odd q, but there must be four $q/2$-dimensional irreps for even q, as shown also in Ref. [220].

The reason there are additional irreps is that there is an additional symmetry that may remain unbroken by the paired state. To see this, note that applying $\hat{T}_1(\theta_1)$ $q/2$ times on $\hat{\Delta}$ brings an element on the L^{th} anti-diagonal to the same anti-diagonal but

not to the same diagonal, as can be seen from Eq. (4.22a):

$$\hat{\Delta}_{\ell\ell'} \xrightarrow{\hat{T}_1^{q/2}(\theta_1)} e^{i\theta_1 q/2}\hat{\Delta}_{\ell-q/2,\ell'-q/2}\,. \tag{4.37}$$

The element on the RHS is on the same anti-diagonal since $\ell - q/2 + \ell' - q/2 \equiv \ell + \ell'$ mod q, but it is not the same element since $q/2 \neq 0$ mod q. Note that $e^{i\theta_1 q/2} = (-1)^{pM} = (-1)^M$ (using the fact that p cannot be even if q is even), consistent with the fact that $\hat{T}_1^{q/2}$ squares to the identity. The parity of M provides the additional character, in addition to the parity of L, that yields the four $q/2$-dimensional irreps as claimed.

We label the irrep components $\hat{\Delta}^{(L,\pm)}$, and these satisfy

$$\hat{\Delta}^{(L,\pm)}_{\ell-q/2,\ell'-q/2} = \pm\hat{\Delta}^{(L,\pm)}_{\ell\ell'}\,. \tag{4.38}$$

This implies that the functions Δ_ℓ in Eq. (4.30) additionally satisfy $\Delta_{\ell+q} = \pm\Delta_\ell$ (recall that ℓ in this case is defined modulo $2q$). In addition to having only a single anti-diagonal, $\hat{\Delta}^{(L,\pm)}$ has a $\frac{q}{2} \times \frac{q}{2}$ block structure:

$$\hat{\Delta}^{(L,\pm)} = \begin{pmatrix} \hat{A} & \hat{B} \\ \pm\hat{B} & \pm\hat{A} \end{pmatrix} \tag{4.39}$$

where $\hat{A}$ and $\hat{B}$ are $\frac{q}{2} \times \frac{q}{2}$ matrices. Notice that $\hat{\Delta}^{(L,+)\dagger}\hat{\Delta}^{(L,-)}$ is odd under $\hat{T}_1^{q/2}$ and so such terms are not allowed in the free energy (also their trace vanishes), as expected for products of elements from different irreps. This implies in particular that $\hat{\Delta}^{(L,+)}$ and $\hat{\Delta}^{(L,-)}$ decouple in the linearized gap equation and in general have different critical temperatures.

To illustrate the irreps and the additional symmetry, it is helpful to consider again the special case of $q = 2$. The relation Eq. (4.38) places an additional constraint on

the gap functions in Eqs. (4.31-4.32), so the components of the two irreps symmetric under $\hat{T}_2(0)$ are

$$\hat{\Delta}^{(0,\pm)} = \begin{pmatrix} \Delta_0 & 0 \\ 0 & \pm\Delta_0 \end{pmatrix}, \tag{4.40}$$

while the components of the two irreps anti-symmetric under $\hat{T}_2(0)$ (symmetric under $\hat{T}_2(\pi)$) are

$$\hat{\Delta}^{(1,\pm)} = \begin{pmatrix} 0 & \pm\Delta_1 \\ \Delta_1 & 0 \end{pmatrix}. \tag{4.41}$$

The $\pm$ corresponds to gaps symmetric or anti-symmetric under $\hat{T}_1(0)$ respectively.

A more generic example is provided by $q = 4$, for which the irrep components are given by

$$\hat{\Delta}^{(0,\pm)} = \begin{pmatrix} \Delta_0 & 0 & 0 & 0 \\ 0 & 0 & 0 & \Delta_2 \\ 0 & 0 & \pm\Delta_0 & 0 \\ 0 & \pm\Delta_2 & 0 & 0 \end{pmatrix}, \hat{\Delta}^{(2,\pm)} = \begin{pmatrix} 0 & 0 & \pm\Delta_2 & 0 \\ 0 & \Delta_0 & 0 & 0 \\ \Delta_2 & 0 & 0 & 0 \\ 0 & 0 & 0 & \pm\Delta_0 \end{pmatrix},$$
$$\hat{\Delta}^{(1,\pm)} = \begin{pmatrix} 0 & \Delta_3 & 0 & 0 \\ \Delta_1 & 0 & 0 & 0 \\ 0 & 0 & 0 & \pm\Delta_3 \\ 0 & 0 & \pm\Delta_1 & 0 \end{pmatrix}, \hat{\Delta}^{(3,\pm)} = \begin{pmatrix} 0 & 0 & 0 & \pm\Delta_1 \\ 0 & 0 & \Delta_3 & 0 \\ 0 & \Delta_1 & 0 & 0 \\ \pm\Delta_3 & 0 & 0 & 0 \end{pmatrix}, \tag{4.42}$$

which correspond to states symmetric under $\hat{T}_2(\theta_2)$ with $\theta_2 = \frac{\pi p}{2} L$ and symmetric/anti-symmetric under $\hat{T}_1^2(0)$ for $\pm$ respectively (p can only be 1 or 3 in this case). Note the block structure that is in agreement with Eq. (4.39) that also holds for the $q = 2$ case.

We stress that the irrep construction presented here for both even and odd q can be applied without change if $\hat{\Delta}$ carries additional indices (e.g. spin or band indices),

as long as the MTG symmetries do not act on these indices. The construction is therefore quite general. It is however not unique since the irrep is multi-dimensional: instead of irrep components symmetric with respect to $\hat{T}_2$, we could have worked with irrep components that are symmetric with respect to $\hat{T}_1$, or, in general, any q linearly independent combinations of $\hat{\Delta}^{(L)}$. We will consider such combinations in Sec. 4.4 when studying the minima of the Ginzburg-Landau free energy.

4.4 Effective Ginzburg-Landau Theory

As discussed in Sec. 4.3, the gap functions that solve the linearized gap equation are arbitrary linear combinations of the irrep components

$$\hat{\Delta}(\mathbf{p}) = \sum_L \eta_L \hat{\Delta}^{(L)}(\mathbf{p})\,. \tag{4.43}$$

The irreps are q dimensional for odd q, with $L = 0, \ldots, q-1$ and $\hat{\Delta}^{(L)}$ satisfying the defining properties given in Eq. (4.26a-4.26b). For even q, we assume that one of the four $q/2$-dimensional irreps has the highest T_c so that the rest can be neglected, and we therefore drop the $\pm$ in $\hat{\Delta}^{(L,\pm)}$ and restrict L to be even or odd.

The degeneracy of the linearized gap equation is, however, lifted by even infinitesimal non-linear terms, resulting in spontaneous symmetry breaking of the MTG symmetries. In order to study this symmetry breaking, here we use the irreps to construct a phenomenological effective Ginzburg-Landau free energy, following the same procedure used for unconventional superconductors [193]. In the GL theory, we ignore the microscopic details, encoded in the functional form of $\hat{\Delta}^{(L)}(\mathbf{p})$ determined ultimately by the interactions through the gap equation, and write the most general form of the free energy for the complex fields η_L constrained by the $U(1)$ and MTG symmetries.

The vector of complex numbers

$$\boldsymbol{\eta} = (\eta_0, \ldots, \eta_{q-1}) \tag{4.44}$$

constitutes the order parameter of the paired state (for even q, we take $\boldsymbol{\eta}$ to be a $q/2$ component vector instead but use the same notation below). We emphasize that while we originally obtained the microscopic gap functions $\hat{\Delta}^{(L)}$ in the context of a weak-coupling pairing within a single Hofstadter band, the effective GL theory presented here is insensitive to the details of the microscopic theory and therefore remains valid both in the presence of additional degrees of freedom (including additional Hofstadter bands) and in the the strong-coupling limit.

Note that the action of $\hat{T}_1$ and $\hat{T}_2$ on $\Delta^{(L)}$ as given in Eq. (4.26a-4.26b) is equivalent to an action on the components of $\boldsymbol{\eta}$:

$$\eta_L \xrightarrow{\hat{T}_1(0)} \eta_{L+2}\,, \tag{4.45a}$$

$$\eta_L \xrightarrow{\hat{T}_2(0)} \omega_q^{-pL}\eta_L\,, \tag{4.45b}$$

$$\eta_L \xrightarrow{U(\theta)} e^{-2i\theta}\eta_L\,. \tag{4.45c}$$

We can see that $\hat{T}_1$ and $\hat{T}_2$ act on it as $\hat{\tau}^2$ and $\hat{\sigma}^*$ respectively, while $U(1)$ transformations $U(\theta)$ act as $e^{-2i\theta}$. This determines the irrep of the MTG realized by $\boldsymbol{\eta}$ itself in place of the set of $\hat{\Delta}^{(L)}$ [5].

Using these transformation properties, we determine the most general form of the GL free energy to fourth order in $\boldsymbol{\eta}$, consistent with MTG and U(1) symmetries:

$$\mathcal{F} = \alpha\,|\boldsymbol{\eta}|^2 + \sum_{MN}\beta_{MN}\sum_{L}\eta^*_{L+M}\eta^*_{L-M}\eta_{L+N}\eta_{L-N} + \sum_{jj'}\kappa_{jj'}\left(\tilde{D}_j\boldsymbol{\eta}\right)^*\cdot\left(\tilde{D}_{j'}\boldsymbol{\eta}\right)\,. \tag{4.46}$$

[5] Eq. (4.45a) needs to be modified to $\eta_L \xrightarrow{\hat{T}_1(2\pi p/q)} \eta_{L+2}$ for $\hat{\Delta}^{(L,-)}$ irrep components for even q since $\hat{T}_1^{q/2}(0)$ acts as -1 on that irrep.

Note that terms of the form $\eta_L^* \eta_{L'}$ are ruled out for $L' \neq L$ by $\hat{T}_2$ symmetry (including gradient terms), while $\hat{T}_1$ implies that $|\eta_L|^2$ terms have equal coefficients and that β_{MN} does not depend on L. $\tilde{D}_j = \partial_j + \frac{2ie}{c}\tilde{A}_j$ (with $j = x, y$) is the covariant derivative where $\tilde{\mathbf{A}} = \mathbf{A} - xB\mathbf{a}_2/a_{2y}$ is the gauge field associated with the spatial variations of the overall phase of $\boldsymbol{\eta}$. This choice imposes gauge invariance while ensuring that in the ground state η_L are spatially uniform. We emphasize that the relation between the spatial variations of the overall phase of $\boldsymbol{\eta}$ and the vector potential is only valid for very small spacial variations of η_L, i.e. on a scale much larger than the magnetic unit cell, as the transformation properties of the gap functions $\hat{\Delta}$ under gauge transformations, inherited from those of the $d_{\mathbf{p},\ell}$ operators, are highly non-trivial within the magnetic unit cell. A free energy with very similar symmetries was constructed as a dual theory in a different context in Ref. [221]; a similar energy density was also obtained in the context of the bosonic Hofstadter model in Refs. [55, 222]. As discussed in Sec. 4.3.2, the difference from our work is that the order parameter considered in those works belonged to a charge $1e$ irrep of the MTG, rather than $2e$ irreps.

We note that there is some redundancy in the parameters, and in particular we take $\beta_{MN} = \beta_{M,-N} = \beta_{-MN} = \beta_{NM}^*$ (the last equality to make the free energy real; the rest are not strictly necessary but account for redundancy) and $\kappa_{jj'} = \kappa_{j'j}^*$. For odd q only $\frac{(q+1)(q+3)}{4}$ of the β_{MN} parameters are thus distinct, a total of $\frac{(q+1)^2}{4}$ parameters counting real and imaginary parts separately. For even q, M and N must be both even or both odd with only even or only odd L, depending on the irrep. The number of independent parameters, again counting the real and imaginary parts separately, is $\frac{(q+2)^2}{8}$ if $q/2 \neq 1$ is odd, with the exception of $q = 2$, for which there is an additional identification between β_{00} and β_{11}. If $q/2$ is even we additionally have that $\beta_{00} = \beta_{q/2,q/2}$ and $\beta_{0,q/2} = \beta_{q/2,0}$ and are therefore real, so the number of independent real parameters is $\frac{q^2-q-6}{2}$. Terms with M and N of different parity are allowed and couple the even and odd irreps, but this can be ignored if the critical

temperatures for the two irreps are sufficiently different at second order.

In addition, we observe that the free energy Eq. (4.46) has an accidental symmetry at fourth order. Namely, it is symmetric under $\mathcal{I} : \eta_L \to \eta_{-L}$ (and combinations of $\mathcal{I}$ with MTG symmetries). This accidental symmetry is broken by sixth order terms, however:

$$\mathcal{F}^{(6)} = \sum_{MM'NN'} \gamma_{MM'NN'} \sum_{L} \eta^*_{L+M}\eta^*_{L+M'}\eta^*_{L-M-M'}\eta_{L+N}\eta_{L+N'}\eta_{L-N-N'} \,. \tag{4.47}$$

We will not consider these higher order terms below but note that the accidental symmetry is in general explicitly broken. $\mathcal{I}$ may be an actual symmetry if crystalline symmetries are present, for example a rotation by π as considered in Refs. [55, 221, 222].

Minimizing the free energy Eq. (4.46) with respect to η^*_L (and integrating by parts), we obtain the Ginzburg-Landau equations:

$$\kappa_{jj'}\tilde{D}_j\tilde{D}_{j'}\eta_L = \alpha\eta_L + 2\sum_{MN}\beta_{MN}\eta^*_{L+2M}\eta_{L+M+N}\eta_{L+M-N} \tag{4.48}$$

Below we will only discuss the uniform phases, in which the left hand side vanishes, and leave the non-uniform solutions for a future study. As already noted in Sec. 4.3.2, there is no non-zero gap function $\hat{\Delta}$, and hence no non-zero configuration of the field $\boldsymbol{\eta}$, that respects all the MTG symmetry. The non-trivial solutions of the GL equations therefore necessarily break some but not necessarily all of the MTG symmetries, as we will show below. Note that the solutions correspond to local extrema of the free energy, while the ground state is determined by the global minimum.

With our choice of irrep elements, the simplest type of symmetric solutions are the ones that respect the $\hat{T}_2(\theta_2)$ symmetry with $\theta_2 = \frac{2\pi p}{q}L$ (breaking it for any other choice of θ_2), in which case $\eta_{L'} = 0$ unless $L' = L$, and the only non-zero components is $\eta_L = \sqrt{\frac{-\alpha}{2\beta_{00}}}$. There are q or $q/2$ solutions corresponding to each choice of L (for q

odd and even respectively). The value of the free energy at these extrema is

$$\mathcal{F}_{0,1} = -\frac{\alpha^2}{4\beta_{00}} \tag{4.49}$$

(the indexing will be explained below). The $\hat{T}_1(\theta_1)$ symmetry is broken for any choice of θ_1 and maps the degenerate extrema to each other. If this solution is a global minimum, we refer to the corresponding ground state as a $\mathbb{Z}_q$ symmetric Hofstadter SC phase. The order of the symmetry is q for either even or odd q.

There is no fundamental difference between the $\hat{T}_2(\theta_2)$ and $\hat{T}_1(\theta_1)$ symmetries of course, and so we naturally expect solutions of the GL equation that respect $\hat{T}_1(\theta_1)$ as well as other symmetries of the MTG while breaking $\hat{T}_2(\theta_2)$ for any choice of θ_2. Indeed, since the irreps are multidimensional, the definition of the irrep components $\hat{\Delta}^{(L)}$ is not unique, and we could always take the basis of the irrep to be any linearly independent orthogonal combinations of $\hat{\Delta}^{(L)}$, including those that respect other MTG symmetries. In particular, there are solutions that respect the symmetry $\hat{T}(\theta_0) = \hat{T}_2^{N_2}(\theta_2)\hat{T}_1^{N_1}(\theta_1)$ for any choice of $\theta_0 = N_1\theta_1 + N_2\theta_2$ with $N_1, N_2 = 0, \ldots, q-1$. We index the corresponding solutions as $\boldsymbol{\eta}^{(M)_{N_1,N_2}}$. For $N_1 \neq 0$, $\hat{T}_2(\theta_2)$ is broken and generates degenerate solutions by shifting the index $M = 0, \ldots, q-1$. The solutions found above that do respect $\hat{T}_2(\theta_2)$ can be considered as a special case with $N_1 = 0$, $N_2 = 1$, and can be labeled $\boldsymbol{\eta}^{(L)_{0,1}}$ (we reserve L to label the $\hat{\mathbf{b}}_2$ component of the total momentum of the Cooper pairs).

Before explicitly constructing such linear combinations and showing that they do indeed yield additional solutions of the GL equations in Sec. 4.4.2, we illustrate this fact for the cases of $q \leq 4$ that can be partially analyzed analytically. Some of these cases have earlier been considered in Refs. [64, 67], and similar free energies with some additional symmetries were also analyzed in Ref. [221] in a different context. In contrast to those earlier works, here we explicitly determine the symmetries of

the ground states, and identify additional possible symmetric phases that were not previously considered.

4.4.1 Solutions of Ginzburg-Landau Equations for $q \leq 4$

We start with the simplest non-trivial case, $q = 2$ (only $p = 1$ is allowed), which has four 1D irreps. The free energy of each irrep is trivial and of the form (omitting gradient terms)

$$\mathcal{F} = \alpha|\eta|^2 + \beta|\eta|^4 \tag{4.50}$$

for the single order parameter $\eta = \eta_0$ or η_1 and a unique solution for $|\eta|$, implying that the ground state always has some $\mathbb{Z}_2$ symmetry. The corresponding gap functions $\hat{\Delta}^{(L,\pm)}$ with $L = 0, 1$ are simply the irrep components given in Eqs. (4.40-4.41):

$$\hat{\Delta}^{(0,\pm)} = \begin{pmatrix} \Delta_0 & 0 \\ 0 & \pm\Delta_0 \end{pmatrix} \tag{4.51}$$

and

$$\hat{\Delta}^{(1,\pm)} = \begin{pmatrix} 0 & \pm\Delta_1 \\ \Delta_1 & 0 \end{pmatrix} \tag{4.52}$$

with Δ_ℓ as defined in Eq. (4.30). This is the only case in which the MTG may be unbroken, in particular it is unbroken by $\hat{\Delta}^{(0,+)}$. Note that $L = 0, 1$ corresponds to gap functions symmetric/anti-symmetric under $\hat{T}_2(0)$, while $\pm$ corresponds to gap functions symmetric/anti-symmetric under $\hat{T}_1(0)$. As these are all the symmetries of the MTG, in this case there are no other symmetric linear combinations.

$q = 4$

The second-simplest non-trivial case and the only other case that can be completely solved analytically is $q = 4$ (with $p = 1$ or 3), in which case there are four 2D irreps

corresponding to even or odd L and gaps symmetric or anti-symmetric under $\hat{T}_2^2(0)$. The free energy is

$$\begin{aligned}\mathcal{F}_+ &= \alpha_0(|\eta_0|^2 + |\eta_2|^2) + \beta_{00}(|\eta_0|^4 + |\eta_2|^4) + 4\beta_{11}|\eta_0|^2|\eta_2|^2 + 4\beta_{02}|\eta_0|^2|\eta_2|^2\cos\varphi_{02} \\ \mathcal{F}_- &= \alpha_1(|\eta_1|^2 + |\eta_3|^2) + \beta_{00}(|\eta_1|^4 + |\eta_3|^4) + 4\beta_{11}|\eta_1|^2|\eta_3|^2 + 4\beta_{02}|\eta_1|^2|\eta_3|^2\cos\varphi_{13}\end{aligned} \tag{4.53}$$

for even and odd L respectively, where $\varphi_{02} = 2(\phi_0 - \phi_2)$ and $\varphi_{13} = 2(\phi_1 - \phi_3)$. Note that β_{02} can actually be taken to be real in this case. Terms with β_{01} and β_{12} are allowed by symmetry but couple different irreps, so we ignore them assuming that α_0 and α_1 are sufficiently far apart. The free energies have the same mathematical form, and are also similar to the free energy for PDW order parameters [228]. For $\beta_{02} > 0$, the phases can always be minimized by setting $\phi_L = \phi_{L+2} \pm \pi/2$, i.e. the two orders are out of phase by a factor of $\pm i$; the two minima for $\beta_{02} < 0$ are $\phi_L = \phi_{L+2}$ and $\phi_L = \phi_{L+2} + \pi$, i.e. the order parameters are both real and either equal or opposite. Whether the two order coexist at all, however, depends on the ratio $(\beta_{02} - \beta_{11})/\beta_{00}$ with a phase transition at $\beta_{02} - \beta_{11} = \beta_{00}/2$ (note that β_{00} and β_{11} are also real).

The non-coexisting solutions are precisely the $\hat{T}_2(\theta_2)$ symmetric solutions, with

the corresponding gap functions being the irrep components as given in Eq. (4.42):

$$\hat{\Delta}^{(0,\pm)} = \begin{pmatrix} \Delta_0 & 0 & 0 & 0 \\ 0 & 0 & 0 & \Delta_2 \\ 0 & 0 & \pm\Delta_0 & 0 \\ 0 & \pm\Delta_2 & 0 & 0 \end{pmatrix}, \hat{\Delta}^{(2,\pm)} = \begin{pmatrix} 0 & 0 & \pm\Delta_2 & 0 \\ 0 & \Delta_0 & 0 & 0 \\ \Delta_2 & 0 & 0 & 0 \\ 0 & 0 & 0 & \pm\Delta_0 \end{pmatrix},$$
$$\hat{\Delta}^{(1,\pm)} = \begin{pmatrix} 0 & \Delta_3 & 0 & 0 \\ \Delta_1 & 0 & 0 & 0 \\ 0 & 0 & 0 & \pm\Delta_3 \\ 0 & 0 & \pm\Delta_1 & 0 \end{pmatrix}, \hat{\Delta}^{(3,\pm)} = \begin{pmatrix} 0 & 0 & 0 & \pm\Delta_1 \\ 0 & 0 & \Delta_3 & 0 \\ 0 & \Delta_1 & 0 & 0 \\ \pm\Delta_3 & 0 & 0 & 0 \end{pmatrix} \quad (4.54)$$

which correspond to states symmetric under $\hat{T}_2(\theta_2)$ with $\theta_2 = \frac{\pi p}{2} L$ and symmetric/anti-symmetric under $\hat{T}_1^2(0)$ for $\pm$ respectively. As for $q = 2$, Δ_ℓ are defined in Eq. (4.30).

For the $\hat{\Delta}^{(L,-)}$ irreps, there is however a phase transition into a state with gap functions forming linear combinations (assuming $\beta_{02} > 0$)

$$\hat{\Delta}^{(\pm1,+)_{1,0}} = \hat{\Delta}^{(0,-)} \pm i\hat{\Delta}^{(2,-)}$$
$$\hat{\Delta}^{(\pm1,-)_{1,0}} = \hat{\Delta}^{(1,-)} \pm i\hat{\Delta}^{(3,-)} \quad (4.55)$$

As can be checked directly, $\hat{\Delta}^{(M,\pm)_{1,0}}$ are symmetric under $\hat{T}_1(\theta_1)$ with $\theta_1 = \frac{\pi p}{2} M$ with odd $M = \pm 1$, consistent with the notation. In addition, as will generalize to all even q, $\hat{\Delta}^{(M,\pm)_{1,0}}$ are symmetric/anti-symmetric under $\hat{T}_2^2$ respectively, requiring the additional $\pm$ index. In a pattern that will also generalize to other even q (and trivially holds also for the previous example of $q = 2$), the corresponding gap functions are even/odd checkerboard matrices [248] symmetric/anti-symmetric under

$\hat{T}_2^2(0)$ respectively:

$$\hat{\Delta}^{(\pm1,+)_{1,0}} = \begin{pmatrix} \Delta_0 & 0 & \mp i\Delta_2 & 0 \\ 0 & \pm i\Delta_0 & 0 & \Delta_2 \\ \pm i\Delta_2 & 0 & -\Delta_0 & 0 \\ 0 & -\Delta_2 & 0 & \mp i\Delta_0 \end{pmatrix},$$
$$\hat{\Delta}^{(\pm1,-)_{1,0}} = \begin{pmatrix} 0 & \Delta_3 & 0 & \mp i\Delta_1 \\ \Delta_1 & 0 & \pm i\Delta_3 & 0 \\ 0 & \pm i\Delta_1 & 0 & -\Delta_3 \\ \mp i\Delta_3 & 0 & -\Delta_1 & 0 \end{pmatrix} \tag{4.56}$$

These happen to be the phases found in Ref. [64] for the special case of Hubbard interactions.

For the $\hat{\Delta}^{(L,+)}$ irreps, again assuming $\beta_{02} > 0$, the phase transition is instead into

$$\begin{aligned} \hat{\Delta}^{(\pm1,+)_{1,1}} &= \hat{\Delta}^{(0,+)} \pm i\hat{\Delta}^{(2,+)} \\ \hat{\Delta}^{(\pm1,-)_{1,1}} &= \hat{\Delta}^{(1,+)} \pm i\hat{\Delta}^{(3,+)} \end{aligned} \tag{4.57}$$

that as the notation indicates are symmetric under $\hat{T}_2(\theta_1)\hat{T}_1(\theta_2)$ with $\theta_0 = \theta_1 + \theta_2 = \frac{\pi p}{2}M$ with odd $M = \pm 1$. Explicitly they are given by the even/odd checkerboard

matrices symmetric/anti-symmetric under $\hat{T}_2^2(0)$ respectively:

$$\hat{\Delta}^{(\pm 1,+)_{1,1}} = \begin{pmatrix} \Delta_0 & 0 & \pm i\Delta_2 & 0 \\ 0 & \pm i\Delta_0 & 0 & \Delta_2 \\ \pm i\Delta_2 & 0 & \Delta_0 & 0 \\ 0 & \Delta_2 & 0 & \pm i\Delta_0 \end{pmatrix},$$
$$\hat{\Delta}^{(\pm 1,-)_{1,1}} = \begin{pmatrix} 0 & \Delta_3 & 0 & \pm i\Delta_1 \\ \Delta_1 & 0 & \pm i\Delta_3 & 0 \\ 0 & \pm i\Delta_1 & 0 & \Delta_3 \\ \pm i\Delta_3 & 0 & \Delta_1 & 0 \end{pmatrix} \tag{4.58}$$

These are distinct from the phases found in Ref. [64]. We get additional phases taking $\beta_{02} < 0$, which results in $\hat{\Delta}^{(M,\pm)_{1,N_2}}$ solutions with even $M = 0, 2$ and $N_2 = 1$ or 0 for $\hat{\Delta}^{(L,\pm)}$ irreps respectively. We thus find that at least one $\mathbb{Z}_4$ symmetry remains unbroken for $q = 4$, though this may change if the even and odd L irreps are allowed to mix or higher order terms are included in the free energy. For examples of a numerical analysis of the former possibility (with some additional symmetries), see Ref. [221].

$q = 3$

The simplest odd q case is $q = 3$ (with $p = 1$ or 2). There is only one MTG irrep in this case, and the free energy is

$$\begin{aligned} \mathcal{F} = {} & \alpha(|\eta_0|^2 + |\eta_1|^2 + |\eta_2|^2) + \beta_{00}(|\eta_0|^4 + |\eta_1|^4 + |\eta_2|^4) \\ & + 4\beta_{11}\left(|\eta_0|^2|\eta_1|^2 + |\eta_1|^2|\eta_2|^2 + |\eta_2|^2|\eta_0|^2\right) \\ & + 4|\beta_{01}||\eta_0||\eta_1||\eta_2|\left(|\eta_0|\cos\varphi_{01}^{(0)} + |\eta_1|\cos\varphi_{01}^{(1)} + |\eta_2|\cos\varphi_{01}^{(2)}\right) \end{aligned} \tag{4.59}$$

where $\beta_{01} = |\beta_{01}|e^{i\theta_{01}}$ is not necessarily real (unlike the $q = 4$ case) and

$$\varphi_{01}^{(L)} = 2\phi_L - \phi_{L+1} - \phi_{L-1} + \theta_{01} \tag{4.60}$$

Unfortunately already in this case we did not find a complete analytical solution. To make some progress, it is convenient to minimize the free energy with respect to $\varphi_{01}^{(L)}$ instead of ϕ_L, noting that there is a constraint $\sum_L \varphi_{01}^{(L)} = 3\theta_{01}$. This can be enforced using a Lagrange multiplier

$$\mathcal{F}_\lambda = \lambda \sum_L \left(\varphi_{01}^{(L)} - \theta_{01}\right) \tag{4.61}$$

and minimizing $\mathcal{F} + \mathcal{F}_\lambda$ with respect to $|\eta_L|$, $\varphi_{01}^{(L)}$ and λ. Minimizing with respect to $\varphi_{01}^{(L)}$ we find that at any local or global extremum,

$$4|\beta_{01}||\eta_0||\eta_1||\eta_2||\eta_L| \sin \varphi_{01}^{(L)} = \lambda \tag{4.62}$$

In particular, $|\eta_L| \sin \varphi_{01}^{(L)}$ are equal for all L in the ground state. This is enough to prove that *if* all of $|\eta_L|$ are in addition equal in the ground state, then the ground state has a $\mathbb{Z}_3$ symmetry.

This is as much as we can determine analytically. Numerically, we find that for the explored parameter range at least one of the MTG symmetries is always unbroken in the ground state and either all of $|\eta_L|$ are equal or only one is non-zero; this is another pattern that we will see generalizes to all q. The sole exception are phase transitions, for example in the special case

$$\mathcal{F} = \alpha|\boldsymbol{\eta}|^2 + \beta|\boldsymbol{\eta}|^4 . \tag{4.63}$$

It is clear that the direction of the vector $\boldsymbol{\eta}$ is arbitrary in the ground state due to the

additional $SU(3)$ symmetry, so symmetry breaking linear combinations are allowed in this case. We cannot definitively state that the MTG cannot be fully broken away from such phase transition points.

The possible distinct $\mathbb{Z}_3$ symmetries in this case are $\hat{T}_2$, $\hat{T}_1$, $\hat{T}_2\hat{T}_1$, and $\hat{T}_2^2\hat{T}_1$ (other cases are redundant). Note that we can thus always take $N_1 = 1$ in $\boldsymbol{\eta}^{(M)_{N_1,N_2}}$. The gap functions symmetric under $\hat{T}_2$ are again the irrep components already given in Eq. (4.28):

$$\hat{\Delta}^{(0)} = \begin{pmatrix} \Delta_0 & 0 & 0 \\ 0 & 0 & \Delta_2 \\ 0 & \Delta_1 & 0 \end{pmatrix}, \hat{\Delta}^{(1)} = \begin{pmatrix} 0 & 0 & \Delta_1 \\ 0 & \Delta_0 & 0 \\ \Delta_2 & 0 & 0 \end{pmatrix}, \hat{\Delta}^{(2)} = \begin{pmatrix} 0 & \Delta_2 & 0 \\ \Delta_1 & 0 & 0 \\ 0 & 0 & \Delta_0 \end{pmatrix} \tag{4.64}$$

where note that Δ_ℓ with $\ell = 0, 1, 2$ as defined in Eq. (4.27) are determined by the gap equation and may be complex. Gap functions symmetric under $\hat{T}_1$ are

$$\hat{\Delta}^{(M)_{1,0}} = \begin{pmatrix} \Delta_0 & \Delta_2 e^{-\frac{2\pi i p M}{3}} & \Delta_1 e^{\frac{2\pi i p M}{3}} \\ \Delta_1 e^{-\frac{2\pi i p M}{3}} & \Delta_0 e^{\frac{2\pi i p M}{3}} & \Delta_2 \\ \Delta_2 e^{\frac{2\pi i p M}{3}} & \Delta_1 & \Delta_0 e^{-\frac{2\pi i p M}{3}} \end{pmatrix} \tag{4.65}$$

Gap functions symmetric under $\hat{T}_2\hat{T}_1$ are

$$\hat{\Delta}^{(M)_{1,1}} = \begin{pmatrix} \Delta_0 & \Delta_2 e^{-\frac{2\pi i p M}{3}} & \Delta_1 e^{\frac{2\pi i p (M+2)}{3}} \\ \Delta_1 e^{-\frac{2\pi i p M}{3}} & \Delta_0 e^{\frac{2\pi i p (M+2)}{3}} & \Delta_2 \\ \Delta_2 e^{\frac{2\pi i p (M+2)}{3}} & \Delta_1 & \Delta_0 e^{-\frac{2\pi i p M}{3}} \end{pmatrix} \tag{4.66}$$

Finally, gap functions symmetric under $\hat{T}_2^2\hat{T}_1$ are

$$\hat{\Delta}^{(M)_{1,2}} = \begin{pmatrix} \Delta_0 & \Delta_2 e^{-\frac{2\pi i p M}{3}} & \Delta_1 e^{\frac{2\pi i p(M+4)}{3}} \\ \Delta_1 e^{-\frac{2\pi i p M}{3}} & \Delta_0 e^{\frac{2\pi i p(M+4)}{3}} & \Delta_2 \\ \Delta_2 e^{\frac{2\pi i p(M+4)}{3}} & \Delta_1 & \Delta_0 e^{-\frac{2\pi i p M}{3}} \end{pmatrix} \tag{4.67}$$

The phases found for the Harper-Hubbard model in Ref. [64] correspond to the $\hat{T}_2\hat{T}_1$ symmetric gaps, which will also be the phase we consider in the context of chiral pairing functions in Sec. 4.5.

4.4.2 General $\mathbb{Z}_q$ Symmetries

We now determine the general form of solutions $\boldsymbol{\eta}^{(M)_{N_1,N_2}}$ symmetric under $\hat{T}(\theta_0) = \hat{T}_2^{N_2}(\theta_2)\hat{T}_1^{N_1}(\theta_1)$ for some choice of $\theta_0 = N_1\theta_1 + N_2\theta_2$ with $N_1, N_2 = 0, \ldots, q-1$. For simplicity, we will only consider the case when the order of this symmetry is q. This is not the case if and only if N_1, N_2 and q all share a common divisor $d \neq 1$. The order of $\hat{T}(\theta_0)$ in that case is m_0 and the degeneracy of the solutions is dq for odd q or $dq/2$ for even q. Below we consider only $d = 1$, and treat the odd and even q separately.

Let us first consider the $\hat{T}_1(\theta_1)$-symmetric order parameters for odd q, with $e^{i\theta_1} = \omega_q^{pM}$. These can be obtained by taking $\eta_0 = \eta$ and sequentially applying $\hat{T}_1(\theta_1)$ to $\boldsymbol{\eta}$. This way we find the components of $\boldsymbol{\eta}^{(M)_{1,0}}$ to be

$$\eta_L^{(M)_{1,0}} = \omega_q^{-pM[L/2]_q}\eta \tag{4.68}$$

where $[L/2]_q = L/2$ if L is even but $[L/2]_q = (L+q)/2$ if ℓ is odd. By construction, applying $\hat{T}_2(0)$ to $\boldsymbol{\eta}^{(M)_{1,0}}$ maps it to $\boldsymbol{\eta}^{(M+2)_{1,0}}$, and again there are q degenerate

solutions. The corresponding gap functions

$$\hat{\Delta}^{(M)_{1,0}} = \sum_L \eta_L^{(M)_{1,0}} \hat{\Delta}^{(L)} \tag{4.69}$$

can be considered as an alternative set of irrep components, now symmetric with respect to $\hat{T}_1(\theta_1)$. Eq. (4.65) provides an example for $q = 3$.

The procedure is essentially the same for all other $\hat{T}(\theta_0)$ symmetries, and we obtain the solutions $\boldsymbol{\eta}^{(M)_{N_1,N_2}}$ with components

$$\eta_{2N_1J}^{(M)_{N_1,N_2}} = \omega_q^{-2pN_1N_2J(J-1)-pMJ}\eta\,. \tag{4.70}$$

If $\gcd(N_1, q) \neq 1$, some components may vanish. Again for simplicity we will not consider that case; in all other cases we can take $N_1 = 1$ without loss of generality since $\hat{T}(\theta_0)$ forms a $\mathbb{Z}_q$ subgroup. To gain a better understanding of these solutions, we consider the implications for the form of the gap functions

$$\hat{\Delta}^{(M)_{N_1,N_2}} = \sum_L \eta_L^{(M)_{N_1,N_2}} \hat{\Delta}^{(L)}\,. \tag{4.71}$$

The symmetry $\hat{T}(\theta_0)$ constrains the elements of these matrices to be of the form

$$\hat{\Delta}_{\ell\ell'}^{(M)_{N_1,N_2}} = \Delta_{\ell-\ell'} \exp\left[i\phi_{\ell+\ell'}^{(M)_{N_1,N_2}}\right]\,, \tag{4.72}$$

where $\Delta_{\ell-\ell'}$ as given in Eq. (4.27) are the same for all M, N_1 and N_2 and depend only on $\ell - \ell'$ that labels which diagonal they are on. The phases $\phi_{\ell+\ell'}^{(M)_{N_1,N_2}}$ on the other hand are different for each M and depend only on $L = \ell + \ell'$, i.e. which anti-diagonal the element is on. From Eq. (4.71) we see that for $N_1 = 1$ and setting $\phi_0^{(M)_{1,N_2}} = 0$

without loss of generality,

$$\phi_L^{(M)_{1,N_2}} = \left[\frac{L}{2}\right]_q \left(\left[\frac{L}{2}\right]_q + 1\right) \frac{2\pi p N_2}{q} + \frac{2\pi p M}{q} \left[\frac{L}{2}\right]_q \tag{4.73}$$

See Eqs. (4.65-4.67) for concrete illustrations of these equations for $q = 3$. The case when $N_1 \neq 1$ is similar with the phases permuted accordingly.

Even q

The expressions for even q are essentially the same as for odd q but with some minor modifications to keep track of the fact that there are four different irreps in this case. Note that within a given irrep, only η_L with the same parity of L are non-zero, so the symmetric order parameters have an additional index. For example the $\hat{T}_1(\theta_1)$-symmetric order parameters are $\boldsymbol{\eta}^{(M,\pm)_{1,0}}$ with components given by the same expression as for odd q, Eq. (4.68):

$$\eta_L^{(M,\pm)_{1,0}} = \omega_q^{-pML/2}\eta \tag{4.74}$$

but with the understanding that only even or odd L components are non-zero. In general, the order parameters with symmetries other than $\hat{T}_2(\theta_2)$ are given by $\boldsymbol{\eta}^{(M,\pm)_{N_1,N_2}}$. The meaning of the labels depends on the the parity of N_1. If N_1 is odd, $\pm$ labels the parity of L of non-zero components while M is determined by which of the four irreps the gap function belongs to, with $\hat{T}_1^{q/2}(0)$ acting as $(-1)^M$ on the order parameter. If N_1 is even, on the other hand, M must have the same parity as L, while $\pm$ corresponds to $\hat{T}_1^{q/2}(0)$ acting as ± 1 in the irrep. For odd N_1, Eq. (4.70) gives $\boldsymbol{\eta}^{(M,+)_{N_1,N_2}}$ with even L components. The odd L component combinations $\boldsymbol{\eta}^{(M,-)_{N_1,N_2}}$ are given by essentially the same formula:

$$\eta_{2N_1J+1}^{(M,-)_{N_1,N_2}} = \omega_q^{-2pN_1N_2J(J-1)-pMJ}\eta\,. \tag{4.75}$$

For even N_1, the RHSs of Eqs. (4.70) and (4.75) give the components of $\boldsymbol{\eta}^{(M,\pm)_{N_1,N_2}}$ for even and odd M respectively. We will consider odd N_1 below for simplicity.

The parity of L of the non-zero components can be considered as the eigenvalue of $\boldsymbol{\eta}^{(M,\pm)_{N_1,N_2}}$ under $\hat{T}_2^{q/2}(0)$. We note that this symmetry places a particular constraint on the corresponding pairing matrices $\hat{\Delta}$, on which it acts as

$$\hat{\Delta} \xrightarrow{\hat{T}_2^{q/2}(0)} \hat{\sigma}^{q/2}\hat{\Delta}\hat{\sigma}^{q/2} \tag{4.76}$$

(note that $\hat{\sigma}_{\ell\ell}^{q/2} = (-1)^{\ell}$). This implies that the gap functions

$$\hat{\Delta}^{(M,\pm)_{N_1,N_2}} = \sum_L \eta_L^{(M,\pm)_{N_1,N_2}} \hat{\Delta}^{(L,(-1)^M)} \tag{4.77}$$

that are even or odd under $\hat{T}_2^{q/2}(0)$ are even or odd checkerboard matrices [248]: $\hat{\Delta}_{\ell\ell'}^{(M,\pm)_{N_1,N_2}} = 0$ whenever $\ell + \ell'$ is odd or even respectively for $+$ and $-$ respectively. We saw this explicitly for the $q = 2$ and 4 cases considered in Sec. 4.4.1. Note that the term $\hat{\Delta}^{(M,+)_{N_1,N_2}\dagger}\hat{\Delta}^{(M,-)_{N_1,N_2}}$ is odd under $\hat{T}_2^{q/2}$ so such a term is not allowed in the free energy and its trace vanishes because a product of an even and an odd checkerboard matrix is an odd checkerboard matrix with zero diagonal. This confirms once again that the four irreps for even q are not mixed at the leading second order in the free energy.

Again to understand the solutions better, we consider the form of the gap functions corresponding to the order parameters $\boldsymbol{\eta}^{(M,\pm)_{N_1,N_2}}$. As for odd q, we can express the elements of $\hat{\Delta}^{(M,\pm)_{N_1,N_2}}$ as

$$\hat{\Delta}_{\ell\ell'}^{(M,\pm)_{N_1,N_2}} = \Delta_{\ell-\ell'} \exp\left[i\phi_{\ell+\ell'}^{(M,\pm)_{N_1,N_2}}\right] \tag{4.78}$$

but with a caveat that $\ell - \ell'$ in $\Delta_{\ell-\ell'}$ is defined modulo $2q$ and restricted to be even or odd for $\pm$ respectively, as in Eq. (4.30), and additionally satisfying $\Delta_{\ell+q} = (-1)^M \Delta_\ell$.

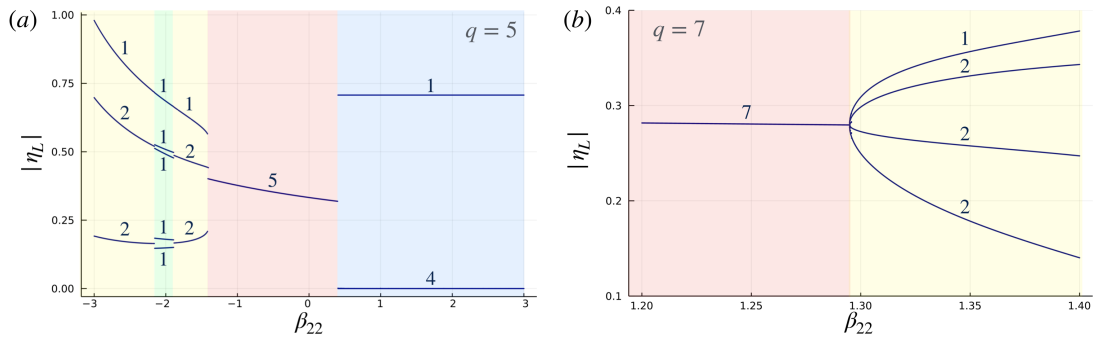

Figure 4.2: Numerical solutions of uniform GL equations $|\eta_L|$ for (a) $q = 5$ and (b) $q = 7$ as a function of β_{22} treated as a variable parameter with $\beta_{23} = 2$, $\beta_{12} = 1.7$ for $q = 5$ and $\beta_{12} = 1.6$ for $q = 7$, and all other $\beta_{MN} = 1$. Numbers indicate the number of equal $|\eta_L|$ on each segment. For $q = 5$, we find four first order phase transitions between four kinds of phases: a $\hat{T}_2$ symmetric phase with a single non-zero η_L (blue); a $\mathbb{Z}_5$ symmetric phase with all $|\eta_L|$ equal (red); a phase with $\mathcal{I}$ symmetry with pairs of equal $|\eta_L|$ except for one (yellow); and a phase with no symmetries where none of the $|\eta_L|$ are equal (green). For $q = 7$ we find a second order phase transition between a $\mathbb{Z}_7$ symmetric phase with all $|\eta_L|$ equal (red) and a $\mathcal{I}$ symmetric phase with pairs of equal $|\eta_L|$ except for one (yellow).

In this case only the relative phases between even or odd L anti-diagonals are defined, so for $N_1 = 1$ we have:

$$\begin{aligned}\phi_L^{(M,+)_{1,N_2}} &= \phi_0 + \frac{L(L+2)}{4}\frac{2\pi p N_2}{q} + \frac{\pi p M L}{q} \\ \phi_L^{(M,-)_{1,N_2}} &= \phi_1 + \frac{(L-1)(L+3)}{4}\frac{2\pi p N_2}{q} + \frac{\pi p M (L-1)}{q}\end{aligned} \tag{4.79}$$

As for odd q, the phase relations for $N_1 \neq 1$ are similar. See Eqs. (4.52, 4.56,4.58) for concrete illustrations for $q = 2$ and 4.

$\mathbb{Z}_q$-symmetric and Non-Symmetric Solutions of the GL Equations

So far in this subsection we have have simply constructed configurations $\boldsymbol{\eta}^{(M)_{N_1,N_2}}$ in Eqs. (4.70,4.75) that respect $\hat{T}(\theta_0)$ symmetry. The corresponding gap functions in

Eq. (4.71) satisfy the defining properties

$$\hat{\Delta}^{(M)_{N_1,N_2}} \xrightarrow{\hat{T}_1(0)} \omega_q^{pM} \hat{\Delta}^{(M)_{N_1,N_2}} \tag{4.80a}$$

$$\hat{\Delta}^{(M)_{N_1,N_2}} \xrightarrow{\hat{T}_2(0)} \hat{\Delta}^{(M+2N_1)_{N_1,N_2}} \tag{4.80b}$$

for odd q; the relations are the same for $\hat{\Delta}^{(M,+)_{N_1,N_2}}$ in Eq. (4.77) for even q, while for $\hat{\Delta}^{(M,-)_{N_1,N_2}}$ the last relation becomes

$$\hat{\Delta}^{(M,-)_{N_1,N_2}} \xrightarrow{\hat{T}_2\left(\frac{2\pi p}{q}\right)} \hat{\Delta}^{(M+2N_1,-)_{N_1,N_2}} , \tag{4.81}$$

to be consistent with the fact that in this irrep $\hat{T}_2^{q/2}(0)$ acts as -1 on $\hat{\Delta}^{(M,-)_{N_1,N_2}}$.

We still need to show that the configurations $\boldsymbol{\eta}^{(M)_{N_1,N_2}}$ are actually solutions of the GL equations and are therefore always at least local minima of the free energy. To see this, note that all the symmetric configurations have the important property that all the components η_L have the same magnitude and differ only by a phase, $\eta_L = \eta e^{i\phi_L}$ with real η (more precisely, all non-zero η_L have the same magnitude). Plugging this ansatz into Eq. (4.48) we find the equation for η:

$$\eta = \sqrt{\frac{-\alpha}{2\sum_{MN} |\beta_{MN}| \cos \varphi_{MN}^{(L)}}} \tag{4.82}$$

where

$$\varphi_{MN}^{(L)} = \phi_{L+M} + \phi_{L-M} - \phi_{L+N} - \phi_{L-N} + \theta_{MN} \tag{4.83}$$

with $\beta_{MN} = |\beta_{MN}| e^{i\theta_{MN}}$. The solution exists only if the RHS of Eq. (4.82) is independent of L. For symmetric gaps it is easy to check from Eq. (4.73) and (4.79) that in fact $\varphi_{MN}^{(L)} = \varphi_{MN}^{(0)}$ for all L. Therefore, as claimed above, symmetric solutions

are always extrema of the free energy. The free energy at these extrema is

$$\mathcal{F}_{N_1\neq 0,N_2} = -\frac{\alpha^2(2q-1)}{4\sum_{MN}|\beta_{MN}|\cos\varphi^{(L)}_{MN}}\,. \tag{4.84}$$

(Note that if both N_1 and N_2 divide q, some η_L are zero, but all non-zero components have equal magnitudes.)

Although we thus conclude that the $\hat{T}(\theta_0)$-symmetric order parameters are possible ground states of the system, it is not true that the ground state is necessarily symmetric. Though we did find this to be the case for $q \leq 4$ in Sec. 4.4.1 (analytically for $q = 2$ and 4 and numerically for $q = 3$), already for $q = 5$ we find numerically that the MTG may be fully broken in the ground state, as shown in Fig. 4.2 (a). With the particular choice of parameters, we observe first order phase transitions between phases with only one η_L being non-zero and all $|\eta_L|$ equal, i.e. phases with different $\mathbb{Z}_q$ symmetries; a phase transition into a phase with pairs of $|\eta_L|$ being equal except for one that is symmetric under $\eta_L \to \eta_{M-L}$ for some M (as noted above, this is an accidental symmetry in our case); and a phase transition into a phase where none of the $|\eta_L|$ are equal and there are no symmetries. There may also be second order phase transitions, as we find for $q = 7$ (see Fig. 4.2 (b)).

4.4.3 Summary

To summarize this section, we found that the GL equations Eq. (4.48) always have solutions with a $\mathbb{Z}_q$ symmetry $\hat{T}(\theta_0) = \hat{T}_2^{N_2}(\theta_2)\hat{T}_1^{N_1}(\theta_1)$ with $\theta_0 = N_1\theta_1 + N_2\theta_2 = \frac{2\pi p}{q}M$, and $N_1, N_2 = 0, \ldots, q-1$. N_1 and N_2 are determined in the ground state by which of $\mathcal{F}_{N_1,N_2}$, given in Eqs. (4.49) and (4.84) is smallest (assuming the ground state does not completely break the MTG), while each value of $M = 0, 2, 4, \ldots$ corresponds to a degenerate solution. For even q, only M of the same parity give degenerate solutions, while all M are degenerate for odd q. The solutions are thus q-fold degenerate for odd

q and $q/2$-fold degenerate for even q, corresponding to the dimensions of the MTG irreps, and there is an additional $\mathbb{Z}_2$ symmetry for even q. Additional degeneracy may occur if other crystalline symmetries are present, e.g. the inversion-like symmetry $\mathcal{I} : \eta_L \to \eta_{-L}$ that exists in presence of two-fold rotation symmetry (and is an accidental symmetry at fourth order of the free energy). Since $\hat{T}_2(0)$ is broken by all phases except $\boldsymbol{\eta}^{(0)_{0,1}}$, in all other cases the unit cell is extended in real space by an additional factor of q along the $\mathbf{a}_2$ direction, resulting in a unit cell $q \times q$ larger than the normal state unit cell in the absence of the magnetic field (note that $\hat{T}_j^q(0)$ are always unbroken).

The symmetric solutions are given by $\boldsymbol{\eta}^{(M)_{N_1,N_2}}$ for odd q ($\boldsymbol{\eta}^{(M,\pm)_{N_1,N_2}}$ for even q) in Eqs. (4.68,4.70). As a special case, $\boldsymbol{\eta}^{(L)_{0,1}}$ are simply vectors with a single non-zero element. These states satisfy the defining relations Eqs. (4.80a-4.80b), which in particular imply that if $N_1 \neq 0$, applying $\hat{T}_2$ to the ground state shifts $M \to M + 2$; if $N_1 = 0, N_2 = 1$, then applying $\hat{T}_1(0)$ shifts $L \to L + 2$ instead. In either case the degenerate ground states are simply shifted version of each other.

An important property of the symmetric solutions is that all non-zero components η_L have the same magnitude η given by Eq. (4.82). Moreover, the relative phases ϕ_L are also constrained by symmetry, which also fixes the phase relations between anti-diagonals of $\hat{\Delta} = \sum_L \eta_L \hat{\Delta}^{(L)}$, while the phases between diagonals is fixed by the interaction via the linearized gap equation Eq. (4.16). The phase relations for $q = 3$ and $q = 4$ (and $p = 1$) have been noted earlier in Ref. [64] as a consequence of minimizing a Ginzburg-Landau free energy with the assumption of Hubbard interactions. Here we clarified that the phase relations in those cases are a consequence of the symmetry of the solutions themselves and found the phase relations for all q assuming this symmetry remains unbroken. The ground states found in Ref. [64] have $\hat{T}$ symmetry with either $N_1 = N_2 = 1$ or $N_2 = -1$ for $q = 3$ (the two are found to be degenerate) and $N_1 = 1, N_2 = 0$ for $q = 4$; for even q we also need to specify

whether the solutions are symmetric or anti-symmetric with respect to $\hat{T}_2^{q/2}$, but Ref. [64] finds the two cases to be degenerate. The extra degeneracy in both $q = 3$ and $q = 4$ cases can be understood as a result of extra symmetry of the square lattice. Similar partial symmetry breaking of the MTG has been seen in Ref. [67], and in Refs. [55, 222] in the context of the related bosonic Hofstadter model. These authors did not report the phase relations between condensates with different momenta, but Refs. [55, 222] noted that the superfluid state necessarily at least partially breaks the MTG symmetries, essentially for the same reason that the Hofstadter SC state does as we found in this chapter.

Though we showed analytically that the GL equations *always* have symmetric solutions, we emphasize that this only guarantees that such states are *local* minima of the free energy, not necessarily *global* minima that are the true ground states. This implies that extra care must be taken when analyzing such systems numerically, as some methods are susceptible to getting stuck in local minima. Indeed, we find explicit cases for $q = 5$ for which the MTG is completely broken, see Fig. 4.2. The additional symmetry breaking can happen in two ways: first, the magnitudes of non-zero η_L may not all be identical; second, the phase relations determined by Eqs. (4.68,4.70,4.74,4.75) may be violated even if the magnitudes are equal. The latter can happen due to frustration between $\varphi_{MN}^{(L)}$ in Eq. (4.83) for different values of $M \neq N$. We also note that the accidental $\mathcal{I}$ symmetry can be 'spontaneously' broken. The degeneracy of the states with a completely broken MTG is q^2, but note that the new unit cell in real space is the same as in the $\mathbb{Z}_q$ symmetric phases. Interestingly, in the limit of large q the unit cell may exceed the size of a finite sample, resulting in a phase with essentially no translational order, similar to a vortex glass phase and may melt into a vortex liquid-like phase due to thermal fluctuations [136, 249–254]. We leave this possibility for a future study.

4.5 BdG Spectrum and Chiral Hofstadter Superconductivity

Having identified the $\mathbb{Z}_q$-symmetric Hofstadter SC phases, we now want to consider their excitation spectrum and topological properties. For this purpose we consider the $2q \times 2q$ BdG Hamiltonian Eq. (4.10) describing pairing of electrons in a single Hofstadter band:

$$\mathcal{H}_{BdG}(\mathbf{p}) = \begin{pmatrix} \varepsilon(\mathbf{p})_{q\times q} & \hat{\Delta}(\mathbf{p}) \\ \hat{\Delta}^\dagger(\mathbf{p}) & -\varepsilon(-\mathbf{p})_{q\times q} \end{pmatrix} \tag{4.85}$$

with the gap function $\hat{\Delta}$ symmetric under some order q MTG symmetry

$$\hat{T} = \hat{T}_2^{N_2}(\theta_2)\hat{T}_1^{N_1}(\theta_1) \tag{4.86}$$

with $\theta_0 = N_1\theta_1 + N_2\theta_2 = \frac{2\pi p}{q}M$ and $M, N_1, N_2 = 0, \ldots, q-1$. For simplicity, we will set $N_1 = 1$ and $N_2 = N$ in this section. Interestingly, this additional symmetry allows us to completely diagonalize the BdG Hamiltonian in the spin polarized limit for any q, as we show below.

In general, symmetry can also affect the topology of the system, potentially giving rise to symmetry protected topological phases (SPTs) [21, 255–257]. Familiar cases are SPTs protected by anti-unitary symmetries such as PHS and time-reversal symmetry, as well as their unitary product, that are classified according to the 10-fold way [258–260]. This classification includes helical and chiral topological superconductors (TSCs) [202, 204], with the best known example of the latter being the chiral p-wave SC considered in a spin polarized system [200], characterized by a non-trivial Chern number. Including additional unitary symmetries in the classification results in additional SPTs, for example crystalline SPTs protected by additional lattice symmetries that include crystalline TSCs, e.g. inversion or mirror symmetries [127, 261–265].

This also includes translational symmetry, which is generally assumed in all other classifications but is itself known to give rise to non-trivial SPTs, as well as symmetry enriched topological (SETs) phases with topological order [266]. Similarly, MTG symmetries are well known to play a role in determining Chern numbers in the quantum Hall effect [22, 28, 267].

It is therefore natural to ask whether the MTG symmetries can also give rise to novel TSC phases realised by Hofstadter superconductors. Remarkably, we demonstrate in Sec. 4.5.2 that Hofstadter superconductors described by the BdG Hamiltonian Eq. (4.10) can indeed realize SPT phases protected by MTG symmetries where the parity of the Chern numbers is the same as the parity of q. This result establishes that Hofstadter superconductors with a fully gapped spectrum fall into two topological classes according to the parity of q; i.e., they support non-Abelian (Abelian) excitations for odd (even) q. We illustrate the possible topological phase transitions for a specific form of the gap functions explicitly in Sec. 4.5.2 for $q = 3$ and 5.

Symmetries, including crystalline symmetries like inversion, can also lead to topologically protected gapless excitations [121, 122, 257, 263, 264, 268, 269], resulting in nodal SCs or Bogoliubov Fermi surfaces (BFSs) [121–132]. We find that in Hofstadter SCs this can happen in the presence of parity symmetry $\mathcal{P}$ that together with PHS can protect BFSs. In particular, we show in Sec. 4.5.3 that the $\mathbb{Z}_2$ topological invariant $\nu_{\mathbb{Z}_2}$ defined in [123] is trivial for even q but non-trivial for odd q, implying the existence of a BFS in that case. Though it is trivial for even q, we propose a new topological invariant $\nu_{\mathbb{Z}_2,0}$ that can be defined only in the presence of the MTG and only if M and $N_2 = N$ in Eq. (4.86) have the same parity, and which remains non-trivial in that case.

4.5.1 Symmetry and Spectrum of the BdG Hamiltonian

We first review the action of symmetries on the BdG Hamiltonian. If a general symmetry acts as a matrix $S(\mathbf{p})$ on the fermionic annihilation operators $d_{\mathbf{p},\ell}$, it results in the action on the Nambu spinor $\Psi_{\mathbf{p},\ell} = (d_{\mathbf{p},\ell}, d^{\dagger}_{-\mathbf{p},\ell})$

$$\tilde{S}(\mathbf{p}) = \begin{pmatrix} S(\mathbf{p}) & 0 \\ 0 & S^*(-\mathbf{p}) \end{pmatrix} . \tag{4.87}$$

For example, a $U(1)$ symmetry $U(\theta)$ given by $d_{\boldsymbol{p},\ell} \to e^{i\theta}\, d_{\boldsymbol{p},\ell} \equiv U(\theta) d_{\boldsymbol{p},\ell}$ is represented in the BdG formalism by

$$\tilde{U}(\theta) = \begin{pmatrix} e^{i\theta} & 0 \\ 0 & e^{-i\theta} \end{pmatrix} . \tag{4.88}$$

The symmetries act on the BdG Hamiltonian as $\tilde{S}(\mathbf{p})\mathcal{H}_{BdG}(\mathbf{p})\tilde{S}^{-1}(\mathbf{p})$, which is compatible with the transformation of the gap function in Eq. (4.19). As discussed in Sec. 4.3.1, since the $U(1)$ symmetry is broken by the SC phase, we are led to consider the family of symmetries $\tilde{S}(\mathbf{p}, \theta_0) = \tilde{U}(\theta_0/2)\tilde{S}(\mathbf{p})$. Note that if $\tilde{S}^n = 1$, then $e^{i\theta_0}$ is an n^{th} root of unity.

Furthermore, we observe that the phase $e^{i\theta_0}$ is encoded in the commutation relations of $\tilde{S}$ and the PHS $\mathcal{C} = \tau^x \mathcal{K}$ where τ^j are Pauli matrices acting on the particle/hole sectors of the Nambu spinor and $\mathcal{K}$ is complex conjugation:

$$\tilde{S}(\mathbf{p}, \theta_0)\mathcal{C} = e^{-i\theta_0}\mathcal{C}\tilde{S}(-\mathbf{p}, \theta_0) . \tag{4.89}$$

We remark that these commutation relations have been used to classify gapless and fully gapped crystalline topological superconducting phases for $\mathbb{Z}_2$ symmetries with $\tilde{S}^2 = 1$, in which case the two possibilities $e^{i\theta_0} = \pm 1$ result in different topological invariants [121, 122, 203, 263, 264]. We leave the general question of whether the same

approach can lead to new topological classifications in the presence of $\mathbb{Z}_q$ symmetry for a future study.

Here we will only invoke the classification in Sec. 4.5.3 for the parity symmetry $\mathcal{P}$ that reverses $\mathbf{p} \to -\mathbf{p}$ and acts on the BdG Hamiltonian as

$$\tilde{\mathcal{P}}(0)\mathcal{H}_{BdG}(\boldsymbol{p})\tilde{\mathcal{P}}^{\dagger}(0) = \mathcal{H}_{BdG}(-\boldsymbol{p})\,. \tag{4.90}$$

The normal state is symmetric under $\mathcal{P}$, consistent with the condition $\varepsilon(\mathbf{p}) = \varepsilon(-\mathbf{p})$ necessary to guarantee the pairing instability in the first place. Note that we refer to $\mathcal{P}$ as parity symmetry since while it is similar to inversion symmetry, the full inversion symmetry also acts on the patch indices as $\ell \to -\ell$. The gap function of the paired state may have either even or odd parity, $\hat{\Delta}(\mathbf{p}) = \pm\hat{\Delta}(-\mathbf{p})$, in which case the BdG Hamiltonian is symmetric under $\tilde{\mathcal{P}}(0)$ or $\tilde{\mathcal{P}}(\pi)$ respectively. Alternatively, $\tilde{\mathcal{P}}(\theta_0)$ may be broken for any choice of θ_0. Note that due to the PHS relation $\hat{\Delta}(\mathbf{p}) = -\hat{\Delta}^T(-\mathbf{p})$, even and odd parity gap functions are skew-symmetric or symmetric matrices, $\hat{\Delta}^T(\mathbf{p}) = \mp\hat{\Delta}(\mathbf{p})$ respectively.

Finally, the MTG symmetry $\hat{T}(\theta_0) = \hat{T}_2^N(\theta_2)\hat{T}_1(\theta_1)$ with $\theta_0 = \frac{2\pi p}{q}M$ and $M, N = 0, \ldots, q-1$ acts in the Nambu basis via

$$\tilde{T}(\theta_0) = \begin{pmatrix} e^{i\theta_0/2}\hat{\sigma}^{-N_2}\hat{\tau}^{N_1} & 0 \\ 0 & e^{-i\theta_0/2}\hat{\sigma}^{N_2}\hat{\tau}^{N_1} \end{pmatrix} \tag{4.91}$$

where $\hat{\tau}$ and $\hat{\sigma}$ are the shift and clock matrices defined in Eq. (4.3). With this symmetry the gap function $\hat{\Delta}$ has the form given in Eqs. (4.72) and (4.78) for odd and even q respectively:

$$\hat{\Delta}^{(M)}_{\ell\ell'} = \Delta_{\ell-\ell'} \exp\left[i\phi^{(M)}_{\ell+\ell'}\right]\,; \tag{4.92}$$

some of the indices are assumed to be fixed and thus we omit them for clarity. Due to the breaking of the MTG symmetries, there are q or $q/2$ degenerate ground states for

different values of M. The phases ϕ_L determined by the $\tilde{T}$ symmetry are given in Eqs. (4.73) and (4.79). The functions $\Delta_\ell(\mathbf{p})$, defined in Eqs. (4.27) and (4.30) for odd and even q respectively, are ultimately determined by the microscopic interactions Eq. (4.4) via the gap equation Eq. (4.16). In our phenomenological approach we treat them as arbitrary functions. Note that in the spin polarized case considered here, PHS additionally requires $\Delta_\ell(\mathbf{p}) = -\Delta_{-\ell}(-\mathbf{p})$; in particular, Δ_0, as well as Δ_q for even q (for which ℓ is defined modulo $2q$), have to be an odd function of $\mathbf{p}$, which in general has to be chiral for the spectrum to be fully gapped.

As with any symmetry, we can simultaneously diagonalize the BdG Hamiltonian and $\tilde{T}$. In particular, since $\tilde{T}$ is two-fold degenerate, we can write the BdG Hamiltonian Eq. (4.10) in a 2×2 block-diagonal form using a basis that simultaneously diagonalizes $\tilde{T}(0)$. This is useful because the eigenstates of $\tilde{T}(0)$ are known: the eigenvalues of the matrix $\hat{\sigma}^N\hat{\tau}$ are $\lambda^{(n)} = \omega_q^{\frac{pN(q+1)}{2}}\omega_q^{pn}$, with corresponding eigenstates

$$f_{\mathbf{p},n} = \frac{1}{\sqrt{q}}\omega_q^{pN\frac{\ell(\ell+1)-\ell(q+1)}{2}-pn\ell}d_{\mathbf{p},\ell} \tag{4.93}$$

with a sum over $\ell = 0, \ldots, q-1$ on the right-hand side implied and with $n = 0, \ldots, q-1$ being the index in the new basis. Using this new basis we can define a new Nambu spinor $\Psi'_{\mathbf{p},n} = (f_{\mathbf{p},n}, f^\dagger_{-\mathbf{p},n})$ and the corresponding transformed BdG Hamiltonian. For odd q, the gap function for the M^{th} ground state as given in Eq.

(4.71) and (4.73) becomes a L^{th} anti-diagonal matrix $\hat{\Delta}'$ with $L = N - M$ modulo q:

$$\hat{\Delta}' = \begin{pmatrix} & & & \hat{\Delta}'_{0,L} & & & \\ & & \hat{\Delta}'_{1,L+1} & & & & \\ & \iddots & & & & & \\ \hat{\Delta}'_{L,0} & & & & & & \\ & & & & & & \hat{\Delta}'_{L+1,q} \\ & & & & & \iddots & \\ & & & & \hat{\Delta}'_{q,L+1} & & \end{pmatrix} \tag{4.94}$$

with the only non-zero elements given by

$$\hat{\Delta}'_{n,L-n} = \frac{1}{2}\sum_{\ell=0}^{q-1} \omega^{-N\frac{\ell^2}{4}+\ell(n+M/2)} \left[1 + (-1)^\ell + (1-(-1)^\ell)(-1)^{pM} i^{pqN}\right] \Delta_\ell \equiv \Delta'_{2n-L} \tag{4.95}$$

while the rest vanish; this formula holds for the even q case as well with ℓ defined modulo $2q$ and restricted to only even or only odd values depending on the irrep. In this basis, the gap functions for different values of M correspond to different anti-diagonals, just as the $\hat{T}_2(\theta_2)$ symmetric irrep components $\hat{\Delta}^{(L)}$ defined in Eq. (5.31).

For a fixed M, after a reshuffling the transformed BdG Hamiltonian splits into 2×2 blocks. For example, for $q = 3$ and $L = 2$ we have

$$\mathcal{H}'_{BdG} = \begin{pmatrix} \varepsilon & 0 & 0 & 0 & 0 & \Delta'_1 \\ 0 & \varepsilon & 0 & 0 & \Delta'_0 & 0 \\ 0 & 0 & \varepsilon & \Delta'_2 & 0 & 0 \\ 0 & 0 & \Delta'^*_2 & -\varepsilon & 0 & 0 \\ 0 & \Delta'^*_0 & 0 & 0 & -\varepsilon & 0 \\ \Delta'^*_1 & 0 & 0 & 0 & 0 & -\varepsilon \end{pmatrix} \tag{4.96}$$

It is easy to read off the 2×2 blocks, and for any q they are

$$\mathcal{H}_{BdG,2n-L} = \begin{pmatrix} \varepsilon & \Delta'_{2n-L} \\ \Delta'^{*}_{2n-L} & -\varepsilon \end{pmatrix} . \tag{4.97}$$

The BdG Hamiltonian thus splits into q blocks, each being a single band triplet SC with effective gap function Δ'_{2n-L}. The eigenvalues of the 2×2 blocks are simply

$$E^{(M)}_{n\pm}(\mathbf{p}) = \pm\sqrt{\varepsilon^2(\mathbf{p}) + \left|\Delta'_{2n-L}(\mathbf{p})\right|^2}, \tag{4.98}$$

and the Nambu eigenspinors of the BdG Hamiltonian are

$$\left|\Upsilon^{(M)}_{n\pm}\right\rangle = \frac{(\varepsilon + E^{(M)}_{n\pm})\hat{\mathbf{e}}_{n,u} + \Delta'_{2n-L}\hat{\mathbf{e}}_{-n-M,v}}{\sqrt{(\varepsilon + E^{(M)}_{n\pm})^2 + |\Delta'_{2n-L}|^2}} , \tag{4.99}$$

where $\hat{\mathbf{e}}_{n,u}$ and $\hat{\mathbf{e}}_{n,v}$ are unit basis vectors with u and v denoting particle and hole components of the spinors.

4.5.2 Chern Number Parity and Phase Transitions

As in the regular spin polarized SC [200], in the spin polarized Hofstadter SC the order parameter is either gapless or chiral. The fact that in the presence of the $\mathbb{Z}_q$ symmetry the BdG Hamiltonian has a 2×2 block structure in Eq. (4.97) implies that the total Chern number can be computed as a sum of Chern numbers of each block given by integrating the Berry curvature $\mathbf{F}^{(M)}_{n\pm}$ defined using the Nambu eigenspinor Eq. (4.99):

$$\mathbf{F}^{(M)}_{n\pm} = -i\boldsymbol{\nabla} \times \left\langle \Upsilon^{(M)}_{n\pm} \right| \boldsymbol{\nabla} \left| \Upsilon^{(M)}_{n\pm} \right\rangle . \tag{4.100}$$

Here we observe that with the chemical potential in the normal state fixed, the parity of the Chern numbers cannot change in a topological phase transition, assuming the normal state Fermi surface does not cross high-symmetry points. This is because the Chern number changes at the phase transition due to the gap closing at Dirac nodes, as happens for example in phase transitions in quantum Hall systems and Chern insulators [22, 27, 28, 60]. In contrast to Chern insulators and quantum Hall states, in chiral SCs the Dirac nodes appear in pairs due to PHS that maps a Dirac node at $\mathbf{p}_D$ to a second node at $-\mathbf{p}_D$, which, under general conditions, satisfies $\mathbf{p}_D \neq -\mathbf{p}_D$. The condition $\varepsilon(\mathbf{p}) = \varepsilon(-\mathbf{p})$ together with Eq. (4.98) imply that the nodes moreover appear at zero energy and at the Fermi momentum. The change in the Chern number associated with each node in the pair is the same, and therefore the total change in the Chern number is an even integer [6].

This implies that if the spin-polarized Hofstadter SC is not gapless, its Chern number has the same parity as q. To see this, consider the special case when $\hat{\Delta}$ is diagonal, i.e. $\Delta_\ell(\mathbf{p})$ are all zero in Eq. (4.92) except for $\Delta_0(\mathbf{p})$. For odd q, the BdG Hamiltonian splits into q identical 2×2 blocks; for even q, the blocks only differ by an overall momentum-independent phase of the gap function. Since $\Delta_0(\mathbf{p})$ has to be an odd function of momentum, the resulting spectrum is fully gapped only if $\Delta_0(\mathbf{p}) \propto (p_x \pm ip_y)^m$ with odd values of m. The Chern number for each block is therefore the same odd number (for any parity of q). The total Chern number is the sum of the Chern numbers of each block, and is therefore even or odd for even and odd q respectively. Since the Chern number can only change by an even integer as $\Delta_\ell(\mathbf{p})$ are varied, we conclude that the Chern number parity is always the same as the parity of q for any choice of $\Delta_\ell(\mathbf{p})$. The assumption of $\tilde{T}$ symmetry can be lifted,

[6] Note that if the Fermi surface does contain high-symmetry points with $\mathbf{p}_D = -\mathbf{p}_D$, then $\hat{\Delta}(\mathbf{p}_D)$ is an anti-symmetric matrix by PHS, which as we discuss in Sec. 4.5.3 implies that $\Delta'_n(\mathbf{p}_D)$ that appear in the eigenvalues of the BdG Hamiltonian in Eq. (4.98) satisfy $\Delta'_{-n}(\mathbf{p}_D) = -\Delta'_n(\mathbf{p}_D)$. As a result, there are band touchings at $\mathbf{p}_D$ and the Berry connection, along with the Chern number, is not well-defined unless we assume that the Fermi surface does not contain such high-symmetry points.

but note that the presence of q bands is a direct consequence of the MTG symmetry of the normal state.

Phase Diagrams for $q = 3$ and 5

In this subsection we illustrate the conservation of the parity of the Chern number in the special cases of $q = 3$ and 5, and obtain generic phase diagrams. Here we will assume that $\tilde{T} = \tilde{T}_2(0)\tilde{T}_1(0)$, corresponding to $N_1 = N_2 = 1$ and $M = 0$. For $q = 3$ the corresponding gap function was given in Eq. (4.66):

$$\hat{\Delta} = \begin{pmatrix} \Delta_0 & \Delta_1 & \Delta_2 e^{-i2\pi/3} \\ \Delta_2 & \Delta_0 e^{-i2\pi/3} & \Delta_1 \\ \Delta_1 e^{-i2\pi/3} & \Delta_2 & \Delta_0 \end{pmatrix}. \tag{4.101}$$

We consider the functions $\Delta_\ell(\mathbf{p})$ to be of the following general form:

$$\begin{aligned} \Delta_0(\boldsymbol{p}) &= a_0(\boldsymbol{p})(p_x + ip_y)/p_F, \\ \Delta_1(\boldsymbol{p}) &= -\Delta_2(-\boldsymbol{p}) = a_1(\boldsymbol{p})(p_x + ip_y)/p_F + b_1(\boldsymbol{p}) \end{aligned} \tag{4.102}$$

where $p_F = \sqrt{2m\mu}$ and a_0, a_1 and b_1 are complex even functions of $\mathbf{p}$. The pairing matrix is such that in the limit $\Delta_1 = 0$ the spectrum remains fully gapped unless $a_0 = 0$; in that case note that the total Chern number is just q times the winding of $\Delta_0(\mathbf{p})$.

We first consider the simplest case when a_0, a_1 and b_1 are constants and compute the Chern number numerically using the algorithm in [187]. We identify two phases with Chern numbers $C = -3$ and $C = -1$, as well as a gapless phase at $a_0 = a_1 = 0$. The $C = -3$ is the expected phase for $\Delta_1 = \Delta_2 = 0$, but once b_1 is sufficiently large there is a phase transition into the $C = -1$ phase. The phase boundary between the two phases is an elliptic cone of eccentricity that depends on the relative phase

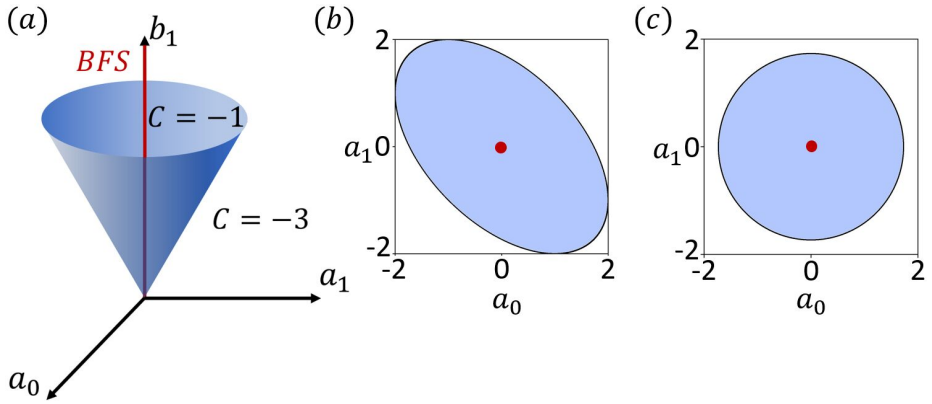

Figure 4.3: Phase diagrams for the spin-polarized Hofstadter SC at $q = 3$ in the $\hat{T}_2\hat{T}_1$ symmetric phase. **(a)** Full phase diagram in the space of a_0, a_1 and b_1, with $\vartheta = 0$. The $C = -1$ and $C = -3$ phases are separated by a conical phase boundary. On the b_1 axis, the system is gapless and has a symmetry protected Bogoliubov Fermi surface (BFS). **(b)** Cut along $b_1 = 1$ with $\vartheta = 0$. **(c)** Same as **(b)** but with $\vartheta = -\pi/6$. The phase boundary is a circle in this case.

between the p-wave components of the gap functions, $\vartheta = \mathrm{Arg}[a_0] - \mathrm{Arg}[a_1]$. In the phase diagram shown in Fig. 4.3 we therefore took

$$\Delta_0(\boldsymbol{p}) = a_0(p_x + ip_y)/p_F, \tag{4.103}$$
$$\Delta_1(\boldsymbol{p}) = -\Delta_2(-\boldsymbol{p}) = a_1 e^{i\vartheta}(p_x + ip_y)/p_F + b_1$$

with a_0, a_1 and b_1 all real, with $\vartheta = 0$ in Fig. 4.3 (b) and $\vartheta = -\pi/6$ in Fig. 4.3 (c).

As mentioned above, the spectrum is gapless along the b_1 axis, with a Fermi surface coinciding with the normal state Fermi surface. This is a simple consequence of the matrix $\hat{\Delta}$ being anti-symmetric along this axis and therefore having a zero eigenvalue, leading to an ungapped energy band. Below we will show that this Bogoliubov Fermi surface is not accidental and occurs for all odd q. It is moreover topologically protected by the combination of PHS $\mathcal{C}$ and parity symmetry $\mathcal{P}$.

While Fig. 4.3 captures the general features of the phase transitions, we note that phase transitions between higher odd Chern numbers are in principle possible with a larger even number of Dirac nodes at the phase transitions. For example, with

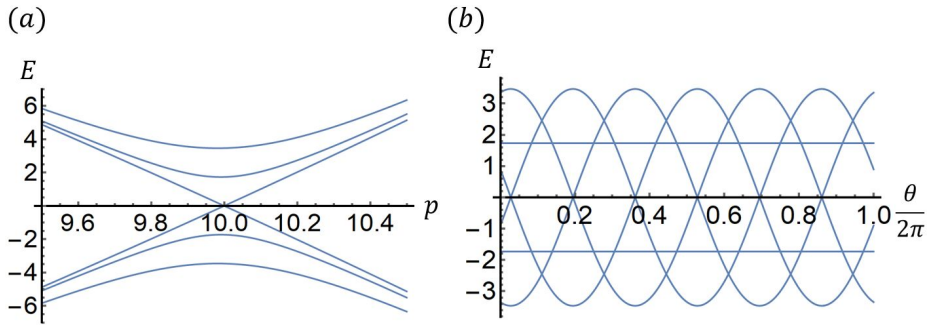

Figure 4.4: BdG spectrum for $q = 3$ with $\Delta_0(\boldsymbol{p}) = \sqrt{3}(p_x + ip_y)^3/p_F^3$, $p_F = 10$ and $\Delta_1 = -\Delta_2 = 1$. 6 Dirac nodes indicate a topological phase transition with Chern number changing from $C = -9$ to $C = -3$. **(a)** A cut of the BdG spectrum along the $\hat{p}$ direction at the Dirac node. **(b)** A cut of the BdG spectrum along the Fermi momentum $p = p_F = 10$ as a function of the angle θ of $\mathbf{p} = p_F(\cos\theta, \sin\theta)$, which shows the presence of 6 Dirac touchings. Note also the unavoided crossings at non-zero energies indicative of the presence of the MTG symmetry $\tilde{T}$.

$\Delta_0(\boldsymbol{p}) = \sqrt{3}(p_x + ip_y)^m/p_F^m$, $m \in \mathbb{Z}$ and $\Delta_1 = -\Delta_2 = 1$, the BdG spectrum has $2m$ Dirac nodes, corresponding to a phase transition between $C = -3m$ and $C = -m$ phases. Fig. 4.4 illustrates the case of $m = 3$ with six Dirac cones. We also note that the presence of the MTG symmetry $\tilde{T}$ generally results in unavoided crossings away from zero energy, as seen in Fig. 4.4 (b).

More phases and phase transitions are possible for larger q, but always with Chern numbers of the same parity as q. We illustrate this for $q = 5$ with $\Delta_0 = a_0(p_x + ip_y)/p_F, \Delta_1 = a_1(p_x + ip_y)/p_F + b_1, \Delta_2 = 0$, $\Delta_3(\mathbf{p}) = -\Delta_2(-\mathbf{p})$ and $\Delta_4(\mathbf{p}) = -\Delta_1(-\mathbf{p})$. As shown in Fig. 4.5, there are now two phase transitions as b_1 increases, with two nested conical phase boundaries. Again, there is a topologically protected BFS when $a_0 = a_1 = 0$, as we show in the next section.

4.5.3 Symmetry-Protected Bogoliubov Fermi Surfaces

Here we show that the BFS discussed in the previous section are topologically protected in the presence of the parity symmetry $\mathcal{P}$ and are a general feature of the phase diagram of $\mathbb{Z}_q$ Hofstadter SCs: for odd q a BFS is always present and pro-

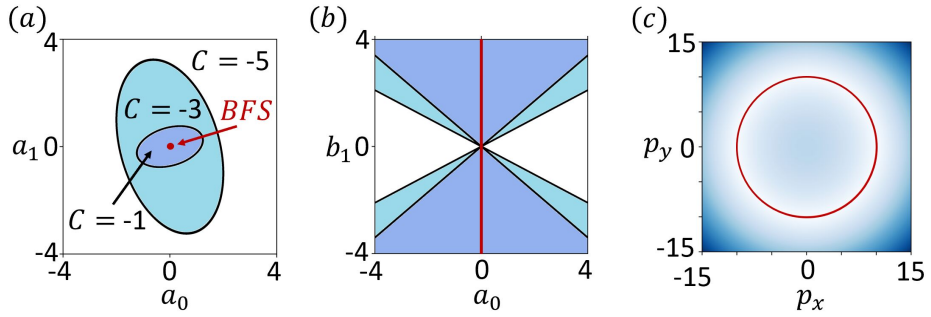

Figure 4.5: The phase diagrams for $q = 5$ with $\Delta_0 = a_0(p_x + ip_y)/p_F, \Delta_1 = a_1(p_1 + ip_2)/p_F + b_1, \Delta_2 = 0$, $\Delta_3(\mathbf{p}) = -\Delta_2(-\mathbf{p})$ and $\Delta_4(\mathbf{p}) = -\Delta_1(-\mathbf{p})$. Cuts of the nested conical phase boundaries and Bogoliubov Fermi surface are shown along **(a)** $b_1 = 1$ and **(b)** $a_1 = 0$. **(c)** Bogoliubov Fermi surface (E=0) located at $|\boldsymbol{p}| = 10$ is shown in red for $\Delta_0 = 0, \Delta_1 = 1, \Delta_2 = 0$.

tected by a topological invariant that has been established in [123]; for even q, a doubly degenerate BFS exists depending on the irrep the gap function belongs to and protected by a new topological invariant that can only be defined in the presence of MTG symmetries. The key observation is that the BFS appeared when the matrix $\hat{\Delta}$ was anti-symmetric, $\hat{\Delta}(\mathbf{p}) = -\hat{\Delta}^T(\mathbf{p})$. Since $\hat{\Delta}$ and $\hat{\Delta}^T$ have the same spectrum, this implies that their eigenvalues must appear in pairs with opposite signs. Assuming a $\mathbb{Z}_q$ symmetry, these eigenvalues are $i\Delta'_n$ with Δ'_n given in Eq. (4.95), which therefore satisfy $\Delta'_n = -\Delta'_{-n}$. For odd q this implies that $\Delta'_0 = 0$, and we conclude that two of the energy bands in Eq. (4.98) are $E_\pm = \pm|\varepsilon(\mathbf{p})|$. In particular, they cross zero energy at the Fermi momentum, forming the BFS at the original normal state Fermi surface.

For even q, note that Eq. (4.95) implies that when $\hat{\Delta}'$ is an L^{th} anti-diagonal matrix, n in Δ'_n is either an even or odd integer modulo $2q$ for L even or odd respectively. When L is odd, therefore, we conclude that in general none of the Δ'_n vanish, while for even L two of them vanish, namely Δ'_0 and Δ'_q. In the latter case the BFS is doubly degenerate and formed by four bands instead of two. As we discuss below, this implies that the BFS is topologically protected for odd q but not in general for even q. We conjecture that the doubly degenerate BFS is topologically protected for

even q and even L as long as the $\mathbb{Z}_q$ MTG symmetry is unbroken.

To establish whether the BFS is topologically protected, we need to compute the corresponding topological invariant. As discussed in Sec. 4.5.1, due to the PHS relation $\hat{\Delta}(\mathbf{p}) = -\hat{\Delta}^T(-\mathbf{p})$, $\hat{\Delta}(\mathbf{p})$ being anti-symmetric is equivalent to it being even under $\mathcal{P}$: $\hat{\Delta}(\mathbf{p}) = \hat{\Delta}(-\mathbf{p})$. It has been shown in [121] that for even parity gap functions there does indeed exist a $\mathbb{Z}_2$ topological invariant $\nu_{\mathbb{Z}_2}$ that can protect BFSs. This invariant was determined in [123] using the Pfaffian of the BdG Hamiltonian for $4N \times 4N$ BdG Hamiltonians, with the invariant being non-trivial if the Pfaffian changes sign as the BFS is crossed. As we will see, we can generalize this invariant for $2q \times 2q$ BdG Hamiltonian even when q is odd.

Note that while the Pfaffian is generally only defined for anti-symmetric matrices of even dimensions, the Pfaffian $\mathrm{Pf}[A]$ of a matrix A can be more generally defined as a polynomial in the elements of A with integer coefficients such that $\mathrm{Pf}^2[A] = \mathrm{Det}[A]$. We therefore first want to find the determinant of $\mathcal{H}_{BdG}$ which we can do by direct computation using the eigenvalues of the BdG Hamiltonian in Eq. (4.98):

$$\mathrm{Det}[\mathcal{H}_{BdG}] = (-1)^q \prod_n \left(\varepsilon^2 + |\Delta'_n|^2\right) \tag{4.104}$$

where the product is over all values of n. Notice that this is positive for even q but negative for odd q. We therefore compute the Pfaffian of $\tau^z \mathcal{H}_{BdG}$ instead of $\mathcal{H}_{BdG}$ itself, the two being equivalent for even q. τ^z is a Pauli matrix acting on the particle and hole sectors (it can be replaced with any $2q \times 2q$ matrix with integer elements and determinant equal to $(-1)^q$).

This still does not guarantee that $\mathrm{Det}[\tau^z \mathcal{H}_{BdG}]$ is a square of a polynomial, and we need to invoke the anti-symmetry of $\hat{\Delta}$. As pointed out above, when $\hat{\Delta}$ is an anti-symmetric matrix, $\Delta'_{-n} = -\Delta'_n$. Using this fact, we conclude that when $\hat{\Delta}'$ is an

L^{th} anti-diagonal matrix,

$$\mathrm{Pf}[\tau^z\mathcal{H}_{BdG}(\boldsymbol{p})] = \begin{cases} \prod_{n=0}^{q/2-1}\left(\varepsilon^2(\boldsymbol{p}) + \left|\Delta'_{2n+1}(\boldsymbol{p})\right|^2\right), & q \text{ even, } L \text{ odd} \\ \varepsilon^2(\boldsymbol{p})\prod_{n=1}^{q/2-1}\left(\varepsilon^2(\boldsymbol{p}) + |\Delta'_{2n}(\boldsymbol{p})|^2\right), & q \text{ even, } L \text{ even} \\ \varepsilon(\boldsymbol{p})\prod_{n=1}^{q/2-1}\left(\varepsilon^2(\boldsymbol{p}) + |\Delta'_{n}(\boldsymbol{p})|^2\right), & q \text{ odd} \end{cases} \tag{4.105}$$

where the product is restricted to only include one of each pair of $\Delta'_{\pm n}(\boldsymbol{p})$. As $\varepsilon^2(\boldsymbol{p}) + |\Delta'_n(\boldsymbol{p})|^2$ are positive-definite quantities, we conclude that the Pfaffian does not change sign when q is even, but necessarily changes sign at the BFS for odd q because $\varepsilon(\boldsymbol{p})$ does. The $\mathbb{Z}_2$ topological invariant can be defined as

$$\nu_{\mathbb{Z}_2} = \{\mathrm{Pf}\left[\tau^z\mathcal{H}_{BdG}(\mathbf{p}_+)\right]\mathrm{Pf}\left[\tau^z\mathcal{H}_{BdG}(\mathbf{p}_-)\right]\} \tag{4.106}$$

where $\boldsymbol{p}_+$ ($\boldsymbol{p}_-$) is any momentum inside (outside) of the BFS; this coincides with the definition in [123] for even q. The invariant is trivial when it is equal to 1 and non-trivial when it is equal to -1, i.e. when the Pfaffian changes sign across the BFS. The topological invariant is therefore trivial for even q but non-trivial for odd q, and so the BFS is topologically protected in the latter case.

Note that while we made use of the MTG $\mathbb{Z}_q$ symmetry in the proof of the existence of the BFS for odd q, since the stability of the BFS relies only on PHS and parity symmetry [121, 122], the BFS established for odd q remains perturbatively stable if MTG is broken as long $\hat{\Delta}(\mathbf{p})$ is an even function of $\mathbf{p}$. However, in the presence of the MTG symmetry we can simplify the invariant by noting that only the $n = 0$ block of the BdG Hamiltonian contributes to the sign change of the Pfaffian. Instead of using the Pfaffian of the whole BdG Hamiltonian we can therefore use the Pfaffian of $\mathcal{H}_{BdG,0}$ in Eq. (4.97). Note incidentally that the Pfaffian of a direct sum of two matrices is a product of the Pfaffians of the two matrices: $\mathrm{Pf}[A \oplus B] = \mathrm{Pf}[A]\mathrm{Pf}[B]$,

assuming the RHS exists. Since

$$\mathrm{Det}\left[\tau^z \mathcal{H}_{BdG,0}\right] = -\mathrm{Det}\left[\begin{pmatrix} \varepsilon & 0 \\ 0 & -\varepsilon \end{pmatrix}\right] = \varepsilon^2\,, \tag{4.107}$$

the Pfaffian is $\mathrm{Pf}\left[\tau^z \mathcal{H}_{BdG,0}\right] = \varepsilon$. We can therefore instead define a $\mathbb{Z}_2$ invariant

$$\nu_{\mathbb{Z}_2,0} = \left\{\mathrm{Pf}\left[(\tau^z \mathcal{H}_{BdG,0}(\boldsymbol{p}_+)\right] \mathrm{Pf}\left[\tau^z \mathcal{H}_{BdG,0}(\boldsymbol{p}_-)\right]\right\} \tag{4.108}$$

While for odd q we simply have $\nu_{\mathbb{Z}_2,0} = \nu_{\mathbb{Z}_2}$, we note that interestingly we can also define $\nu_{\mathbb{Z}_2,0}$ for even q assuming that L is even. In that case we can also analogously define $\nu_{\mathbb{Z}_2,q}$ indicating a sign change of $\mathrm{Pf}\left[\tau^z \mathcal{H}_{BdG,q}\right] = \varepsilon$. We then have $\nu_{\mathbb{Z}_2} = \nu_{\mathbb{Z}_2,0}\nu_{\mathbb{Z}_2,q}$ is trivial, while the new invariant $\nu_{\mathbb{Z}_2,0}$ is not, indicating the presence of a doubly degenerate BFS.

Importantly, $\nu_{\mathbb{Z}_2,0}$ exists for even q only when L is even, and can only be defined in the presence of the $\mathbb{Z}_q$ MTG symmetry in addition to PHS and parity $\mathcal{P}$, unlike $\nu_{\mathbb{Z}_2}$. Recall that when the $\mathbb{Z}_q$ symmetry is $\hat{T}(\theta_0) = \hat{T}_2^N \hat{T}_1$ with $\theta_0 = \frac{2\pi p}{q} M$, $L = N - M$ modulo q and note that $\hat{T}(\theta_0)$ commutes or anti-commutes with $\hat{T}_1^{q/2}(0)$ when L is even or odd. Recall also that gap functions are even or odd under $\hat{T}_1^{q/2}(0)$ for even and odd M respectively and belong to different irreps of the MTG, as we showed in Sec. 4.3.2. The parity of N, on the other hand, determines whether the $\mathbb{Z}_q$ symmetry $\hat{T}(\theta_0)$ commutes or anti-commute with $\hat{T}_1^{q/2}(0)$. We therefore conclude that for even q, $\nu_{\mathbb{Z}_2,0}$ is a new topological invariant protected by the combination of PHS, parity $\mathcal{P}$, and $\mathbb{Z}_q$ symmetries when M and N have the same parity. We note the similarity of the definition of $\nu_{\mathbb{Z}_2,0}$ to that of topological invariants of crystalline SPT phases defined by similarly simultaneously block-diagonalizing the Hamiltonian and the crystalline symmetry [261, 262]. Our result therefore shows that Hamiltonians with MTG symmetries require a new classification of their topological invariants.

4.6 Summary and Discussion

The main contributions presented in this chapter are:

- We have provided a detailed analysis of the properties of electrons undergoing pairing instabilities in time-reversal broken Hofstadter bands, which characterize the spectrum of single particle states in 2D lattices with magnetic flux $\Phi = (p/q)\Phi_0$ per unit cell. Our approach focused on exploring the consequences of the magnetic translation symmetries on the paired state.

- We have established the classification of the irreducible representations of the magnetic translation group furnished by the pairing matrix $\hat{\Delta}$, which we showed to have different properties from the familiar irreps furnished by single particle Bloch states. Furthermore, the group theory analysis shows that at least one magnetic translation symmetry is *necessarily* broken in the paired state, and we find numerically that all of them can be broken at least for $q \geq 5$.

- Building on the properties of the irreps of the magnetic translation group, we have formulated an effective Ginzburg-Landau theory to study the thermodynamic properties of Hofstadter superconductors at general fluxes $\Phi = (p/q)\Phi_0$ with rational p/q. The theory is constructed in terms of a complex valued vector order parameter $\boldsymbol{\eta}$ of dimension q ($q/2$) for odd (even) q.

- We found that the multi-component nature of the order parameter yields a rich phase diagram characterized by different symmetry breaking patterns of the magnetic translation group, which can be interpreted as distinct classes of "vortex lattices." In particular, we have identified an important class of thermodynamic phases that corresponds to $\mathbb{Z}_q$-symmetric Hofstadter superconductors, in which the magnetic translation group breaks down to a $\mathbb{Z}_q$ subgroup resulting in $q/2$- or q-fold degenerate ground states for even and odd q, respectively, with

the degeneracy equal to the dimension of the irreps.

- We have shown that chiral $\mathbb{Z}_q$-symmetric Hofstadter superconductors provide a natural setting for the realization of topological superconductivity with tunable Chern numbers. In particular, we have established that when pairing only involves electrons in a single Hofstadter band, Hofstadter superconductors can realize SPT phases protected by magnetic translation symmetries where the parity of the Chern numbers is the same as the parity of q. This property establishes that Hofstadter superconductors with a fully gapped spectrum fall into two topological classes according to the parity of q; i.e., they support non-Abelian (Abelian) excitations for odd (even) q.

- We have shown that when the Hofstadter superconductor additionally possesses parity symmetry, its spectrum *necessarily* supports Bogoliubov Fermi surfaces (BFS) for odd q, even when the $\mathbb{Z}_q$ symmetry is broken by the order parameter as the associated topological invariant defined in [123] does not require it. For even q, in contrast, parity alone cannot protect the BFSs, which are necessarily doubly degenerate if they exist. However, we also showed that this doubly degenerate BFS can be protected by the $\mathbb{Z}_q$ MTG symmetry in cases when a new topological invariant, given in Eq. (4.108), can be defined. This illustrates the fact that a new topological classification is required for $\mathbb{Z}_q$-symmetric Hofstadter superconductors.

Our work in this chapter raises a number of interesting questions that deserve future attention:

- First, it would be desirable to find direct connections between the phenomenological Ginzburg-Landau theory established on symmetry grounds and microscopic models describing moiré superlattices subject to a perpendicular magnetic field [270–273], with the purpose of shedding light on realistic parameter

regimes conducive to the realization of electronic pairing in moiré Hofstadter bands [1, 2, 45, 47–49, 109].

- Second, given that the ground states we find have a large degeneracy of order q, in a real system it is natural to expect domain formation. The study of such domains requires considering gradient terms in the Ginzburg-Landau free energy in Eq. (4.46) that we have ignored in this chapter. Additionally, other spatial defects (of the order parameter and/or of the underlying lattice) such as dislocations and disclinations are possible. It could therefore be fruitful to study the nature of low energy excitations of Hofstadter superconductors in the presence of such defects to seek possible realizations of defect-bound Majorana fermions [274, 275]. The study of these lattice defects may also shed light on the meaning of "gauging" the magnetic translation group, similar to the approach of gauging internal [276] and spatial symmetries [277].

- Another potentially rich scenario could be explored by studying interfaces of Hofstadter superconductors, where different Majorana backscattering may lead to 1D SPT interfaces [278–281] supporting non-Abelian domain walls [282–291].

- Furthermore, the presence of a multi-component order parameter characterizing Hofstadter superconductors with phases relations fixed by the magnetic translation group suggests the possibility that this system may support interesting classes of Leggett modes [292]. In the context of pair density waves (PDW), multi-component pairing order parameters are also known to lead to fractional vortices [221, 228, 244, 293–295], as well as induced or vestigial orders like charge density waves or charge 4e condensates [137, 197, 228, 245, 296–304]. This raises the question of what such phenomena may look like in Hofstadter SCs, for example whether vortices trapping a $1/q$ fraction of the flux quantum may be possible [221, 297, 305, 306]. Note that charge 4e, 6e and higher charge

Q orders would be classified by irreps of the MTG beyond those considered here, with irrep dimensions given by the greatest common divisor $\gcd(q, Q)$ [220].

Chapter 5

Competing Orders in Hofstadter Quantum Materials

5.1 Overview

In chapter 4, we have provided a classification of Hofstadter superconductors with a phenomenological framework, without addressing the microscopic mechanism responsible for pairing of electrons. Recently, experimental evidence found in moiré systems points to electronic interactions playing key role in accounting for a plethora of new phases of matter[41, 44, 87, 99, 103, 104, 106, 196, 233, 273, 307–309]. It is thus pertinent to ask whether superconducting condensate of paired electrons can form in Hofstadter systems with electronic repulsion, similar to the proposed mechanisms of unconventional superconductivity in correlated materials[79, 193–197] such as high-temperature superconductors[134, 136, 138, 198], and in contrast to conventional superconductivity caused by phonon mediated electronic attraction[8, 192, 310]. In this chapter, we addresses this important question by providing a microscopic mechanism explaining the origin of Hofstadter superconductivity[61] that relies solely on electronic interactions and nontrivial properties of Hofstadter bands.

It has long been suggested that, contrary to the conventional view, superconductivity(SC) can reemerge in Landau levels in the presence of strong magnetic fields, provided that there are attractive interactions between electrons[151]. More recently, it has been proposed theoretically that such reentrant SC can theoretically occur in magic angle twisted bilayer graphene (TBG) [307]. TBG and other 2D moiré superlattices are particularly attractive for realizing reentrant SC as they can host SC at zero magnetic field at low density carrier regimes [308], such that only relatively modest magnetic fields are required to achieve the quantum limit of Landau levels. However, several challenges have stood in the way of observing reentrant SC in experiment, among them the role of repulsive interactions that make quantum Hall states natural competitors of such reentrant SC in Landau levels.

In this chapter we propose that this issue can be circumvented in Hofstadter bands that unlike Landau levels have a finite bandwidth W [4, 90], allowing a weak-coupling renormalization group (RG) treatment of repulsive electronic interactions. This is especially relevant for moiré systems since their nanometer scale unit cells enable the realization of Hofstadter bands in experimentally accessible magnetic fields at which the magnetic flux per super unit cell $\Phi = BA_{\text{uc}}$ is comparable to the flux quantum $\Phi_0 = 2\pi\hbar/e = 2\pi$ in natural units [1, 2, 45–49]. Beyond the rich phenomena in Hofstadter-Chern insulators [60, 94–107], a recent classification [61] has shown that Hofstadter bands may support novel Hofstadter superconductors (HSC) characterized by spontaneous breaking of the magnetic translation group (MTG) symmetries [91–93], leading to multi-component finite momentum Cooper pairing similar to pair-density wave states [228]. HSCs embody a new form of reentrant superconductivity in Hofstadter bands, in which the large flux per unit cell makes the magnetic length comparable to the lattice scale, thus generalizing the Landau level reentrant SC state.

Though pairing in Hofstadter bands has been studied earlier using mean-field calculations with phenomenological attractive interactions [62–68], no microscopic mech-

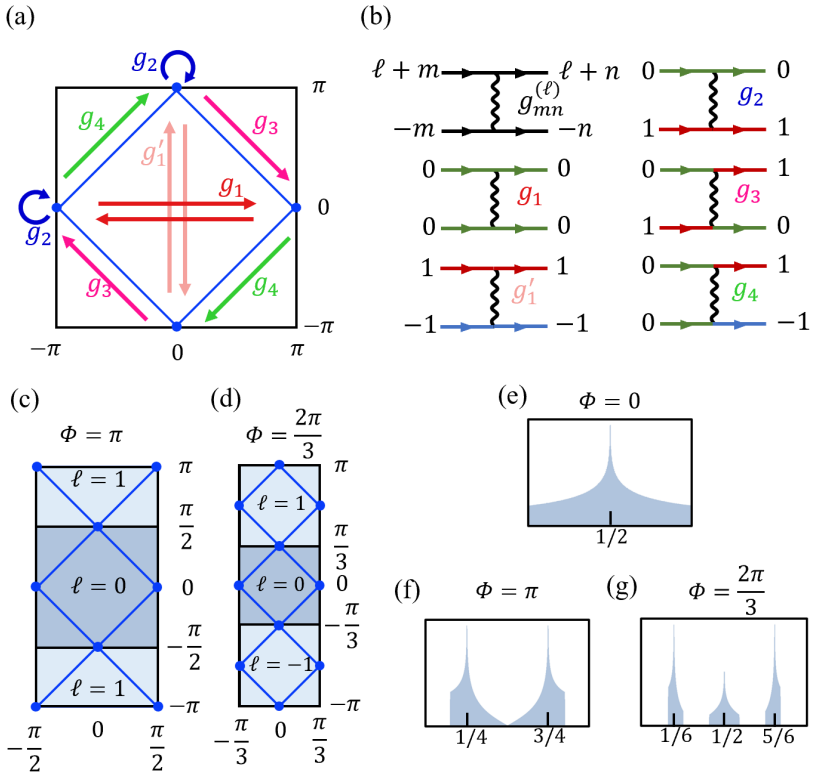

Figure 5.1: Van Hove singularities in the square Hofstadter model at **(a)** zero, **(c)** π, and **(d)** $2\pi/3$ flux, and **(e-g)** the corresponding peaks in the density of states at indicated fillings. Due to the MTG symmetry, the magnetic Brillouin zone (MBZ) splits into q (energy degenerate) reduced magnetic Brillouin zones (rMBZ) labeled with $\ell = 0, \ldots, q-1$. In each band there are a total of $2q$ VHSs occurring at momenta $\mathbf{K}_{\ell,\mathrm{v}} = \left((1+\mathrm{v})\frac{\pi}{q}, (\mathrm{v}+2p\ell)\frac{\pi}{q}\right)$, such that there is a pair of VHSs in each rMBZ labelled with a VHS index $\mathrm{v} = 0, \pm 1$, with the identification of VHS $\ell, 1$ and $\ell+1, -1$. Colored arrows in **(a)** and the Feynman diagrams in **(b)** show the types of interaction processes considered in the RG analysis: intra-VHS processes g_1 and $g_{1'}$ (red and light red); inter-VHS forward scattering g_2 (blue); exchange g_3 (magenta); and pair-hopping g_4. Green, red, and blue propagator arrows correspond to $\mathrm{v} = 0, 1, -1$ respectively, and the black diagram show the additional rMBZ indices $\ell, m, n = 0, \ldots, q-1$ carried by the coupling constants $g_{mn}^{(\ell)}$, ℓ denoting the total momentum of the interacting pair.

anism leading to this attraction has so far been proposed. Here we show that HSCs can arise from repulsive interactions due to the competition of electronic orders near Van Hove singularities (VHS) that provide a logarithmic enhancement of the density of states (DOS) [73]. Such a scenario of competing orders near VHSs underlies several proposed mechanisms of unconventional superconductivity through repulsive interactions, for example in cuprates [74–76], doped graphene [77–80] and moiré graphene superlattices [81–89]. Furthermore, we go beyond mean-field by using an RG analysis [142–144], extending it to the new realm of Hofstadter electronic bands and uncovering a new pathway to realize reentrant superconductivity in moiré superlattices. In addition, our approach allows us to treat the interplay of all logarithmically divergent instabilities on equal footing, and thus to additionally study the competition of superconductivity with charge/spin density wave (CDW/SDW) orders. The RG analysis thus also goes beyond earlier mean-field studies of CDW and SDW in Hofstadter systems in [69] and [70, 71] respectively, and furthermore provides an alternative scenario to fractionalization in Hofstadter bands [17, 72, 117, 119, 273, 311–315].

As a proof of principle, we work with the repulsive Hofstadter-Hubbard (HH) model on the square lattice with onsite interaction $U > 0$ and flux $\Phi = 2\pi p/q$ that is a rational multiple of the flux quantum. Importantly, we focus on the regime $q \sim 1$ in which the Hofstadter bands have a bandwidth W comparable to that of the original band at zero field, which allows us to investigate electronic instabilities in a controlled weak coupling regime $U/W \ll 1$. While a hexagonal lattice would better approximate twisted bilayer graphene, which is the best studied superconducting moiré system, we establish our results on the square lattice since it still allows us to capture the essential correlation effects in Hofstadter bands while working with a simpler band structure, as shown in Sec.5.2. Nevertheless, we stress that while the competition of electronic orders and their resulting instabilities can depend on the underlying lattice and interactions, the weak coupling RG framework developed

here is of general applicability, and thus represents an important step towards the investigation of electronic instabilities in a wider class of two dimensional Hofstadter superlattices, including moiré graphene.

Additionally, the square HH model can more easily be realized in cold atom systems [135, 316–322], though the focus in that field has been on bosonic [55, 221, 323–326] and time-reversal invariant fermionic [235–237, 327–329] HH models (note that the latter coincides with the regular fermionic Hofstadter-Hubbard model at $q = 2$, i.e. at π-flux). In addition, more recently single layer cuprates exhibiting critical temperatures close to their bulk values have been fabricated [140], opening an avenue for realizing twisted cuprate moiré systems with square lattices for which our model may be directly applicable. Such twisted heterostructures have recently been studied theoretically [139, 330–333], with few-layer twisted interfaces already realized in experiment [334, 335]. It remains to be seen whether Hofstadter physics can be realized in twisted cuprates, but, if it is, a reentrant HSC phase may be possible in this system.

The MTG symmetries play a key role in our analysis. In particular, they imply the presence of $2q$ VHSs per Hofstadter band, as shown in Fig. 5.1. The magnetic flux $\Phi = 2\pi p/q$ thus acts as a knob controlling the number of VHSs in the system, which completely alters the RG flow and thus the possible instabilities of the system. This is well illustrated by the two distinct reentrant HSC phases that we find at π-flux (i.e. $q = 2$) and at $2\pi/3$-flux ($q = 3$). For the former case, we identify a nodal SC phase that respects all MTG symmetries as the winning RG instability at 1/4 and 3/4 lattice filling, even with perfect nesting in the competing SDW channel that is degenerate with the SC channel in the absence of the magnetic field [157]. For $q = 3$, we find that, at 1/6 and 5/6 lattice filling, SC and SDW are nearly degenerate when both are at perfect nesting, while CDW is favored at half-filling. A small symmetry-allowed detuning from perfect nesting in the SDW therefore favors

the pairing instability, which necessarily breaks a subset of the MTG symmetries [61]. We find that the resulting SC state is a fully gapped chiral topological phase with Chern number $\mathcal{C} = \pm 6$ that preserves a $\mathbb{Z}_q$ subgroup of the MTG. Surprisingly, this phase also possesses an emergent self-similarity symmetry due to the RG flow approaching a special self-similar fixed trajectory that exists as another consequence of the MTG symmetries. We identify this self-similar fixed trajectory for all q, implying that long-range self-similar HSC states can be competing instabilities at flux values beyond those studied numerically in this chapter.

The main results presented in this chapter are:

- We perform a weak coupling renormalization group (RG) analysis for the electron ordering of the Hofstadter-Hubbard model on a square lattice, which establishes a rich competition of electronic orders, from which electronic pairing emerges as a low energy instability.

- We find that some of the RG fixed points are characterized by an emergent self-similarity, which reflects the non-trivial renormalization of the bare Hubbard interaction in fractal Hofstadter bands.

- We predict for the repulsive Hubbard-Hofstadter model the existence of (i) nodal d-wave superconductivity near 1/4 and 3/4 fillings in the π-flux lattice ($\Phi = h/2e$); (ii) chiral topological superconductivity with Chern number $\mathcal{C} = \pm 6$ near 1/6 and 5/6 fillings in the $\pm 2\pi/3$-flux lattice ($\Phi = \pm h/3e$). The latter arises when the interactions flow to a self-similar fixed trajectory of the RG flow and are characterized by a self-similarity symmetry that enforces a polynomially decaying real space order parameter.

These results open a new route in the pursuit of reentrant superconductivity in a wide class of Hofstadter quantum materials including synthetic lattices and moiré heterostructures.

The rest of this chapter is organized as follows. In Sec. 5.2 we review the square lattice fermionic HH model and its symmetries, and present the VHS patch model with dispersions and interactions expanded around the VHS points at which the DOS diverges. In Sec. 5.3, we establish the symmetry of the HSC by presenting the mean field theory. We then analyse the repulsive Hubbard-Hofstadter model using RG in Sec. 5.4. We first study the flow of the coupling constants, identifying a self-similar fixed trajectory, and then analyse the flow of test vertices and corresponding susceptibilities in order to identify the leading instabilities of the system. In Sec. 5.5, We present a simple method based on symmetry argument that extended the gap functions to the full BZ. We then study the topology of the $q = 3$ HSC by computing the edge modes.

5.2 Model

In this section, we present the fermionic HH model with repulsive interaction on the square lattice. We establish the form of the projected interaction at the q-fold VHSs that will be used in the RG analysis.

We consider the nearest neighbor square lattice repulsive HH Hamiltonian

$$\begin{aligned} H = &- \sum_{\langle \mathbf{r}\mathbf{r}'\rangle\sigma} t\, e^{2\pi i A_{\mathbf{r}\mathbf{r}'}} c^\dagger_{\mathbf{r}\sigma} c_{\mathbf{r}'\sigma} + h.c. - \mu \sum_{\mathbf{r}\sigma} c^\dagger_{\mathbf{r}\sigma} c_{\mathbf{r}\sigma} \\ &+ U \sum_{\mathbf{r}} n_{\mathbf{r}\uparrow}\, n_{\mathbf{r}\downarrow} = H_0 + H_{\text{int}}\,, \end{aligned} \tag{5.1}$$

with $U > 0$ where μ is the chemical potential, $n_{\boldsymbol{r}\sigma}$ is the number operator with spin $\sigma = \uparrow, \downarrow$ at site $\mathbf{r} = (x, y) \in \mathbb{Z}^2$, and $A_{\mathbf{r}\mathbf{r}'} = \int_{\mathbf{r}}^{\mathbf{r}'} \mathbf{A} \cdot d\mathbf{r}/\Phi_0 = \frac{p}{q} x(1 - \delta_{yy'})$ corresponding to a flux per unit cell $\Phi = 2\pi p/q$ that is a rational multiple of the flux quantum Φ_0. We work in the Landau gauge with vector potential $\mathbf{A} = xB\hat{y}$ and set the lattice constant $a = 1$. Note that while time-reversal symmetry (TRS) is broken by the

orbital effect, we neglect the Zeeman splitting in our analysis and retain the full SU(2) spin rotation symmetry, implying that our weak coupling analysis in applicable in the regime $E_Z < \Delta \ll W$, where E_Z is the Zeeman splitting and Δ is the characteristic energy scale of the electron instabilities. The interesting regime of spin polarized Hofstadter bands case merits a separate discussion which is outside the scope of this chapter.

In addition to TRS, the vector potential breaks the translation symmetry T_x along the x direction. However, the *magnetic* translation $\hat{T}_x = T_x e^{2\pi i a B y/\Phi_0}$ remains a symmetry of the Hamiltonian. $\hat{T}_x$ and the unbroken translation $T_y = \hat{T}_y$ along the y direction generate the non-Abelian magnetic translation group (MTG) satisfying $\hat{T}_x\hat{T}_y = \omega_q^p \hat{T}_y\hat{T}_x$ with $\omega_q = e^{2\pi i/q}$ being the q^{th} root of unity. Point group symmetries of the original Hamiltonian in the absence of the magnetic field similarly give rise to their magnetic versions with appropriate gauge transformations of the vector potential. For example, the original C_4 symmetry becomes $\hat{C}_4 = C_4 e^{-2\pi i x y B/\Phi_0}$, where the additional gauge transformation rotates $\mathbf{A} = xB\hat{\mathbf{y}} \to yB\hat{\mathbf{x}}$. The $\hat{C}_4$ symmetry will play a role below when we consider the instabilities of the π-flux Hofstadter Hamiltonian.

The commutation relations imply that $\hat{T}_x^q$ and $\hat{T}_y$ commute with each other and the Hamiltonian, effectively enlarging the unit cell along the x direction. We correspondingly define operators $c_{\mathbf{R},s,\sigma} = c_{s\hat{\mathbf{x}}+\mathbf{R},\sigma}$ with $s = 0, \ldots, q-1$ being the sub-lattice index defined modulo q and $\mathbf{R} = (qj, y)$ with $j, y \in \mathbb{Z}$ labeling the extended unit lattice cites. Bloch's theorem then applies to these operators and we can write the Hofstadter Hamiltonian H_0 in momentum space using $c_{\mathbf{k}s\sigma} = \frac{1}{\sqrt{N}} \sum_{\mathbf{R}} e^{-i\mathbf{k}\cdot(s\hat{\mathbf{x}}+\mathbf{R})} c_{s\hat{\mathbf{x}}+\mathbf{R},\sigma}$, with N being the total number of unit cells and where the quasi-momentum $\mathbf{k}$ is defined on the folded *magnetic* Brillouin zone (MBZ) $\mathbf{k} = (k_x, k_y) \in [-\pi/q, \pi/q) \times [-\pi, \pi)$. In this basis

$$H_0 = -\sum_{\mathbf{k}s} (2t\cos(k_y + sQ) + \mu) c^\dagger_{\mathbf{k}s\sigma} c_{\mathbf{k}s\sigma} - \sum_{\mathbf{k}\langle ss'\rangle} t e^{-ik_x(s-s')} c^\dagger_{\mathbf{k}s\sigma} c_{\mathbf{k}s'\sigma} \,, \tag{5.2}$$

and the magnetic translation symmetries act as $\hat{T}_x c_{\mathbf{k}s\sigma}\hat{T}_x^\dagger = e^{-ik_x}c_{\mathbf{k}+\mathbf{Q},s+1,\sigma}$ and $\hat{T}_y c_{\mathbf{k}s\sigma}\hat{T}_y^\dagger = e^{-ik_y}c_{\mathbf{k}s\sigma}$, with $\mathbf{Q} = \frac{2\pi p}{q}\hat{\mathbf{y}}$. The Hofstadter Hamiltonian H_0 can then be diagonalized as $H_0 = \sum_{\mathbf{k}\alpha\sigma}\varepsilon_\alpha(\mathbf{k})d^\dagger_{\mathbf{k}\alpha\sigma}d_{\mathbf{k}\alpha\sigma}$ using a unitary transformation

$$d_{\mathbf{k}\alpha\sigma} = \sum_s \mathcal{U}^s_\alpha(\mathbf{k})c_{\mathbf{k}s}\,. \tag{5.3}$$

Note that there is a large freedom in choosing the U(1) phases in $\mathcal{U}^s_\alpha(\mathbf{k})$. For concreteness, we take $\mathcal{U}^{s+1}_\alpha(\mathbf{k}+\mathbf{Q}) = \mathcal{U}^s_\alpha(\mathbf{k})$, which endures a canonical transformation under MTG for the band operators: $\hat{T}_x d_{\mathbf{k}\alpha\sigma}\hat{T}_x^\dagger = e^{-ik_x}d_{\mathbf{k}+\mathbf{Q},\alpha,\sigma}$ and $\hat{T}_y d_{\mathbf{k}\alpha\sigma}\hat{T}_y^\dagger = e^{-ik_y}d_{\mathbf{k}\alpha\sigma}$. Furthermore, we fix the remaining gauge freedom by taking $\mathcal{U}^1_\alpha(\mathbf{k}) \in \mathbb{R}$. This choice makes it clear that the $\hat{T}_x$ symmetry implies a q-fold degeneracy of each band, $\varepsilon_\alpha(\mathbf{k}) = \varepsilon_\alpha(\mathbf{k}+\mathbf{Q})$. This means we can further restrict the quasi-momentum to a *reduced* magnetic Brillouin zone (rMBZ) $\mathbf{p} = (p_x, p_y) \in [-\pi/q, \pi/q)^2$ and define $d_{\mathbf{p}\ell\alpha\sigma} = d_{\mathbf{p}+\ell\mathbf{Q},\alpha\sigma}$ where $\ell = 0, \ldots, q-1$ is the magnetic patch index defined modulo q as defined in [61] (see Fig. 5.1 (c-d)). We also refer to ℓ as the rMBZ magnetic flavor index to distinguish it from the VHS indices introduced below.

VHS Patch Model and Projected Interactions

Unlike earlier mean-field analyses of the fermionic HH model [62–65, 67, 69–71], here we investigate the instabilities driven by *repulsive* on-site interactions due to diverging DOS at the VHSs. In the square lattice Hofstadter model, the VHSs occur at electron fillings that are odd multiples of $1/(2q)$ (counting spin), i.e. in half-filled Hofstadter bands. In each band there are a total of $2q$ VHSs occurring at momenta $\mathbf{K}_{\ell,\mathrm{v}} = \left((1+\mathrm{v})\frac{\pi}{q}, \mathrm{v}\frac{\pi}{q}\right) + \ell\mathbf{Q}$ which we label with the VHS index $\mathrm{v} = 0, 1$ [336]. Note that the VHSs thus lie at the images of the original VHSs of the square lattice at zero flux under a rescaling of the momentum by $1/q$, which is a consequence of the self-similarity property of the Hofstadter spectrum [60, 337] that also implies that the

Fermi surfaces are composed of q touching squares for any Hofstadter band (see Fig. 5.1 (a), (c-d)).

Within this weak-coupling framework we can project the interactions onto the Fermi surfaces formed by a single band α, neglecting all other bands and expand the dispersions around patches centered at the VHS momenta $\mathbf{K}_{\ell,\mathrm{v}}$, obtaining a VHS patch model that we will analyse in in Sec. 5.4 using fermionic RG [74, 75, 77, 144]. We thus define the patch model operators $d_{\mathbf{p}\ell\mathrm{v}\alpha\sigma} = d_{\mathbf{p}+\mathbf{K}_{\ell,\mathrm{v}},\alpha,\sigma}$ with $\mathbf{p}$ a small momentum expanded around a patch centered at $\mathbf{K}_{\ell,\mathrm{v}}$. For bookkeeping purposes, we include a redundancy in our description and allow $\mathrm{v} = -1$ with the identification $\mathbf{K}_{\ell,-1} \equiv \mathbf{K}_{\ell-1,1}$ which makes the VHS and magnetic flavor indices conserved quantities in Feynman diagrams we use in the RG analysis.

We then project H_{int} in Eq. (5.1) onto the patches obtaining an effective interaction Hamiltonian

$$H_{int} \to H_{int}^{(\alpha)} = \frac{1}{2} \sum_{\substack{\ell mn \\ \mathrm{uvw},\sigma\sigma'}} g^{(\alpha;\ell,\mathrm{u})}_{m,\mathrm{v};n,\mathrm{w}} d^\dagger_{\ell+n,\mathrm{u+w},\alpha,\sigma} d^\dagger_{-n,-\mathrm{w},\alpha,\sigma'} d_{-m,-\mathrm{v},\alpha,\sigma'} d_{\ell+m,\mathrm{u+v},\alpha,\sigma} \,, \quad (5.4)$$

where $\ell, m, n = 0, \dots q-1$ are magnetic flavor indices, $\mathrm{u}, \mathrm{v}, \mathrm{w} = 0, \pm 1$ are the VHS indices, and

$$g^{(\alpha;\ell,\mathrm{u})}_{m,\mathrm{v};n,\mathrm{w}} = U \sum_s \mathcal{U}^s_\alpha\left(\mathbf{K}_{\ell+n,\mathrm{u+w}}\right) \mathcal{U}^s_\alpha\left(\mathbf{K}_{-n,-\mathrm{w}}\right) \mathcal{U}^{s*}_\alpha\left(\mathbf{K}_{-m,-\mathrm{v}}\right) \mathcal{U}^{s*}_\alpha\left(\mathbf{K}_{\ell+m,\mathrm{v}}\right) \quad (5.5)$$

are the coupling constants corresponding to interactions between electrons with total momenta $\mathrm{u}(\pi,\pi)/q + \ell\mathbf{Q}$, dressed by form factors originating from the unitary transformation Eq. (5.3). Henceforth we will consider a fixed band α and drop the index where it is clear from context.

As there are $2q$ VHSs, the number of coupling constants grows quickly with q, which manifests the MTG action in momentum space. Taking hermiticity, MTG

symmetries, and redundancy of the VHS indices into account, there are a total of $\mathcal{O}(q^2)$ independent coupling constants that can be classified into five processes according to their VHS indices:

$$\begin{aligned} g_{mn}^{(\ell)1} &= g_{m,0;n,0}^{(\ell,0)} & g_{mn}^{(\ell)1'} &= g_{m,1;n,1}^{(\ell,0)} \\ g_{mn}^{(\ell)2} &= g_{m,0;n,0}^{(\ell,1)} & g_{mn}^{(\ell)3} &= g_{m,0;n,-1}^{(\ell,1)} \\ g_{mn}^{(\ell)4} &= g_{m,0;n,1}^{(\ell,0)} \end{aligned} \tag{5.6}$$

as shown in Fig. 5.1 (b). g_1 and $g_{1'}$ correspond to intra-patch processes for $\mathrm{v} = 0, \pm 1$ VHSs respectively, g_2 (g_3) is an inter-patch process without (with) exchange, and g_4 is a pair-hopping process. Note that in the absence of TRS, not all coupling constants are necessarily real. In addition to relations imposed by hermiticity, the coupling constants also satisfy $g_{mn}^{(\ell)j} = g_{m-1,n-1}^{(\ell+2),j}$ as a consequence of the MTG action on the fermion operators $\hat{T}_x d_{\mathbf{p}\ell\mathrm{v}\sigma}\hat{T}_x^\dagger = e^{-ip_x} d_{\mathbf{p},\ell+1,\mathrm{v}\sigma}$. In particular, for odd q all coupling constants can be expressed in terms of $g_{mn}^{(0)j}$. For even q, all coupling constants can be expressed in terms of either $g_{mn}^{(0)j}$ or $g_{mn}^{(1)j}$, with an additional relation $g_{mn}^{(\ell)j} = g_{m-q/2,n-q/2}^{(\ell)j}$. By virtue of the MTG symmetries the coupling constants Eq.(5.6) thus organize into processes that resemble those in zero magnetic field. As we will see in Sec. 5.4, this has the important implication that the RG equations exhibit a degree of self-similarity.

5.3 Mean Field Analysis

In this section, we present the mean-field theory of HSC using the standard Bogoliubov-De Gennes (BdG) formalism to establish the symmetry of the HSC for $q \neq 1$. For a detailed discussion, see Chapter 4 or [61].

5.3.1 Mean Field Hamiltonian

We start with the mean field Hamiltonian, which in the band basis reads

$$H = \sum_{\ell,\alpha,\mathbf{p}} \varepsilon_\alpha(\mathbf{p}) d^\dagger_{\mathbf{p},\ell,\alpha} d_{\mathbf{p},\ell,\alpha} + \frac{1}{2} \sum_{m,n,\alpha,\beta,\mathbf{p}} \left[\hat{\Delta}_{\ell,\alpha;\ell'\beta}(\mathbf{p}) d^\dagger_{\mathbf{p},\ell,\alpha} d^\dagger_{-\mathbf{p},\ell',\beta} + h.c. \right] + H_{\Delta^2} \quad (5.7)$$

where $\alpha, \beta = 0, \ldots, q-1$ are the Hofstadter band indices, ℓ, ℓ' are the magnetic patch indices (we omit the spin index), and

$$H_{\Delta^2} = \sum_{\ell,n,m,\mathbf{p},\mathbf{p}'} \hat{\Delta}^\dagger_{\ell+m,-m}(\mathbf{p}) \left[g^{-1}(\mathbf{p};\mathbf{p}') \right]^{(\ell)}_{mn} \hat{\Delta}_{\ell+n,-n}(\mathbf{p}') \quad (5.8)$$

is a term quadratic in the gap function arising from the Hubbard-Stratonovich transformation and involving the inverse of the coupling tensor:

$$\sum_{o\mathbf{q}} g^{(\ell)}_{mo}(\mathbf{p};\mathbf{q}) \left[g^{-1}(\mathbf{q};\mathbf{p}') \right]^{(\ell')}_{on} = \delta_{\ell,\ell'} \delta_{mn} \delta_{\mathbf{p}\mathbf{p}'} \,. \quad (5.9)$$

Here we omitted the band indices in the interactions for simplicity as in the weak-coupling approximation we assume only interactions within a single band play a role and inter-band interaction will not play a role below. In the BdG formalism we introduce the Nambu spinors $\Psi_{\mathbf{p}\ell\alpha} = (d_{\mathbf{p}\ell\alpha}, d^\dagger_{-\mathbf{p}\ell\alpha})$, which allows us to write the Hamiltonian as

$$H = \frac{1}{2} \sum_{\ell,\ell',\mathbf{p}\alpha\beta} \Psi^\dagger_{\mathbf{p}\ell\alpha} \left[\mathcal{H}_{BdG}(\mathbf{p}) \right]_{\ell,\alpha;\ell',\beta} \Psi_{\mathbf{p}\ell'\beta} + H_{\Delta^2} \quad (5.10)$$

where

$$\left[\mathcal{H}_{BdG}(\mathbf{p}) \right]_{\ell,\alpha;\ell',\beta} = \begin{pmatrix} \varepsilon_\alpha(\mathbf{p})\delta_{\alpha\beta} & \hat{\Delta}_{\ell,\alpha;\ell',\beta}(\mathbf{p}) \\ \hat{\Delta}^\dagger_{\ell,\alpha;\ell',\beta}(\mathbf{p}) & -\varepsilon_\alpha(-\mathbf{p})\delta_{\alpha\beta} \end{pmatrix} \quad (5.11)$$

is the BdG Hamiltonian. Note that when $\hat{\Delta}_{\ell,\alpha;\ell',\beta} = 0$ for $\ell' \neq -\ell$ (i.e. when only zero

total momentum pairing is present), one can remove the magnetic flavor indices ℓ and work on the non-reduced MBZ instead, replacing $\hat{\Delta}_{\ell,\alpha;-\ell,\beta}(\mathbf{p})$ with $\hat{\Delta}_{\alpha\beta}(\mathbf{p}+\ell\mathbf{Q})$, so that the BdG Hamiltonian is a $2q \times 2q$ matrix. In all other cases, however, the unit cell needs to be extended due to the breaking of the $\hat{T}_y$ MTG symmetry, resulting in the q-fold folding of the MBZ into the rMBZ, in which case we have to work with a $2q^2 \times 2q^2$ BdG Hamiltonian.

5.3.2 Ginzburg-Landau Free Energy

To obtain the gap function in the mean field approach we need to minimize the free energy, which yields the self-consistent gap equation. The free energy is in turn obtained from Eq. (5.7) by integrating out the $\Psi_{\mathbf{p}\ell\alpha}$ fields from the partition function. For this part of the calculation we assume that the pairing happens only in one band α and so drop the band index. Using the Matsubara formalism we then find

$$\mathcal{F} = -T \sum_{\omega,\mathbf{p}} \mathrm{Tr}\left[\log \beta \mathcal{G}^{-1}(i\omega, \mathbf{p})\right] + H_{\Delta^2} \tag{5.12}$$

where $\omega = (2\pi j + 1)T$ with integer j are the Matsubara frequencies and we defined the Gor'kov Green's function

$$\begin{aligned} \mathcal{G}(i\omega, \mathbf{p}) &= \left(i\omega - \mathcal{H}_{BdG}(\mathbf{p})\right)^{-1} = \\ &= \begin{pmatrix} \hat{G}(i\omega, \mathbf{p}) & \hat{F}(i\omega, \mathbf{p}) \\ \hat{F}^\dagger(i\omega, \mathbf{p}) & -\hat{G}^T(-i\omega, -\mathbf{p}) \end{pmatrix} . \end{aligned} \tag{5.13}$$

Minimizing $\mathcal{F}$ with respect to $\hat{\Delta}^\dagger$ gives the gap equation

$$\hat{\Delta}_{\ell+n,-n}(\mathbf{p}) = T \sum_{\omega \mathbf{p}' m} g^{(\ell)}_{nm}(\mathbf{p}; \mathbf{p}') \hat{F}_{\ell+m,-m}(i\omega, \mathbf{p}') \,. \tag{5.14}$$

Close below T_c we can expand the free energy and the Green's functions in powers of the gap function and obtain the linearized gap equation (see the Section in [61] for details):

$$\hat{\Delta}_{\ell+n,-n}(\mathbf{p}) = -\log\frac{1.13\Lambda}{T}\sum_{\mathbf{p}'m}\nu(\mathbf{p}')g^{(\ell)}_{nm}(\mathbf{p};\mathbf{p}')\hat{\Delta}_{\ell+m,-m}(\mathbf{p}') \tag{5.15}$$

where $\nu(\mathbf{p})$ is the momentum resolved density of states at the Fermi level and Λ is the high energy cutoff. We note that the linearized gap equation is equivalent to the 1 loop RG flow equation for the SC vertex and both give the same form of the gap function.

As shown in [61] and discussed above, for odd q the gap function belongs to a q-dimensional irrep which means that just as in the 1 loop RG flow there are q degenerate solutions of the linearized gap equation that we can label $\hat{\Delta}^{(L)}$ with $L = 0, \ldots, q-1$ labeling the total momentum $L\mathbf{Q}$ of the corresponding Cooper pairs. The solutions are picked such that

$$\hat{\Delta}^{(L)} \xrightarrow{\hat{T}_x} \hat{\Delta}^{(L-2)}\,, \tag{5.16}$$

$$\hat{\Delta}^{(L)} \xrightarrow{\hat{T}_y} \omega_q^{pL}\hat{\Delta}^{(L)}\,. \tag{5.17}$$

$\hat{\Delta}^{(L)}$ then form q components of the irrep that are eigenmodes of the $\hat{T}_y$ symmetry and are generated by the $\hat{T}_x$ symmetry [61]. Because the linearized gap equation is linear (as is the 1 loop RG vertex flow equation), any linear combination

$$\hat{\Delta}(\mathbf{p}) = \sum_L \eta_L \hat{\Delta}^{(L)}(\mathbf{p}) \tag{5.18}$$

is a solution for any choice of the complex parameters η_L. The vector $\boldsymbol{\eta} = (\eta_0, \ldots, \eta_{q-1})$ constitutes the order parameter that is selected spontaneously once non-linear terms are included.

In order to obtain the higher order terms we take Eq. (5.18) as the ansatz, plug

it into the free energy in Eq. (5.12) and sum over the momentum $\mathbf{p}$, which yields the macroscopic Ginzburg-Landau free energy

$$\mathcal{F} = a\left|\boldsymbol{\eta}\right|^2 + \sum_{MN} b_{MN} \sum_{L} \eta^*_{L+M}\eta^*_{L-M}\eta_{L+N}\eta_{L-N} \tag{5.19}$$

where the parameters a and b_{MN} are

$$\begin{aligned} a &= H_{\Delta^2} - \log\frac{1.13\Lambda}{T}\sum_{\mathbf{p}}\nu(\mathbf{p})\mathrm{Tr}\left[\hat{\Delta}^{(L)\dagger}\hat{\Delta}^{(L)}\right], \\ b_{MN} &= \frac{7\zeta(3)}{32\pi^2T^2}\sum_{\mathbf{p}}\nu(\mathbf{p})\mathrm{Tr}\left[\hat{\Delta}^{(L+M)\dagger}\hat{\Delta}^{(L+N)}\hat{\Delta}^{(L-M)\dagger}\hat{\Delta}^{(L-N)}\right]. \end{aligned} \tag{5.20}$$

In order to compute the fourth order b_{MN} coefficients, we note that the point with high DOS $\nu(\mathbf{p})$ dominate in the sum, so we can get an approximate expression by restricting the sum only to the VHS points $\mathbf{K}_{\ell,\mathrm{v}}$.

5.4 Renormalization Group Analysis

In this section, we extend the RG analysis developed previously for the half-filled square lattice [74, 75, 157] and the quarter-filled hexagonal lattice [77] with 2 and 3 VHSs, respectively, to the patch model with $2q$ VHSs presented above. The competing instability channels fall into two classes: particle-particle channels with momentum transfers $\ell\mathbf{Q}$; and particle-hole channels with momentum transfers $(\pi,\pi)/q + \ell\mathbf{Q}$. Due to the MTG symmetries, all the susceptibilities are independent of the magnetic flavor indices ℓ, and the two relevant susceptibilities are $\Pi_{pp}(\ell\mathbf{Q}) \approx \nu_0 \ln^2\Lambda/T$ and $\Pi_{ph}((\pi,\pi)/q + \ell\mathbf{Q}) \approx d_{ph}\nu_0\ln^2\Lambda/T$ where Λ is the high energy cutoff, T is the temperature and $\nu_0\ln\Lambda/E$ is the DOS at energy E above the VHS [77, 86, 157]. Here we introduce the standard phenomenological detuning parameter $d_{ph} = \Pi_{ph}/\Pi_{pp} \in [0,1]$ to account for possibly imperfect nesting in the particle-hole channels due to addi-

tional symmetry allowed terms that break particle-hole symmetry at half-filling or for chemical potentials slightly away from the VHSs [157]. For one loop RG, we obtain the following flow equations for the coupling constants (repeated indices are summed over):

$$
\begin{aligned}
\dot{g}^{(\ell)1}_{mn} &= -g^{(\ell)1}_{mk} g^{(\ell)1}_{kn} - g^{(\ell)4}_{mk} g^{(\ell)4*}_{nk} \\
\dot{g}^{(\ell)1'}_{mn} &= -g^{(\ell)1'}_{mk} g^{(\ell)1'}_{kn} - g^{(\ell)4*}_{km} g^{(\ell)4}_{kn} \\
\dot{g}^{(\ell)2}_{mn} &= d_{ph} \left(g^{(\ell+n-k)2}_{mk} g^{(\ell+m-k)2}_{kn} + g^{(\ell+n-k)4*}_{k,m-1} g^{(\ell+m-k)4}_{k,n-1} \right) \\
\dot{g}^{(\ell)3}_{mn} &= 2 d_{ph} g^{(\ell+m+n+k)3}_{-n-k,-m-k} \left(g^{(k)2}_{m,-n-k} - g^{(k)3}_{mn} \right) + d_{ph} g^{(\ell+m+n+k)4}_{-n-k,-m-k} \left(g^{(k)4*}_{n,-m-k} - 2 g^{(k)4*}_{n,m-1} \right) \\
&\quad + d_{ph} g^{(\ell+m+n+k)4}_{-n-k,-n-\ell-1} g^{(k)4*}_{n,m-1} \\
\dot{g}^{(\ell)4}_{mn} &= -g^{(\ell)1}_{mk} g^{(\ell)4}_{kn} - g^{(\ell)4}_{mk} g^{(\ell)1'}_{kn} + d_{ph} \left(g^{(\ell+n-k)2}_{k-\ell-m-n,-\ell-n} g^{(\ell+m-k)4}_{kn} + g^{(\ell+n-k)4}_{mk} g^{(\ell+m-k-1)2}_{k+1,n+1} \right) \\
&\quad + d_{ph} g^{(\ell+m+n+k)4}_{-n-k,-m-k} \left(g^{(k-1)2}_{-m-k+1,n+1} - 2 g^{(k-1)3}_{1-k-m,-k-n} \right) + d_{ph} g^{(\ell+m+n+k)4}_{-n-k,-n-\ell-1} g^{(k-1)3}_{1-k-m,-k-n} \\
&\quad + d_{ph} g^{(\ell+m+n+k)3}_{-n-k,-m-k} g^{(k)4}_{-m-k,n} + d_{ph} \left(g^{(\ell+m+n+k),2}_{-n-k,-n-\ell} - 2 g^{(\ell+m+n+k)3}_{-n-k,-m-k} \right) g^{(k)4}_{mn} ,
\end{aligned}
\tag{5.21}
$$

where we have used the particle-particle susceptibility $t = \Pi_{pp}(E) = \nu_0 \ln^2 \Lambda/E$ as the RG time. High energy modes are integrated above the energy scale E. For $q = 1$, i.e. zero flux, Eq.5.21 reduces to the standard result for the half-filled square lattice in [74].

Under the RG flow some of the coupling constants diverge at some finite RG time t_c, indicating an instability of the Fermi surface (see Fig. 5.2 (a) and (c)). To study these instabilities, we classify the vertices into SC, CDW and SDW to study their

flow:

$$\begin{aligned} H_{SC} &= \Delta^{(\ell)}_{m;\mathrm{v}} i\sigma^{y}_{\sigma\sigma'} d^{\dagger}_{\ell+m,\mathrm{v},\sigma} d^{\dagger}_{-m,-\mathrm{v},\sigma'} + h.c. \\ H_{CDW} &= \rho^{[\ell]}_{m;\mathrm{v}} d^{\dagger}_{\ell+m,-\mathrm{v},\sigma} d_{m,1+\mathrm{v},\sigma} \\ H_{SDW} &= \mathbf{M}^{[\ell]}_{m;\mathrm{v}} \cdot \boldsymbol{\sigma}_{\sigma\sigma'} d^{\dagger}_{\ell+m,-\mathrm{v},\sigma} d_{m,1+\mathrm{v},\sigma'} \end{aligned} \tag{5.22}$$

with summation over the indices implied. $\Delta^{(\ell)}_{m;\mathrm{v}}$, $\rho^{[\ell]}_{m;\mathrm{v}}$, and $\mathbf{M}^{[\ell]}_{m;\mathrm{v}}$ are the corresponding SC, CDW, and SDW order parameters respectively with momentum transfers $\ell\mathbf{Q}$ for SC and $(\pi,\pi)/q + \ell\mathbf{Q}$ for the CDW and SDW. Additionally, in order to determine which instability actually takes place, we consider the flow of the susceptibilities χ_I where $I = \Delta^{(\ell)}_{m;\mathrm{v}}$, $\tilde{\rho}^{[\ell]}_{k;\mathrm{v}}$, $\tilde{M}^{[\ell]}_{k;\mathrm{v}}$ corresponding to the instability[86, 144].

We studied the RG equations for $p/q = 1/2, 1/3$ and $2/3$, with the results summarized in Table 5.1. For zero flux, $q = 1$, we have recovered the results for the square lattice with repulsive interactions at half-filling [74, 75, 157]. We now analyse the resulting instabilities for $q \neq 1$ where the magnetic field is applied. In this case, the RG Eq.(5.21) in principle allow for a large number of fixed trajectories that characterize the instabilities of the Hofstadter metal.

	$q=2$, $d_{ph}=1$	$q=3$, $d_{ph}=1$		$q=3$, $d_{ph}=0.8$	
Filling	$1/4, 3/4$	$1/6, 5/6$	$1/2$	$1/6, 5/6$	$1/2$
I	$\Delta^{(0,+,-)}$	$\tilde{M}^{[1]}_0$	$\tilde{\rho}^{[1]}_2$	Δ	$\tilde{\rho}^{[1]}_2$
α_I	0.73	0.68	0.67	0.65	0.76
Symmetry	$\hat{T}_x$, $\hat{T}_y$, $\hat{C}_4(-1)$	$\hat{T}_x(\omega_3)$, $\hat{T}_y$	$\hat{T}_x(\omega_3)$, $\hat{T}_y(\omega_3^2)$	$\hat{T}_x\hat{T}_y(\omega_3^n)$, $\hat{S}$	$\hat{T}_x(\omega_3)$, $\hat{T}_y(\omega_3^2)$

Table 5.1: Summary of instabilities $I = \Delta, \tilde{M}^{[\ell]}_k$, and $\tilde{\rho}^{[\ell]}_k$, (SC, SDW, and CDW respectively) found in the RG analysis for $q = 2$ (column two) and $q = 3$ at ($d_{ph} = 1$, next two columns) and away from ($d_{ph} = 0.8$, last two columns) perfect nesting in the particle-hole channels. The second row indicate the fillings corresponding to the VHSs at which the instabilities are found. The fourth row indicates the critical exponent α_I of the corresponding instability and the last row shows its symmetry; values in parentheses indicate the phase picked up by the order parameter under the symmetry, e.g. $\Delta^{(0,+,-)} \xrightarrow{\hat{C}_4} -\Delta^{(0,+,-)}$. Recall that $\omega_q = e^{2\pi i/q}$.

5.4.1 Self-similar Fixed Trajectories

We have found that the RG equations Eq.(5.21) admit a universal fixed point trajectory characterized by $g_{mn}^{(\ell)j} = g_j/\sqrt{q}$, i.e. coupling constants independent of the magnetic flavor indices and depending only on the VHS patch indices. In this case, g_j again satisfy the same set of equations as for $q = 1$ [74] and we refer to such solutions as self-similar fixed trajectories. Remarkably, we find numerically that when SC becomes the leading instability for $q = 3$, the coupling constants tend asymptotically to this self-similar fixed trajectory. The existence of a self-similar behavior in the RG equations and their relation to unconventional SC is one of the main results of this chapter.

5.4.2 Instabilities for $q = 2$

Unlike the $q = 1$ case, for $q = 2$ we find that an SC instability occurs already at perfect nesting in both Hofstadter bands. As shown in [61], in this case the SC orders belong to one of four one dimensional irreducible representations (irreps) of the MTG determined by the gap function being even or odd under $\hat{T}_y$ and $\hat{T}_x$. The SC phase that wins in our RG calculation is even under both $\hat{T}_y$ and $\hat{T}_x$, which corresponds to $\Delta_{m;\mathrm{v}}^{(1)} = 0$ and $\Delta_{0;\mathrm{v}}^{(0)} = \Delta_{1;\mathrm{v}}^{(0)}$ respectively. Furthermore, we find that $\Delta_{m;0}^{(0)} = -\Delta_{m;1}^{(0)}$ (see Fig. 5.3 (a)), which implies that the gap function is odd under the magnetic $\hat{C}_4$ rotation. We note that this is an exceptional case, as for $q > 2$ the gap function necessarily breaks one of the MTG symmetries, and must either break the $\hat{C}_4$ symmetry or break the remaining MTG symmetry [61]. Only when the gap function is both even or both odd under $\hat{T}_x$ and $\hat{T}_y$, as in the present case, can it also have a well-defined $\hat{C}_4$ symmetry.

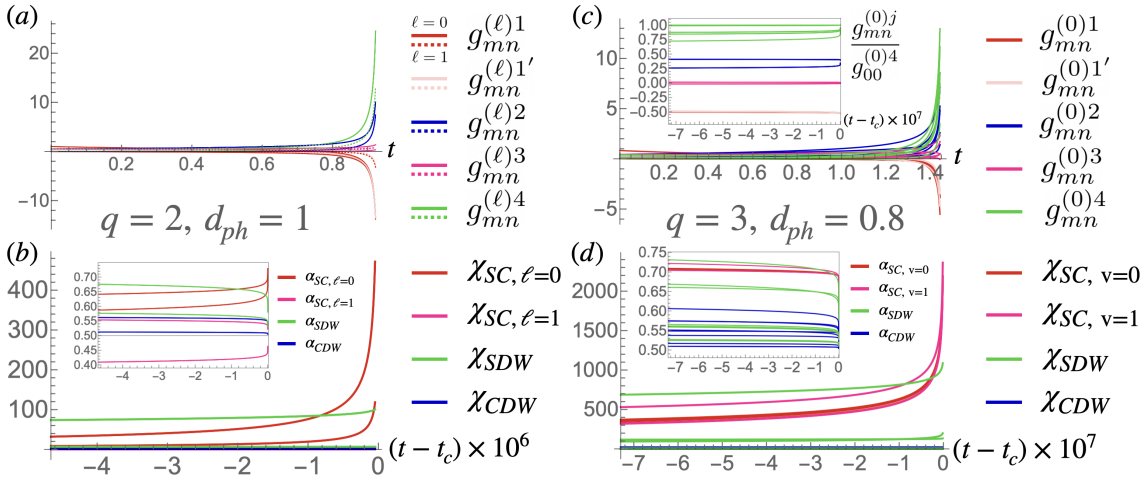

Figure 5.2: RG flow of coupling constants $g^{(\ell)j}_{mn}$ with $\ell = 0, 1$ (solid and dashed lines respectively), $j = 1, 1', 2, 3, 4$ (red, light red, blue, magenta and green respectively), and $m, n = 0, \ldots, q-1$ for (a) $q = 2$ at 1/4 filling at perfect nesting $d_{ph} = 1$; and for (c) $q = 3$ at 1/6 filling with $d_{ph} = 0.8$ ($U = 1$ in arbitrary units in all plots). The instability occurs at $t_c = 0.93$ and $t_c = 1.46$ for $q = 2$ and 3 respectively. The flows for $q = 2$ and 3 are otherwise qualitatively similar, and both are similar to the flow in the absence of the magnetic field: while all coupling constants are initially positive or vanish, $g^{(\ell)1}_{mn}$ and $g^{(\ell)1'}_{mn}$ eventually change sign, leading to effective attraction in the pairing channel. The inset in (c) shows the $q = 3$ flow normalized by $g^{(0)4}_{00}$ which shows that the self-similar fixed trajectory $g^{(\ell)j}_{mn} = g_j/\sqrt{q}$ is reached at the end of the flow, as indicated by curves of the same color approaching the same value (we also find $g_1 = g_{1'}$). (b) $q = 2$ RG flow of the susceptibilities χ_I with I corresponding to SC with Cooper pairs with zero momentum ($\ell = 0$, red) or momentum $\mathbf{Q} = \frac{2\pi p}{q}\hat{\mathbf{y}}$ ($\ell = 1$, magenta), SDW (green) or CDW (blue). Initially χ_{SDW} is the fastest growing susceptibility, but eventually The $\ell = 0$ SC susceptibility takes over. The inset shows the corresponding critical exponents $\alpha_I = \left(1 - \log_{t_c - t}\chi_I\right)/2$ for the same range of RG times t. The largest exponent at the end of the flow is $\alpha_{SC,\ell=0}(t_c) \approx 0.73$. (d) Shows that analogous plots for $q = 3$, but in this case the $\ell = 0$ and 1 SC channels are degenerate so only the former is plotted; in this case red and magenta colors indicate the suscpetibilities at v = 0 and 1 VHS points respectively, which contribute to the same SC channel. The largest exponent at the end of the flow is $\alpha_{SC}(t_c) \approx 0.65$.

5.4.3 Instabilities for $q = 3$

For $q = 3$ we do not find a definitive winning instability at perfect nesting: depending on the initial value of the vertices, either SC or $\tilde{\rho}_2^{[1]}$ CDW susceptibility can diverge first in the middle band, while SC or $\tilde{M}_0^{[1]}$ SDW diverge first in the top and bottom bands. This suggests strongly competing instabilities that likely remain degenerate at perfect nesting as in the $q = 1$ case, and a small detuning from perfect nesting generally favors SC instabilities. We find that for $d_{ph} = 0.8$, SC is a clear winner in the top and bottom bands at 1/6 and 5/6 fillings, but CDW remains the apparent leading instability at half-filling. Remarkably, we find that when SC is the winning instability, the RG flow approaches the self-similar fixed trajectory $g_{mn}^{(\ell)j} = g_j/\sqrt{q}$ within numerical accuracy, as shown in the inset in Fig. 5.2 (c). We therefore expect the results for the $q = 1$ case to generalize in this case.

Indeed, the SC phase we find in the top and bottom bands satisfies $\Delta_{m;\mathrm{v}}^{(0)} = \Delta_{m+1;\mathrm{v}}^{(0)}$ and $\Delta_{m;0}^{(0)} = -\Delta_{m;1}^{(0)}$, similar to the $q = 2$ and $q = 1$ cases. Unlike those cases, however, there is no natural interpretation of these relations in terms of MTG and $\hat{C}_4$ symmetries. As shown in [61], in this case the gap function transforms according to a 3D irrep of the MTG and necessarily breaks at least one of $\hat{T}_x$ or $\hat{T}_y$, and any $\hat{C}_4$ symmetric gap breaks all of the MTG symmetries.

In order to determine the symmetries of the resulting degenerate ground states it is necessary to minimize the fourth order terms in the Ginzburg-Landau free energy Eq.(5.19). We thus find that the solutions are of the form $|\eta_L| = \eta$, $\arg[\eta_L] = \pm 4\pi/3\delta_{LM}$ for some fixed $M = 0, 1, 2$, for a total of six solutions. As shown in [61], these solutions are precisely the solutions symmetric under $\omega_3^{pM}\hat{T}_x\hat{T}_y^{\pm 1}$ for the + and − cases respectively (equivalently, the gap functions pick up a phase of ω_3^{-2pM} under $\hat{T}_x\hat{T}_y^{\pm 1}$). The fact that there are six solutions instead of three as one would expect from the breaking of the $\hat{T}_x$ symmetry is due to the fact that the $\hat{C}_4$ symmetry is also broken and maps $\hat{T}_x\hat{T}_y$ to $\hat{T}_y\hat{T}_x^{-1}$. In all cases the ground states have a $\mathbb{Z}_3$ symmetry.

The $\mathbb{Z}_3$ symmetry determines the rest of the $\Delta^{(\ell)}_{m;\mathrm{v}}$ order parameters for $\ell \neq 0$, so below we will focus on the form of $\Delta^{(0)}_{m;\mathrm{v}}$ only.

The $\Delta^{(0)}_{m;\mathrm{v}} = \Delta^{(0)}_{m+1;\mathrm{v}}$ condition extended to $\Delta^{(0)}_{m}(\mathbf{p}) = \Delta^{(0)}_{m+1}(\mathbf{p})$ on the full rMBZ implies an additional symmetry that emerges under the RG flow, which we refer to as a self-similarity symmetry $\hat{S}$. This symmetry acts as on the gap function as

$$\Delta(\mathbf{p}) \xrightarrow{\hat{S}} \hat{T}_x(\mathbf{p})\Delta(\mathbf{p})\hat{T}_x(-\mathbf{p}) \tag{5.23}$$

which is in contrast to the canonical action of $\hat{T}_x$ itself, which acts as $\Delta(\mathbf{p}) \xrightarrow{\hat{T}_x} \hat{T}_x(\mathbf{p})\Delta(\mathbf{p})\hat{T}^T_x(-\mathbf{p})$ [61]). Stated another way, $\hat{S}$ acts as $\hat{T}_x$ on the particle sector but as $\hat{T}^{-1}_x$ on the hole sector in the Nambu space of the Bogoliubov-de Gennes (BdG) formalism. In the sub-lattice basis $c_{\mathbf{k}s}$, $\hat{S}$ acts on the gap function as $\Delta^{(\ell)}_{ss'}(\mathbf{k}) \xrightarrow{\hat{S}} \Delta^{(\ell)}_{s-1,s'+1}(\mathbf{k}+\mathbf{Q})$.

5.5 Projected Gap Functions

Since the RG only determines the order parameter at the VHS points, it is necessary to extend it to determine the nature of the resulting phase (chiral or nodal). In principle, one needs to extend the RG calculation to the whole BZ, which is computationally prohibitive already for moderate q. Even solving the self-consistent gap equation for a constant Hubbard interaction numerically is quite challenging. We therefore adopt a simpler approach and construct an ansatz gap function in real space in the $c_{\mathbf{r}\sigma}$ basis first (e.g. standard s- or d-wave gap functions with up to nearest neighbor terms, etc.), and then projecting onto the Hofstadter band of interest via $d_{\mathbf{k}\alpha\sigma} = \sum_s \mathcal{U}^s_\alpha(\mathbf{k}) c_{\mathbf{k}s\alpha}$ with the band index α fixed.

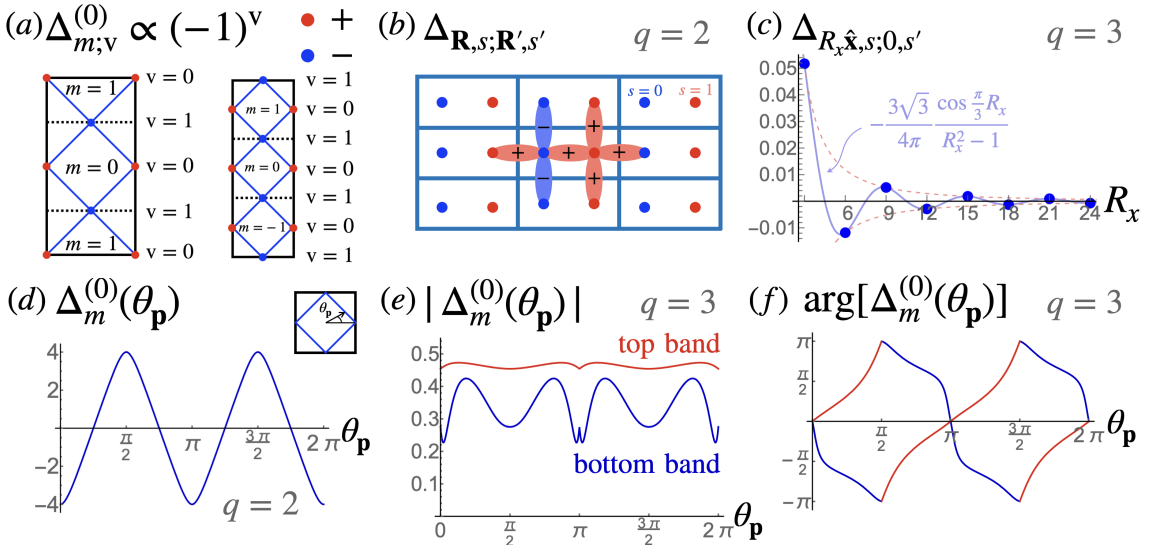

Figure 5.3: **(a)** Gap functions at the VHS obtained from the RG analysis for $q = 2$ at perfect nesting (left) and for $q = 3$ at $d_{ph} = 0.8$ in the top and bottom Hofstadter bands (right). In both cases the gap function changes sign between the two VHSs $\mathrm{v} = 0, 1$. Here we focus on pairing with zero total momentum $\ell = 0$, with pairings for $\ell \neq 0$ determined by MTG symmetries. **(b)** Real space structure of the gap function for $q = 2$ even under $\hat{T}_1$ and $\hat{T}_2$ and odd under $\hat{C}_4$, shown within a single magnetic unit cell (the pattern repeats in all cells). **(c)** Profile of the gap function $\Delta_{R_x\hat{\mathbf{x}},s;0,s'}$ for $q = 3$ as a function of the horizontal magnetic unit cell separation R_x between Cooper pairs (with lattice constant $a = 1$). Note that the gap function oscillates between each unit cell and decays as $1/R_x^2$ at long distances. See Section 5.5 for more details. **(d)** The projection onto the Fermi surface of the gap function for $q = 2$ shown in **(b)** as a function of the angle $\theta_{\mathbf{p}}$ along the Fermi surface within the rMBZ (note that $\Delta^{(\ell)}_m$ are equal within each patch m). Note that the gap crosses zero, indicating nodes in the fermionic spectrum. **(e-f)** The projection onto the Fermi surface of the model gap function for $q = 3$ for the top (red) and bottom (blue) bands that agrees with the gap function found in the RG analysis. Note that the magnitude of the gap function never vanishes as shown in **(e)**, implying that the fermionic spectrum is fully gapped (the sharp features at $\theta_{\mathbf{p}} = 0, \pi$ are due to the corners of the Fermi surface). The phase of the projected gap functions, however, winds by $\pm 4\pi$ around the Fermi surface in the top and bottom bands respectively, as shown in **(f)**, implying each $\Delta^{(\ell)}_m$ contributes ± 2 to the Chern number. Plots **(c-e)** are given in arbitrary units as the magnitude of the gap function is not determined within the weak coupling theory.

The gap function at the VHSs is defined as

$$H_{SC,VHS} = \sum_{\ell,m,\mathrm{v}} \Delta^{(\ell)}_{m;\mathrm{v}} d^{\dagger}_{\ell+m,\mathrm{v}} d^{\dagger}_{-m,-\mathrm{v}} + h.c. \tag{5.24}$$

where $\mathrm{v} = 0, 1$ is the VHS index and $m = 0, \ldots, q-1$ is the magnetic flavor index. The full gap function defined on the reduced MBZ is

$$\begin{aligned} H_{SC} &= \sum_{\ell,m,\mathbf{p}} \Delta^{(\ell)}_{m}(\mathbf{p}) d^{\dagger}_{\mathbf{p},\ell+m} d^{\dagger}_{-\mathbf{p},-m} + h.c. = \\ &= \sum_{m,n,\mathbf{p}} \hat{\Delta}_{mn}(\mathbf{p}) d^{\dagger}_{\mathbf{p},m} d^{\dagger}_{-\mathbf{p},n} + h.c \end{aligned} \tag{5.25}$$

where the latter is the notation of [61]. The gap function can be extended to include pairing between different bands α and β:

$$\begin{aligned} H_{SC} &= \sum_{m,n,\alpha,\beta,\mathbf{p}} \hat{\Delta}_{m\alpha,n\beta}(\mathbf{p}) d^{\dagger}_{\mathbf{p}\alpha m} d^{\dagger}_{-\mathbf{p}\beta n} + h.c = \\ &= \sum_{m,n,s,s',\mathbf{p}} \Delta_{m,s;n,s'}(\mathbf{p}) c^{\dagger}_{\mathbf{p}+m\mathbf{Q},s} c^{\dagger}_{-\mathbf{p}+n\mathbf{Q},s'} = \\ &= \sum_{\mathbf{R},\mathbf{R}',s,s'} \Delta_{\mathbf{R},s;\mathbf{R}',s'} c^{\dagger}_{\mathbf{R}s} c^{\dagger}_{\mathbf{R}',s'} \end{aligned} \tag{5.26}$$

$\Delta_{m,s;n,s'}(\mathbf{p})$ is thus the gap function in the sub-lattice basis. We further define $\Delta^{(\ell)}_{ss'}(\mathbf{k})$ with $\mathbf{k}$ defined in the un-reduced MBZ via $\Delta_{m,s;n,s'}(\mathbf{p}) = \Delta^{(m+n)}_{ss'}(\mathbf{p} + (m-n)\mathbf{Q}/2)$. $\Delta^{(\ell)}_{ss'}(\mathbf{k})$ is then simply the gap function in the sub-lattice basis corresponding to pairing with total momentum $\ell\mathbf{Q}$ and defined on the original MBZ. We thus have

$$\begin{aligned} \hat{\Delta}_{m\alpha,n\beta}(\mathbf{p}) &= \sum_{ss'} \mathcal{U}^{s}_{\alpha}(\mathbf{p}+m\mathbf{Q}) \mathcal{U}^{s'}_{\beta}(-\mathbf{p}+n\mathbf{Q}) \Delta_{m,s;n,s'}(\mathbf{p}) \\ &= \sum_{ss'} \mathcal{U}^{s+m}_{\alpha}(\mathbf{p}) \mathcal{U}^{s'+n}_{\beta}(-\mathbf{p}) \Delta_{m,s;n,s'}(\mathbf{p}) \end{aligned} \tag{5.27}$$

The second line follows from our gauge choice $\mathcal{U}_\alpha^{s+1}(\mathbf{k}+\mathbf{Q}) = \mathcal{U}_\alpha^s(\mathbf{k})$. We also have

$$\Delta_{m,s;n,s'}(\mathbf{p}) = \frac{1}{N}\sum_{\mathbf{R},\mathbf{R}'} e^{-i(\mathbf{p}+m\mathbf{Q})\cdot\mathbf{r}-i(-\mathbf{p}+n\mathbf{Q})\cdot\mathbf{r}'}\Delta_{\mathbf{R},s;\mathbf{R}',s'} = \\ = \frac{1}{N}\sum_{\mathbf{R},\mathbf{R}'} e^{-i\mathbf{p}\cdot(\mathbf{r}-\mathbf{r}')-i\mathbf{Q}\cdot(m\mathbf{r}+n\mathbf{r}')}\Delta_{\mathbf{R},s;\mathbf{R}',s'} \tag{5.28}$$

or equivalently

$$\Delta^{(\ell)}_{ss'}(\mathbf{k}) = \frac{1}{N}\sum_{\mathbf{R},\mathbf{R}'} e^{-i\mathbf{k}\cdot(\mathbf{r}-\mathbf{r}')-i\ell\mathbf{Q}\cdot(\mathbf{r}+\mathbf{r}')/2}\Delta^{(\ell)}_{\mathbf{R},s;\mathbf{R}',s'} = \\ = \frac{1}{N}\sum_{\mathbf{R},\mathbf{R}'} e^{-i\mathbf{k}\cdot(\mathbf{r}-\mathbf{r}')-i\ell\mathbf{Q}\cdot(\mathbf{R}+\mathbf{R}')/2}\Delta^{(\ell)}_{\mathbf{R},s;\mathbf{R}',s'} \tag{5.29}$$

Note that $\Delta^{(\ell)}_{\mathbf{R}+\mathbf{R}'',s;\mathbf{R}'+\mathbf{R}'',s'} = e^{i\ell\mathbf{Q}\cdot\mathbf{R}''}\bar{\Delta}^{(\ell)}_{\mathbf{R},s;\mathbf{R}',s'}$. The projection of $\Delta_{m,s;n,s'}(\mathbf{p})$ (or equivalently $\Delta_{\mathbf{R},s;\mathbf{R}',s'}$) onto the α band simply amounts to computing $\hat{\Delta}_{m\alpha,n\alpha}(\mathbf{p}) \equiv \hat{\Delta}_{mn}(\mathbf{p})$, assuming the rest of the components vanish.

We then seek $\bar{\Delta}_{\mathbf{R},s;\mathbf{R}',s'}$ such that $\hat{\Delta}_{mn}(\mathbf{K}_{0,v}) = \Delta^{(\ell)}_{m;v}$ as found in the RG calculation. Note that thanks to the MTG symmetry, we can look at the $\ell = m+n = 0$ channel alone, the rest being obtained by simple application of $\hat{T}_x$ symmetry (for $q > 2$ we then find the MTG symmetry of the ground state by minimizing the fourth order free energy in Section 5.3). In particular, for both $q = 2$ and the lower and upper bands for $q = 3$ we found $\Delta^{(0)}_{m;0} = -\Delta^{(0)}_{m;1}$. We also use the relations in this section to establish the action of the self-similarity symmetry $\hat{S}$ in different bases. Recall that it imposes $\Delta^{(0)}_{m;v} = -\Delta^{(0)}_{n;v}$ for all m and n (for $q = 2$ we find the same relation, but as a consequence of the usual $\hat{T}_x$ symmetry). On $\hat{\Delta}_{mn}(\mathbf{p})$, this symmetry acts as

$$\hat{\Delta}_{mn}(\mathbf{p}) \xrightarrow{\hat{S}} \hat{\Delta}_{m+1,n-1}(\mathbf{p}) = \left[\tau\hat{\Delta}(\mathbf{p})\tau\right]_{mn} \tag{5.30}$$

where $\tau_{mn} = \delta_{m,n-1}$ is the shift matrix. This is in contrast to the action of $\hat{T}_x$ itself, which acts as $\hat{\Delta}_{mn}(\mathbf{p}) \xrightarrow{\hat{T}_x} \left[\tau\hat{\Delta}(\mathbf{p})\tau^T\right]_{mn} = \hat{\Delta}_{m+1,n+1}(\mathbf{p})$. From the action of the $\hat{S}$

in the band basis, we establish its action on the gap function components in other bases: e.g., it acts on $\Delta^{(\ell)}_{ss'}(\mathbf{k})$ as

$$\Delta^{(\ell)}_{ss'}(\mathbf{k}) \xrightarrow{\hat{S}} \Delta^{(\ell)}_{s-1,s'+1}(\mathbf{k}+\mathbf{Q}) \tag{5.31}$$

and as a convolution in real space:

$$\Delta_{\mathbf{R}s;\mathbf{R}'s'} \xrightarrow{\hat{S}} e^{-i\mathbf{Q}\cdot(\mathbf{R}-\mathbf{R}')} \sum_{X\in q\mathbb{Z}} \mathrm{sinc}\left[\frac{\pi}{q}(X+2)\right] \Delta_{\mathbf{R},s+1;\mathbf{R}'+X\hat{\mathbf{x}},s'-1} \tag{5.32}$$

where $\mathrm{sinc}(x) = \sin x/x$ is the inverse Fourier transform of e^{2ik_x}.

In the real space basis $c_{\mathbf{R}s}$, the action of this symmetry has a highly non-local character: $\Delta_{\mathbf{R}s;\mathbf{R}'s'} \xrightarrow{\hat{S}} e^{-i\mathbf{Q}\cdot(\mathbf{R}-\mathbf{R}')} \sum_{X\in q\mathbb{Z}} \mathrm{sinc}\left[\frac{\pi}{q}(X+2)\right] \Delta_{\mathbf{R},s+1;\mathbf{R}'+X\hat{\mathbf{x}},s'-1}$, where $\mathrm{sinc}(x) = \sin x/x$ (see Section 5.5 for details of the change of basis transformation). In particular, if $\Delta_{\mathbf{R}s;\mathbf{R}'s'}$ is symmetric under $\hat{S}$, it decays as $1/(R_x - R'_x)^2$, implying a long-range order and an obstruction to constructing fully localized Wannier states of the BdG Hamiltonian (see Fig. 5.3 (c)).

5.5.1 Gap Function for $q = 2$

For $q = 2$, the gap function $\Delta^{(0)}_m(\mathbf{p})$ is symmetric under $\hat{T}_x$, $\hat{T}_y$ and odd under $\hat{C}_4$, such that it takes a unique nearest-neighbor form in the $c_{\mathbf{k}s}$ basis, namely:

$$\Delta^{(0,+,-)}_{ss'}(\mathbf{k}) = \Delta_0 \left(\cos k_x \sigma^x_{ss'} - \cos k_y \sigma^z_{ss'}\right) \tag{5.33}$$

The anti-symmetry of this order parameter under $\hat{C}_4$ symmetry can be checked directly by using

$$\hat{C}_4 c_{\mathbf{p}+\ell\mathbf{Q},s\sigma} \hat{C}_4^\dagger = \frac{1}{\sqrt{q}} \sum_{s'\ell'} \omega_q^{-p(ss'+\ell s'+\ell' s)} c_{\bar{\mathbf{p}}+\ell'\mathbf{Q},s'\sigma} \tag{5.34}$$

where $\bar{\mathbf{p}} = (-p_y, p_x)$ (one can also check that the RHS in Eq. (5.34) is an eigenstate of $\hat{T}_x$). Fig. 5.3 (b) shows the corresponding gap function $\Delta_{\mathbf{R},s;\mathbf{R}',s'}$ in real-space in the $c_{\mathbf{R}s}$ basis. We will see in the next section that the gap function $\Delta_m^{(0)}(\mathbf{p})$ is then obtained by projecting $\Delta_{ss'}^{(0,+,-)}(\mathbf{k})$ onto the band basis $\mathbf{d}_{\mathbf{k}\alpha}$. Importantly, the resulting gap is nodal (see Fig. 5.3 (d)). A gap function of this form has been considered as a toy model of a nodal d-wave superconductor in a magnetic field in [338], but without a microscopic justification or a consideration of its symmetries presented here (indeed, the gap function in that model does not transform as a proper irreducible representation of the MTG for $q > 2$). The π-flux superconductor on a square lattice has also previously been studied using quantum Monte Carlo at half-filling, i.e. at the Dirac nodes of the normal spectrum, where a so-called ds^* SC phase has been found [339]. The corresponding gap function has the form $\Delta_{ss'}^{(0,+,+)}(\mathbf{k}) = \Delta_0 \left(\cos k_x \sigma^x_{ss'} + \cos k_y \sigma^z_{ss'}\right)$ and we find that it is precisely the $\hat{T}_x$, $\hat{T}_y$ symmetric gap that is *even* under $\hat{C}_4$, and therefore distinct from the phase we find in RG at VHS fillings.

5.5.2 Gap Function for $q = 3$

For $q = 3$, we find that the extended gap function respecting the $\hat{S}$ symmetry and matching the RG result at VHSs has a simple form in the sub-lattice basis:

$$\Delta_{ss'}^{(0)}(\mathbf{k}) = \Delta_0 \left[1 - \cos k_x - \cos(k_y - (s - s')Q)\right] \tag{5.35}$$

Though as mentioned above this gap function cannot be written down in real space using nearest neighbor terms, it can be constructed using an extended s-wave gap function $\Delta_{\mathbf{rr}'}^{(S)} = \Delta_0(\delta_{\mathbf{rr}'} - \sum_{\mathbf{a}} \delta_{\mathbf{r},\mathbf{r}'+\mathbf{a}}/2)$ where $\mathbf{a}$ is summed over all nearest neighbors of the square lattice. The real space order parameter can then be obtained by repeatedly applying the $\hat{S}$ symmetry discussed in Section 5.4, $\Delta_{\mathbf{R}s;\mathbf{R}'s'} = \sum_j \hat{S}^j \left[\Delta_{\mathbf{rr}'}^{(S)}\right]$.

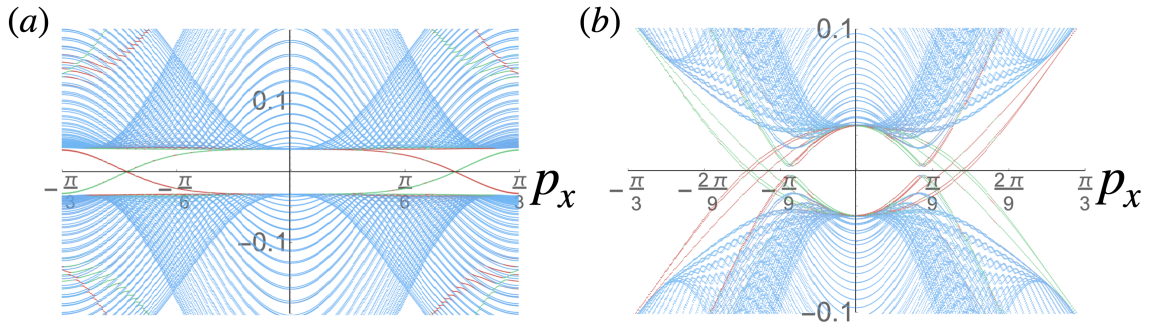

Figure 5.4: Edge modes in the BdG spectrum of the Hofstadter SC for $q = 3$ with cylindrical boundary conditions open in the y direction for the self-similar $\hat{T}_x\hat{T}_y$ symmetric gap function Eq. (5.35) at (a) 5/6 and (b) 1/6 filling (chemical potential $\mu = \pm 2.44$ respectively, with $t = 1$ and $\Delta_0 = 0.02$ in (a) and 0.2 in (b), taking 100 extended unit cells along the y direction; see Section 5.3 for details of the BdG Hamiltonian). The spectra are colored according to a weighted inverse participation ratio with green and red indicating states localized to the top and bottom edges of the cylinder respectively, while blue indicates bulk states. In (a) there are pairs of crossing edge modes at zero energy around $p_x = \pm 2\pi/9$, and we find that each is three-fold degenerate, corresponding to Chern number 6. In (b) there are six right-moving and six left-moving zero energy edge modes are located around $p_x = \pm\pi/6$, giving a total Chern number -6. Observe that the edge modes of the same color move in opposite direction in (a) and (b). Localized edge modes at higher energies that do not cross zero energy are the normal state edge modes that connect to higher energy Hofstadter bands not shown in the figure.

We then obtain the extension $\Delta_m^{(0)}(\mathbf{p})$ by projecting onto the band basis $\mathbf{d}_{\mathbf{p}\ell\alpha}$ (see Section 5.5), and find that the resulting order parameter is fully gapped and chiral, $\Delta_m^{(0)}(\mathbf{p}) \sim e^{\pm 2i\theta}$ with $\pm$ for the upper and lower bands respectively, contributing a Chern number of ± 2 (see Fig. 5.3 (e-f)). An important consequence of the $\hat{S}$ symmetry is the three fold degeneracy of the BdG spectrum of the fermionic excitations, which therefore implies that the total Chern number of this phase is ± 6. In the next section, we verify this property numerically for the $\hat{T}_x\hat{T}_y$ symmetric gap function by computing edge mode in a finite system with cylindrical boundary conditions periodic in the x direction and open in the y direction (taking advantage of the gap function being short-ranged in the latter). The resulting spectrum is shown in Fig. 5.4.

5.6 Summary and Discussion

Hofstadter systems have recently experienced a renaissance caused by the advent of 2D moiré superlattices realizing large magnetic fluxes in laboratory accessible magnetic fields. For nearly four decades, Hofstadter bands have been predominantly studied as platforms for the quantum Hall effect, following the seminal work of Thouless and collaborators [22] that showed that it is a consequence of the topology of filled Hofstadter bands. However, this connection between Hofstadter systems and quantum Hall effect is but one aspect of the rich physics embodied by fractal electronic bands.

This chapter invites a broader view on the potentialities of Hofstadter quantum materials. Rather surprisingly, using the powerful renormalization group method we showed that repulsive interactions can produce superconductivity when the Fermi energy lies in the vicinity of Van Hove singularities that are tunable and generically present in every Hofstadter band. The resulting prediction of emergent superconductivity in Hofstadter bands is surprising not just because of the role played by

electronic interactions, but also - and perhaps primarily - because it describes the formation of Cooper pairs in large magnetic fields that cause a strong orbital effect commonly viewed as detrimental for superconductivity. Our analysis therefore establishes a new microscopic mechanism for the realization of reentrant superconductivity in Hofstadter materials, which could be within near-term experimental reach in moiré superlattices. We have investigated the nature of electronic instabilities on the square lattice Hofstadter-Hubbard model, using weak coupling renormalization group to characterize competing electronic orders when the Fermi level is brought near a manifold of $2q$ VHSs and the flux per unit cell is $\Phi = 2\pi p/q$.

The main contributions presented in this chapter are:

- We have established the form of the repulsive Hubbard interaction at the q-fold degenerate VHSs of the Hofstadter bands. We have derived the symmetries of the coupling constants under a canonical gauge that is consistent with the magnetic translations, such that the $2q$ projected interactions at the VHSs are classified into five groups.

- We have performed a Fermionic RG analysis allowing for the treatment of competing instabilities on equal footing, revealing how the progressive elimination of high energy modes renormalizes the bare repulsive interactions and opens low energy instability channels.Our analysis shows a rich set of RG equations that possess self-similar fixed trajectories related to the RG equations at zero field. Remarkably, we find that the self-similar fixed trajectory is reached by the RG flow for $q = 3$ when the SC instability occurs.The existence of a self-similar structure in the RG flow is a remarkable property of Hofstadter systems that illustrates the power of the magnetic translation group in constraining the low energy instabilities.

- We analysed two representative instabilities found by the RG analysis, with

the results summarized in Table 5.1: First, for $p/q = 1/2$ corresponding to the TR-symmetric π-flux phase we have identified nodal d-wave superconducting instabilities near 1/4 and 3/4 fillings. The nodal order parameters are odd under the magnetic rotation $\hat{C}_4$ and have unusual real space structure (see Fig. 5.3 (b)) giving rise to a gapless spectrum of Bogoliubov quasiparticles that manifest themselves in a linear-in-temperature specific heat. Second, for $p/q = 1/3, 2/3$ corresponding to $\pm 2\pi/3$ flux lattices our analysis uncovers the existence of a novel chiral topological superconductors near 1/6 and 5/6 fillings. These TRS broken paired states break $\hat{C}_4$ symmetry while preserving a $\mathbb{Z}_3$ subgroup of the MTG, thus realizing a $\mathbb{Z}_3$ Hofstadter superconductor classified in Ref. [61].

- We have characterized the novel phases associated with these instabilities by a bulk Chern number topological invariant $\mathcal{C} = \pm 6$, which accounts for a chiral phase with 6 net chiral Majorana edge modes. A universal experimental signature of such phases is a quantized thermal Hall coefficient $\kappa_{xy}/T = 6 \times (\pi^2 k_B^2/3h)$.

- We have found that the chiral phases occur when the system flows to the self-similar trajectory of the RG equations and as a result possess a self-similarity symmetry $\hat{S}$ defined in Eq. (5.23) that forces the real-space order parameters to be long-ranged, providing another experimental signature of these phases. Moreover, since the self-similar trajectory is present for all q, the self-similar HSC instability is viable for all values of the magnetic flux. The prediction of unconventional nodal and self-similar topological superconductivity in partially filled Hofstadter bands form intrinsic electronic interactions is the main result of this chapter.

- We have found several closely competing spin and charge density wave instabilities that break MTG symmetries and that may be of experimental interest in

their own right. Below the transition temperature, these states can coexist with the HSC states and can give rise to rich and complex phase diagram similar to those of high T_c superconductors [340]. Moreover, the multi-component nature of the HSC order parameters implies that vestigial density wave orders may appear in the vicinity of the SC instability and can provide an experimental signature of these phases[304].

Our theoretical findings on the square lattice Hofstadter-Hubbard model may inform the realization of reentrant Hofstadter superconductivity in a number of experimental platforms, including optical lattices [316, 319–322] and twisted cuprate moiré systems [334, 335]. Moreover, the RG framework developed here for the square lattice can be directly generalized to other Hofstadter systems. A particularly interesting direction is to extend this formalism to effective lattice models describing the band structure of magic angle twisted bilayer graphene where $2\pi/3$ and π flux lattices can be realized at accessible magnetic fields $B \sim 8$ T and $B \sim 12$ T, respectively. In that regard, the experimental observation [309] of reentrant behavior in magic angle twisted bilayer graphene with small Zeeman splitting (~ 2 meV) may offer a promising route to search for emergence of Hofstadter superconductivity, enabled by the competition of electronic orders in the rich manifold of Van Hove singularities present in moiré Hofstadter superlattices.

The RG theory can also be extended to the case of spin polarized bands for materials in which the Zeeman splitting is strong. In that regime triplet Hofstadter superconductivity may become possible. Recent observations of triplet SC in twisted trilayer graphene [196, 341] as well as Bernal stacked bilayer graphene [342] indicate that this may be another promising route to realizing HSCs. Of course in all these systems, including TBG, strong correlation effects may play an important role, which are known to affect the Hofstadter spectrum [273, 343, 344] and have been seen to lead to fractional and ferromagnetic states in experiment in the Hofstadter regime

[2, 48, 98]. Including these strong coupling effects in the theory of Hofstadter superconductivity in the RG framework is a challenging task we leave for a future study, but we expect a non-trivial interplay of HSC with these strongly correlated states that can give rise to even more unconventional phases.

Chapter 6

Discussion and Outlook

In this thesis, we have investigated novel quantum collective phenomena of electrons in fractal Hofstadter bands. In particular, we have theoretically investigated novel topological phase transitions caused by lattice effects, provided a framework describing pairing of electrons in Hofstadter bands, and shown how the competition of electronic orders via repulsive interactions provides a pathway to novel symmetry-broken and topological electronic orders.

In Chapter 3, we established a theoretical framework describing topological quantum criticality in Hofstadter-Chern insulators (HCIs) on the honeycomb lattice. We found novel topological phase transitions described by a universality class of multi-flavor Dirac fermions, which arise from the coupling between topological states and the underlying lattice structure, which are distinct from traditional quantum Hall plateau transitions that occur in the Landau level regime. Exploiting the self-similarity of the Hofstadter bands, we identified a universal spectral function dubbed the Thouless function, which serves as a powerful tool in classifying the topological phase transitions tuned by the modulation of lattice hopping parameters on the honeycomb lattice. Furthermore, we have shown that these topological phase transitions are characterized by large jumps in the Hall conductance. Moreover, we have proposed a

general connection relating the energy scales of these quantum critical points with the presence of Van Hove singularities in Hofstadter-Chern bands. This work also opens many interesting directions to study quantum critical phenomena in superlattices. A promising direction would be to explore strain induce topological quantum criticality in van der Waals heterostructures. Furthermore, it is an open question whether the interplay of magnetic fields and higher order VHSs[189, 190] could provide even richer critical phenomena. The methods developed in this thesis serve as a starting point to address these future directions.

In Chapter 4, we established a theoretical framework of Hofstadter superconductivity, which is described as the charge $2e$ condensates formed by pairing of electrons in self-similar Hofstadter bands. We showed that the multi-dimensional order parameter of Hofstadter superconductors are classified by the irreducible representations of the magnetic translation group (MTG) acting on charge $2e$ fields. This led us to formulate a Ginzburg-Landau theory of Hofstadter superconductivity based on this group-theory analysis, which shows a rich phase diagram. A central result of our analysis is that the magnetic translation symmetries are necessarily broken when electron pairings arise in Hofstadter bands. In particular, we identified a new class of charge $2e$ condensate dubbed $\mathbb{Z}_q$ Hofstadter superconductor formed when MTG is broken down to a cyclic $\mathbb{Z}_q$ subgroup. Interestingly, these states can support unconventional excitations, such as Bogoliubov Fermi surfaces[121–132] and chiral Majorana edge states[133]. Therefore, our classification of electronic pairing in Hofstadter bands paves the way to exploring phenomena beyond that in conventional superconductors.

In Chapter 5, we developed a new theory of competing electronic orders in fermionic Hofstadter systems. In particular, we analyzed the role of repulsive Hubbard interaction in the vicinity of the VHSs of the Hofstadter bands. Due to magnetic translations, Hofstadter bands support a rich manifold of degenerate VHSs, whose number (proportional to q) can be tuned as a function of the magnetic flux $\Phi = 2\pi(p/q)h/e$ per

unit cell. Exploring this control knob, we performed a weak coupling renormalization group (RG) analysis which establishes a rich competition of electronic orders, from which electronic pairing emerges as a low energy instability. We found a class of RG fixed points characterized by emergent self-similarity, which reflects the non-trivial renormalization of the bare Hubbard interaction in fractal Hofstadter bands. We analyzed two representative instabilities given by the RG: First, for $p/q = 1/2$, we have identified nodal d-wave superconducting instabilities near 1/4 and 3/4 fillings. Second, for $p/q = 1/3, 2/3$, our analysis uncovers the existence of novel chiral topological superconductors near 1/6 and 5/6 fillings. We have characterized these novel phases by a bulk Chern number topological invariant $\mathcal{C} = \pm 6$, which accounts for a chiral phase with 6 net chiral Majorana edge modes, which in principle can be verified in the experiments by measuring thermal Hall coefficient. Moreover, we have found several competing spin and charge density wave orders that break MTG symmetries. Below the transition temperature, these states can coexist with the Hofstadter SC states and can give rise to rich and complex phase diagram.

There is a number of interesting questions that deserve future investigation regarding the nature of pairing in Hofstadter system. First, it would be desirable to find direct connections between the phenomenological Ginzburg-Landau theory established on symmetry grounds and microscopic models describing moiré superlattices subject to a perpendicular magnetic field [270–273], with the purpose of shedding light on realistic parameter regimes conducive to the realization of electronic pairing in moiré Hofstadter bands [1, 2, 45, 47–49, 109]. Second, given that the ground states we find have a large degeneracy of order q, in a real system it is natural to expect domain formation. The study of such domains requires considering gradient terms in the Ginzburg-Landau free energy in Eq. (5.19) that we have ignored in this chapter. Additionally, other spatial defects (of the order parameter and/or of the underlying lattice) such as dislocations and disclinations are possible. It could therefore be

fruitful to study the nature of low energy excitations of Hofstadter superconductors in the presence of such defects to seek possible realizations of defect-bound Majorana fermions [274, 275]. The study of these lattice defects may also shed light on the meaning of "gauging" the magnetic translation group, similar to the approach of gauging internal [276] and spatial symmetries [277]. Another potentially rich scenario could be explored by studying interfaces of Hofstadter superconductors, where different Majorana backscattering may lead to 1D SPT interfaces [278–281] supporting non-Abelian domain walls [282–291].

Furthermore, the presence of a multi-component order parameter characterizing Hofstadter superconductors with phases relations fixed by the magnetic translation group suggests the possibility that this system may support interesting classes of Leggett modes [292]. In the context of pair density waves (PDW), multi-component pairing order parameters are also known to lead to fractional vortices [221, 228, 244, 293–295], as well as induced or vestigial orders like charge density waves or charge 4e condensates [137, 197, 228, 245, 296–304]. This raises the question of what such phenomena may look like in Hofstadter SCs, for example whether vortices trapping a $1/q$ fraction of the flux quantum may be possible [221, 297, 305, 306]. Note that charge 4e, 6e and higher charge Q orders would be classified by irreps of the MTG beyond those considered here, with irrep dimensions given by the greatest common divisor $\gcd(q, Q)$ [220].

In conclusion, the theoretical works presented in this thesis shed new light on novel quantum phenomena in fractal electronic bands. We hope that our theoretical investigations may stimulate the experimental search of exotic quantum critical phenomena and unconventional superconductivity in a widely accessible class of two-dimensional heterostructures. In particular, this study may provide new insights in the pursuit of long-sought topological superconductors - a holy grail of modern physics. The ideas proposed in this thesis may then be a starting point to explore an exciting frontier in

quantum physics.

Bibliography

[1] C. R. Dean, L. Wang, P. Maher, C. Forsythe, F. Ghahari, Y. Gao, J. Katoch, M. Ishigami, P. Moon, M. Koshino, T. Taniguchi, K. Watanabe, K. L. Shepard, J. Hone, and P. Kim, Nature **497**, 598 (2013), number: 7451 Publisher: Nature Publishing Group.

[2] E. M. Spanton, A. A. Zibrov, H. Zhou, T. Taniguchi, K. Watanabe, M. P. Zaletel, and A. F. Young, Science **360**, 62 (2018), publisher: American Association for the Advancement of Science Section: Report.

[3] P. G. Harper, Proceedings of the Physical Society. Section A **68**, 879 (1955).

[4] D. R. Hofstadter, Physical Review B **14**, 2239 (1976), publisher: American Physical Society.

[5] Y. Hasegawa, P. Lederer, T. M. Rice, and P. B. Wiegmann, Physical Review Letters **63**, 907 (1989).

[6] P. W. Anderson, Science **177**, 393 (1972).

[7] L. D. Landau, Physikalische Zeitschrift der Sowjetunion **11**, 26 (1937).

[8] V. Ginzburg and L. Landau, Soviet physics, JETP **20** (1950).

[9] K. v. Klitzing, G. Dorda, and M. Pepper, Physical Review Letters **45**, 494 (1980).

[10] D. C. Tsui, H. L. Stormer, and A. C. Gossard, Physical Review Letters **48**, 1559 (1982).

[11] R. B. Laughlin, Physical Review Letters **50**, 1395 (1983).

[12] R. B. Laughlin, Physical Review B **23**, 5632 (1981).

[13] B. I. Halperin, Physical Review B **25**, 2185 (1982).

[14] M. E. Cage, K. Klitzing, A. Chang, F. Duncan, M. Haldane, R. B. Laughlin, A. Pruisken, and D. Thouless, *The quantum Hall effect* (Springer Science & Business Media, 2012).

[15] M. Stone, *Quantum Hall Effect* (World Scientific, 1992).

[16] X.-G. Wen, International Journal of Modern Physics B **4**, 239 (1990).

[17] X. G. Wen, Physical Review Letters **66**, 802 (1991), publisher: American Physical Society.

[18] X. G. Wen and A. Zee, Physical Review B **46**, 2290 (1992).

[19] X.-G. Wen, Advances in Physics **44**, 405 (1995).

[20] X.-G. Wen, International Scholarly Research Notices **2013** (2013).

[21] X.-G. Wen, Reviews of Modern Physics **89**, 041004 (2017), publisher: American Physical Society.

[22] D. J. Thouless, M. Kohmoto, M. P. Nightingale, and M. den Nijs, Physical Review Letters **49**, 405 (1982), publisher: American Physical Society.

[23] M. V. Berry, Proceedings of the Royal Society of London. A. Mathematical and Physical Sciences **392**, 45 (1984).

[24] P. A. M. Dirac, Proceedings of the Royal Society of London. Series A, Containing Papers of a Mathematical and Physical Character **133**, 60 (1931).

[25] T. T. Wu and C. N. Yang (1969) p. 349.

[26] J. E. Avron, R. Seiler, and B. Simon, Physical Review Letters **51**, 51 (1983).

[27] B. Simon, Physical Review Letters **51**, 2167 (1983), publisher: American Physical Society.

[28] M. Kohmoto, Annals of Physics **160**, 343 (1985).

[29] B. Huckestein, Reviews of Modern Physics **67**, 357 (1995).

[30] A. H. Castro Neto, F. Guinea, N. M. R. Peres, K. S. Novoselov, and A. K. Geim, Reviews of Modern Physics **81**, 109 (2009).

[31] A. K. Geim, science **324**, 1530 (2009).

[32] K. S. Novoselov, A. K. Geim, S. V. Morozov, D. Jiang, M. I. Katsnelson, I. V. Grigorieva, S. V. Dubonos, and A. A. Firsov, Nature **438**, 197 (2005).

[33] K. S. Novoselov, Z. Jiang, Y. Zhang, S. Morozov, H. L. Stormer, U. Zeitler, J. Maan, G. Boebinger, P. Kim, and A. K. Geim, Science **315**, 1379 (2007).

[34] Y. Zhang, Y.-W. Tan, H. L. Stormer, and P. Kim, nature **438**, 201 (2005).

[35] K. I. Bolotin, F. Ghahari, M. D. Shulman, H. L. Stormer, and P. Kim, Nature **462**, 196 EP (2009).

[36] L. F. Mattheiss, Physical Review B **8**, 3719 (1973).

[37] X. Xu, W. Yao, D. Xiao, and T. F. Heinz, Nature Physics **10**, 343 (2014).

[38] S. Manzeli, D. Ovchinnikov, D. Pasquier, O. V. Yazyev, and A. Kis, Nature Reviews Materials **2**, 1 (2017).

[39] L. Landau, Zeitschrift für Physik **64**, 629 (1930).

[40] Y. Liu, N. O. Weiss, X. Duan, H.-C. Cheng, Y. Huang, and X. Duan, Nature Reviews Materials **1**, 1 (2016).

[41] E. Y. Andrei, D. K. Efetov, P. Jarillo-Herrero, A. H. MacDonald, K. F. Mak, T. Senthil, E. Tutuc, A. Yazdani, and A. F. Young, Nature Reviews Materials **6**, 201 (2021).

[42] J. Wang, X. Mu, L. Wang, and M. Sun, Materials Today Physics **9**, 100099 (2019).

[43] S. Carr, S. Fang, and E. Kaxiras, Nature Reviews Materials **5**, 748 (2020).

[44] D. M. Kennes, M. Claassen, L. Xian, A. Georges, A. J. Millis, J. Hone, C. R. Dean, D. Basov, A. N. Pasupathy, and A. Rubio, Nature Physics **17**, 155 (2021).

[45] L. A. Ponomarenko, R. V. Gorbachev, G. L. Yu, D. C. Elias, R. Jalil, A. A. Patel, A. Mishchenko, A. S. Mayorov, C. R. Woods, J. R. Wallbank, M. Mucha-Kruczynski, B. A. Piot, M. Potemski, I. V. Grigorieva, K. S. Novoselov, F. Guinea, V. I. Fal'ko, and A. K. Geim, Nature **497**, 594 (2013).

[46] B. Hunt, J. D. Sanchez-Yamagishi, A. F. Young, M. Yankowitz, B. J. LeRoy, K. Watanabe, T. Taniguchi, P. Moon, M. Koshino, P. Jarillo-Herrero, and R. C. Ashoori, Science **340**, 1427 (2013), publisher: American Association for the Advancement of Science Section: Report.

[47] C. Forsythe, X. Zhou, K. Watanabe, T. Taniguchi, A. Pasupathy, P. Moon, M. Koshino, P. Kim, and C. R. Dean, Nature Nanotechnology **13**, 566 (2018), number: 7 Publisher: Nature Publishing Group.

[48] L. Wang, Y. Gao, B. Wen, Z. Han, T. Taniguchi, K. Watanabe, M. Koshino, J. Hone, and C. R. Dean, Science **350**, 1231 (2015), publisher: American Association for the Advancement of Science Section: Report.

[49] Y. Saito, J. Ge, L. Rademaker, K. Watanabe, T. Taniguchi, D. A. Abanin, and A. F. Young, Nature Physics **17**, 478 (2021), number: 4 Publisher: Nature Publishing Group.

[50] M. C. Geisler, J. H. Smet, V. Umansky, K. von Klitzing, B. Naundorf, R. Ketzmerick, and H. Schweizer, Physical Review Letters **92**, 256801 (2004).

[51] S. Melinte, M. Berciu, C. Zhou, E. Tutuc, S. J. Papadakis, C. Harrison, E. P. De Poortere, M. Wu, P. M. Chaikin, M. Shayegan, R. N. Bhatt, and R. A. Register, Physical Review Letters **92**, 036802 (2004).

[52] T. Feil, K. Výborný, L. Smrčka, C. Gerl, and W. Wegscheider, Physical Review B **75**, 075303 (2007).

[53] H. Miyake, G. A. Siviloglou, C. J. Kennedy, W. C. Burton, and W. Ketterle, Physical Review Letters **111**, 185302 (2013).

[54] M. Aidelsburger, M. Atala, M. Lohse, J. T. Barreiro, B. Paredes, and I. Bloch, Physical Review Letters **111**, 185301 (2013).

[55] S. Powell, R. Barnett, R. Sensarma, and S. Das Sarma, Physical Review A **83**, 013612 (2011), publisher: American Physical Society.

[56] D. Pfannkuche and A. H. MacDonald, Physical Review B **56**, R7100 (1997).

[57] M. Sato, D. Tobe, and M. Kohmoto, Physical Review B **78**, 235322 (2008).

[58] J. Y. Lee, C. Wang, M. P. Zaletel, A. Vishwanath, and Y.-C. He, Physical Review X **8**, 031015 (2018).

[59] J. Herzog-Arbeitman, Z.-D. Song, N. Regnault, and B. A. Bernevig, Physical Review Letters **125**, 236804 (2020).

[60] J. Wang and L. H. Santos, Physical Review Letters **125**, 236805 (2020).

[61] D. Shaffer, J. Wang, and L. H. Santos, Physical Review B **104**, 184501 (2021).

[62] M. M. Maśka, Physical Review B **66**, 054533 (2002), publisher: American Physical Society.

[63] S. Mo and A. SudbÃ¸, Physica C: Superconductivity **383**, 279 (2002).

[64] H. Zhai, R. O. Umucalılar, and M. O. Oktel, Physical Review Letters **104**, 145301 (2010), publisher: American Physical Society.

[65] M. Iskin, Physical Review A **91**, 011601 (2015), publisher: American Physical Society.

[66] G. S. Jeon, J. K. Jain, and C.-X. Liu, Physical Review B **99**, 094509 (2019), publisher: American Physical Society.

[67] R. Sohal and E. Fradkin, Physical Review B **101**, 245154 (2020), publisher: American Physical Society.

[68] J. Schirmer, C.-X. Liu, and J. K. Jain, arXiv:2204.11737 [cond-mat] (2022), arXiv: 2204.11737.

[69] A. Mishra, S. R. Hassan, and R. Shankar, Physical Review B **93**, 125134 (2016), publisher: American Physical Society.

[70] S.-P. Hong and S.-H. Suck Salk, Physical Review B **60**, 9550 (1999), publisher: American Physical Society.

[71] S.-P. Hong, S.-S. Lee, and S.-H. Suck Salk, Physical Review B **62**, 14880 (2000), publisher: American Physical Society.

[72] A. Kol and N. Read, Physical Review B **48**, 8890 (1993).

[73] L. Van Hove, Physical Review **89**, 1189 (1953).

[74] H. J. Schulz, Europhysics Letters (EPL) **4**, 609 (1987), publisher: IOP Publishing.

[75] I. Dzyaloshinski, JETP Lett **46** (1987).

[76] R. S. Markiewicz, Journal of Physics and Chemistry of Solids **58**, 1179 (1997).

[77] R. Nandkishore, L. S. Levitov, and A. V. Chubukov, Nature Physics **8**, 158 (2012).

[78] W.-S. Wang, Y.-Y. Xiang, Q.-H. Wang, F. Wang, F. Yang, and D.-H. Lee, Physical Review B **85**, 035414 (2012).

[79] M. L. Kiesel, C. Platt, W. Hanke, D. A. Abanin, and R. Thomale, Physical Review B **86**, 020507 (2012).

[80] J. González, Physical Review B **78**, 205431 (2008).

[81] H. Isobe, N. F. Yuan, and L. Fu, Physical Review X **8**, 041041 (2018), publisher: American Physical Society.

[82] Y. Sherkunov and J. J. Betouras, Physical Review B **98**, 205151 (2018).

[83] C.-C. Liu, L.-D. Zhang, W.-Q. Chen, and F. Yang, Physical Review Letters **121**, 217001 (2018).

[84] D. M. Kennes, J. Lischner, and C. Karrasch, Physical Review B **98**, 241407 (2018).

[85] Y.-Z. You and A. Vishwanath, npj Quantum Materials **4**, 16 (2019).

[86] Y.-P. Lin and R. M. Nandkishore, Physical Review B **102**, 245122 (2020).

[87] Y.-T. Hsu, F. Wu, and S. Das Sarma, Physical Review B **102**, 085103 (2020).

[88] L. Classen, A. V. Chubukov, C. Honerkamp, and M. M. Scherer, Physical Review B **102**, 125141 (2020), publisher: American Physical Society.

[89] D. V. Chichinadze, L. Classen, and A. V. Chubukov, Physical Review B **101**, 224513 (2020).

[90] M. Y. Azbel, Sov. Phys. JETP **19**, 634 (1964).

[91] J. Zak, Physical Review **134**, A1602 (1964), publisher: American Physical Society.

[92] J. Zak, Physical Review **134**, A1607 (1964), publisher: American Physical Society.

[93] E. Brown, Physical Review **133**, A1038 (1964), publisher: American Physical Society.

[94] J. Herzog-Arbeitman, Z.-D. Song, N. Regnault, and B. A. Bernevig, Physical Review Letters **125**, 236804 (2020).

[95] E. M. Spanton, A. A. Zibrov, H. Zhou, T. Taniguchi, K. Watanabe, M. P. Zaletel, and A. F. Young, Science **360**, 62 (2018).

[96] A. L. Sharpe, E. J. Fox, A. W. Barnard, J. Finney, K. Watanabe, T. Taniguchi, M. A. Kastner, and D. Goldhaber-Gordon, Science **365**, 605 (2019), publisher: American Association for the Advancement of Science.

[97] M. Serlin, C. L. Tschirhart, H. Polshyn, Y. Zhang, J. Zhu, K. Watanabe, T. Taniguchi, L. Balents, and A. F. Young, Science **367**, 900 (2020), publisher: American Association for the Advancement of Science.

[98] Y. Saito, J. Ge, L. Rademaker, K. Watanabe, T. Taniguchi, D. A. Abanin, and A. F. Young, Nature Physics **17**, 478 (2021).

[99] Y. Xie, A. T. Pierce, J. M. Park, D. E. Parker, E. Khalaf, P. Ledwith, Y. Cao, S. H. Lee, S. Chen, P. R. Forrester, K. Watanabe, T. Taniguchi, A. Vishwanath, P. Jarillo-Herrero, and A. Yacoby, Nature **600**, 439 (2021).

[100] K. P. Nuckolls, M. Oh, D. Wong, B. Lian, K. Watanabe, T. Taniguchi, B. A. Bernevig, and A. Yazdani, Nature **588**, 610 (2020), number: 7839 Publisher: Nature Publishing Group.

[101] S. Wu, Z. Zhang, K. Watanabe, T. Taniguchi, and E. Y. Andrei, Nature Materials , 1 (2021), publisher: Nature Publishing Group.

[102] I. Das, X. Lu, J. Herzog-Arbeitman, Z.-D. Song, K. Watanabe, T. Taniguchi, B. A. Bernevig, and D. K. Efetov, Nature Physics **17**, 710 (2021), number: 6 Publisher: Nature Publishing Group.

[103] Y. Choi, H. Kim, Y. Peng, A. Thomson, C. Lewandowski, R. Polski, Y. Zhang, H. S. Arora, K. Watanabe, T. Taniguchi, J. Alicea, and S. Nadj-Perge, Nature **589**, 536 (2021).

[104] J. M. Park, Y. Cao, K. Watanabe, T. Taniguchi, and P. Jarillo-Herrero, Nature **592**, 43 (2021), number: 7852 Publisher: Nature Publishing Group.

[105] P. Stepanov, M. Xie, T. Taniguchi, K. Watanabe, X. Lu, A. H. MacDonald, B. A. Bernevig, and D. K. Efetov, Physical Review Letters **127**, 197701 (2021).

[106] A. T. Pierce, Y. Xie, J. M. Park, E. Khalaf, S. H. Lee, Y. Cao, D. E. Parker, P. R. Forrester, S. Chen, K. Watanabe, T. Taniguchi, A. Vishwanath, P. Jarillo-Herrero, and A. Yacoby, Nature Physics **17**, 1210 (2021), number: 11 Publisher: Nature Publishing Group.

[107] J. Yu, B. A. Foutty, Z. Han, M. E. Barber, Y. Schattner, K. Watanabe, T. Taniguchi, P. Phillips, Z.-X. Shen, S. A. Kivelson, and B. E. Feldman, (2021), 10.48550/ARXIV.2108.00009.

[108] C. R. Dean, L. Wang, P. Maher, C. Forsythe, F. Ghahari, Y. Gao, J. Katoch, M. Ishigami, P. Moon, M. Koshino, T. Taniguchi, K. Watanabe, K. L. Shepard, J. Hone, and P. Kim, Nature **497**, 598 EP (2013).

[109] B. Hunt, J. D. Sanchez-Yamagishi, A. F. Young, M. Yankowitz, B. J. LeRoy, K. Watanabe, T. Taniguchi, P. Moon, M. Koshino, P. Jarillo-Herrero, and R. C. Ashoori, Science **340**, 1427 (2013).

[110] C. Forsythe, X. Zhou, K. Watanabe, T. Taniguchi, A. Pasupathy, P. Moon, M. Koshino, P. Kim, and C. R. Dean, Nature nanotechnology **13**, 566 (2018).

[111] T. Neupert, L. Santos, C. Chamon, and C. Mudry, Physical Review Letters **106**, 236804 (2011).

[112] D. N. Sheng, Z.-C. Gu, K. Sun, and L. Sheng, Nature Communications **2**, 389 EP (2011).

[113] E. Tang, J.-W. Mei, and X.-G. Wen, Physical Review Letters **106**, 236802 (2011).

[114] K. Sun, Z. Gu, H. Katsura, and S. Das Sarma, Physical Review Letters **106**, 236803 (2011).

[115] N. Regnault and B. A. Bernevig, Physical Review X **1**, 021014 (2011).

[116] S. A. Parameswaran, R. Roy, and S. L. Sondhi, Comptes Rendus Physique **14**, 816 (2013).

[117] G. Möller and N. R. Cooper, Physical Review Letters **115**, 126401 (2015).

[118] G. Murthy and R. Shankar, Physical Review B **86**, 195146 (2012).

[119] R. Sohal, L. H. Santos, and E. Fradkin, Physical Review B **97**, 125131 (2018).

[120] B. Andrews, T. Neupert, and G. Möller, Physical Review B **104**, 125107 (2021).

[121] S. Kobayashi, K. Shiozaki, Y. Tanaka, and M. Sato, Physical Review B **90**, 024516 (2014), publisher: American Physical Society.

[122] Y. Zhao, A. P. Schnyder, and Z. Wang, Physical Review Letters **116**, 156402 (2016), publisher: American Physical Society.

[123] D. F. Agterberg, P. M. R. Brydon, and C. Timm, Physical Review Letters **118**, 127001 (2017), publisher: American Physical Society.

[124] P. M. R. Brydon, D. F. Agterberg, H. Menke, and C. Timm, Physical Review B **98**, 224509 (2018), publisher: American Physical Society.

[125] L. H. Santos, Y. Wang, and E. Fradkin, Physical Review X **9**, 021047 (2019).

[126] N. F. Q. Yuan and L. Fu, Physical Review B **97**, 115139 (2018), publisher: American Physical Society.

[127] S. Sumita, T. Nomoto, K. Shiozaki, and Y. Yanase, Physical Review B **99**, 134513 (2019), publisher: American Physical Society.

[128] H. Menke, C. Timm, and P. M. R. Brydon, Physical Review B **100**, 224505 (2019), publisher: American Physical Society.

[129] J. M. Link and I. F. Herbut, Physical Review Letters **125**, 237004 (2020), publisher: American Physical Society.

[130] C. J. Lapp, G. Börner, and C. Timm, Physical Review B **101**, 024505 (2020), publisher: American Physical Society.

[131] D. Shaffer, J. Kang, F. J. Burnell, and R. M. Fernandes, Physical Review B **101**, 224503 (2020), publisher: American Physical Society.

[132] Z. Zhu, M. Papaj, X.-A. Nie, H.-K. Xu, Y.-S. Gu, X. Yang, D. Guan, S. Wang, Y. Li, C. Liu, J. Luo, Z.-A. Xu, H. Zheng, L. Fu, and J.-F. Jia, arXiv:2010.02216 [cond-mat] (2020), arXiv: 2010.02216.

[133] N. Read and D. Green, Physical Review B **61**, 10267 (2000).

[134] J. Orenstein and A. Millis, Science **288**, 468 (2000).

[135] W. Hofstetter, J. I. Cirac, P. Zoller, E. Demler, and M. D. Lukin, Physical Review Letters **89**, 220407 (2002).

[136] G. Blatter, M. V. Feigel'man, V. B. Geshkenbein, A. I. Larkin, and V. M. Vinokur, Reviews of Modern Physics **66**, 1125 (1994), publisher: American Physical Society.

[137] E. Berg, E. Fradkin, and S. A. Kivelson, Nature Physics **5**, 830 (2009), number: 11 Publisher: Nature Publishing Group.

[138] P. A. Lee, N. Nagaosa, and X.-G. Wen, Reviews of Modern Physics **78**, 17 (2006).

[139] O. Can, T. Tummuru, R. P. Day, I. Elfimov, A. Damascelli, and M. Franz, Nature Physics **17**, 519 (2021), number: 4 Publisher: Nature Publishing Group.

[140] Y. Yu, L. Ma, P. Cai, R. Zhong, C. Ye, J. Shen, G. D. Gu, X. H. Chen, and Y. Zhang, Nature **575**, 156 (2019), number: 7781 Publisher: Nature Publishing Group.

[141] B. Keimer, S. A. Kivelson, M. R. Norman, S. Uchida, and J. Zaanen, Nature **518**, 179 (2015).

[142] R. Shankar, Reviews of Modern Physics **66**, 129 (1994).

[143] J. Polchinski, arXiv preprint hep-th/9210046 (1992).

[144] S. Maiti and A. V. Chubukov, AIP Conference Proceedings **1550**, 3 (2013), publisher: American Institute of Physics.

[145] Z. Tešanović, M. Rasolt, and L. Xing, Physical Review Letters **63**, 2425 (1989), publisher: American Physical Society.

[146] H. Akera, A. H. MacDonald, S. M. Girvin, and M. R. Norman, Physical Review Letters **67**, 2375 (1991), publisher: American Physical Society.

[147] Z. Tešanović, M. Rasolt, and L. Xing, Physical Review B **43**, 288 (1991), publisher: American Physical Society.

[148] A. K. Rajagopal and R. Vasudevan, Physical Review B **44**, 2807 (1991), publisher: American Physical Society.

[149] A. H. MacDonald, H. Akera, and M. R. Norman, Physical Review B **45**, 10147 (1992), publisher: American Physical Society.

[150] M. R. Norman, H. Akera, and A. H. MacDonald, Physica C: Superconductivity **196**, 43 (1992).

[151] M. Rasolt and Z. Tešanović, Reviews of Modern Physics **64**, 709 (1992), publisher: American Physical Society.

[152] A. H. MacDonald, H. Akera, and M. R. Norman, Australian Journal of Physics **46**, 333 (1993), publisher: CSIRO PUBLISHING.

[153] J. C. Ryan and A. K. Rajagopal, Physical Review B **47**, 8843 (1993), publisher: American Physical Society.

[154] S. c. v. Dukan and Z. Tešanović, Physical Review B **56**, 838 (1997).

[155] T. Ueta and T. Hioki, Journal of Superconductivity and Novel Magnetism **26**, 1921 (2013).

[156] P. Scherpelz, D. Wulin, B. c. v. Šopík, K. Levin, and A. K. Rajagopal, Physical Review B **87**, 024516 (2013).

[157] N. Furukawa, T. M. Rice, and M. Salmhofer, Physical Review Letters **81**, 3195 (1998).

[158] R. Rammal, Journal de Physique **46**, 1345 (1985).

[159] C. Kreft and R. Seiler, Journal of Mathematical Physics **37**, 5207 (1996).

[160] J. E. Avron, O. Kenneth, and G. Yehoshua, Journal of Physics A: Mathematical and Theoretical **47**, 185202 (2014).

[161] A. Agazzi, J.-P. Eckmann, and G. M. Graf, Journal of Statistical Physics **156**, 417 (2014).

[162] F. D. M. Haldane, Physical Review Letters **61**, 2015 (1988).

[163] J. K. Jain, Physical Review Letters **63**, 199 (1989).

[164] A. López and E. Fradkin, Physical Review B **44**, 5246 (1991).

[165] B. I. Halperin, P. A. Lee, and N. Read, Physical Review B **47**, 7312 (1993).

[166] Z. Liu, E. J. Bergholtz, H. Fan, and A. M. Läuchli, Physical Review Letters **109**, 186805 (2012).

[167] Y.-L. Wu, B. A. Bernevig, and N. Regnault, Physical Review B **85**, 075116 (2012).

[168] A. M. Läuchli, Z. Liu, E. J. Bergholtz, and R. Moessner, Physical Review Letters **111**, 126802 (2013).

[169] Y.-M. Lu, Y. Ran, and M. Oshikawa, Annals of Physics **413**, 168060 (2020).

[170] J. K. Jain, S. A. Kivelson, and N. Trivedi, Physical Review Letters **64**, 1297 (1990).

[171] S. Kivelson, D.-H. Lee, and S.-C. Zhang, Physical Review B **46**, 2223 (1992).

[172] M. Gibertini, A. Singha, V. Pellegrini, M. Polini, G. Vignale, A. Pinczuk, L. N. Pfeiffer, and K. W. West, Physical Review B **79**, 241406 (2009).

[173] A. Singha, M. Gibertini, B. Karmakar, S. Yuan, M. Polini, G. Vignale, M. I. Katsnelson, A. Pinczuk, L. N. Pfeiffer, K. W. West, and V. Pellegrini, Science **332**, 1176 (2011).

[174] A. Soibel, U. Meirav, D. Mahalu, and H. Shtrikman, Semiconductor Science and Technology **11**, 1756 (1996).

[175] L. Nádvorník, M. Orlita, N. A. Goncharuk, L. Smrčka, V. Novák, V. Jurka, K. Hruška, Z. Výborný, Z. R. Wasilewski, M. Potemski, and K. Výborný, New Journal of Physics **14**, 053002 (2012).

[176] S. Wang, D. Scarabelli, Y. Y. Kuznetsova, S. J. Wind, A. Pinczuk, V. Pellegrini, M. J. Manfra, G. C. Gardner, L. N. Pfeiffer, and K. W. West, Applied Physics Letters **109**, 113101 (2016).

[177] S. Wang, D. Scarabelli, L. Du, Y. Y. Kuznetsova, L. N. Pfeiffer, K. W. West, G. C. Gardner, M. J. Manfra, V. Pellegrini, S. J. Wind, and A. Pinczuk, Nature Nanotechnology **13**, 29 (2018).

[178] B. Andrei Bernevig, T. L. Hughes, S.-c. Zhang, H.-d. Chen, and C. Wu, International Journal of Modern Physics B **20**, 3257 (2006).

[179] D. J. Thouless, Physical Review B **28**, 4272 (1983).

[180] J.-W. Rhim and K. Park, Physical Review B **86**, 235411 (2012).

[181] I. N. Karnaukhov, Physics Letters A **383**, 2114 (2019).

[182] A. Das, R. K. Kaul, and G. Murthy, Physical Review B **101**, 165416 (2020).

[183] Y. Hasegawa, R. Konno, H. Nakano, and M. Kohmoto, Physical Review B **74**, 033413 (2006).

[184] B. Wunsch, F. Guinea, and F. Sols, New Journal of Physics **10**, 103027 (2008).

[185] A. N. Redlich, Physical Review Letters **52**, 18 (1984).

[186] See Supplemental Material for details on further examples of the relation between the vHs energy scale and topological phase transitions.

[187] T. Fukui, Y. Hatsugai, and H. Suzuki, Journal of the Physical Society of Japan **74**, 1674 (2005).

[188] D. Shaffer, J. Wang, and L. H. Santos, arXiv preprint arXiv:2204.13116 (2022).

[189] D. V. Efremov, A. Shtyk, A. W. Rost, C. Chamon, A. P. Mackenzie, and J. J. Betouras, Physical Review Letters **123**, 207202 (2019).

[190] N. F. Q. Yuan, H. Isobe, and L. Fu, Nature Communications **10**, 5769 (2019).

[191] W. Meissner and R. Ochsenfeld, Naturwissenschaften **21**, 787 (1933).

[192] J. Bardeen, L. N. Cooper, and J. R. Schrieffer, Physical Review **108**, 1175 (1957).

[193] M. Sigrist and K. Ueda, Reviews of Modern Physics **63**, 239 (1991), publisher: American Physical Society.

[194] M. R. Norman, Science **332**, 196 (2011).

[195] M. J. Park, Y. B. Kim, and S. Lee, arXiv:2007.16205 [cond-mat] (2020), arXiv: 2007.16205.

[196] Y. Cao, J. M. Park, K. Watanabe, T. Taniguchi, and P. Jarillo-Herrero, arXiv:2103.12083 [cond-mat] (2021), arXiv: 2103.12083.

[197] R. M. Fernandes and L. Fu, Physical Review Letters **127**, 047001 (2021), publisher: American Physical Society.

[198] E. Dagotto, Reviews of Modern Physics **66**, 763 (1994).

[199] L. W. Gruenberg and L. Gunther, Physical Review **176**, 606 (1968), publisher: American Physical Society.

[200] N. Read and D. Green, Physical Review B **61**, 10267 (2000).

[201] A. Y. Kitaev, Physics-Uspekhi (Suppl.) **171**, 131 (2001).

[202] M. Sato and Y. Ando, Reports on Progress in Physics **80**, 076501 (2017), publisher: IOP Publishing.

[203] S. Ono, Y. Yanase, and H. Watanabe, Physical Review Research **1**, 013012 (2019).

[204] X.-L. Qi, T. L. Hughes, and S.-C. Zhang, Physical Review B **81**, 134508 (2010), publisher: American Physical Society.

[205] J. Falson, D. Tabrea, D. Zhang, I. Sodemann, Y. Kozuka, A. Tsukazaki, M. Kawasaki, K. von Klitzing, and J. H. Smet, Science Advances **4** (2018), 10.1126/sciadv.aat8742.

[206] R. L. Willett, C. Nayak, K. Shtengel, L. N. Pfeiffer, and K. W. West, Physical Review Letters **111**, 186401 (2013).

[207] R. L. Willett, L. N. Pfeiffer, and K. W. West, Physical Review B **82**, 205301 (2010).

[208] R. L. Willett, L. N. Pfeiffer, and K. W. West, Proceedings of the National Academy of Sciences **106**, 8853 (2009).

[209] M. Dolev, M. Heiblum, V. Umansky, A. Stern, and D. Mahalu, Nature **452**, 829 (2008).

[210] P. Bonderson, A. Kitaev, and K. Shtengel, Physical Review Letters **96**, 016803 (2006).

[211] C. Wang, A. Vishwanath, and B. I. Halperin, Physical Review B **98**, 045112 (2018).

[212] K. A. Schreiber, N. Samkharadze, G. C. Gardner, R. R. Biswas, M. J. Manfra, and G. A. Csáthy, Physical Review B **96**, 041107 (2017).

[213] Y. Liu, S. Hasdemir, M. Shayegan, L. N. Pfeiffer, K. W. West, and K. W. Baldwin, Physical Review B **88**, 035307 (2013).

[214] J. Xia, V. Cvicek, J. P. Eisenstein, L. N. Pfeiffer, and K. W. West, Physical Review Letters **105**, 176807 (2010).

[215] X. Shi, W. Pan, K. W. Baldwin, K. W. West, L. N. Pfeiffer, and D. C. Tsui, Physical Review B **91**, 125308 (2015).

[216] B. Friess, V. Umansky, L. Tiemann, K. von Klitzing, and J. H. Smet, Physical Review Letters **113**, 076803 (2014).

[217] W. Pan, J. S. Xia, V. Shvarts, D. E. Adams, H. L. Störmer, D. C. Tsui, L. N. Pfeiffer, K. W. Baldwin, and K. W. West, Physical Review Letters **83**, 3530 (1999).

[218] W. Pan, R. R. Du, H. L. Störmer, D. C. Tsui, L. N. Pfeiffer, K. W. Baldwin, and K. W. West, Physical Review Letters **83**, 820 (1999).

[219] G. Moore and N. Read, Nuclear Physics B **360**, 362 (1991).

[220] W. Florek, Physical Review B **55**, 1449 (1997).

[221] L. Balents, L. Bartosch, A. Burkov, S. Sachdev, and K. Sengupta, Physical Review B **71**, 144508 (2005), publisher: American Physical Society.

[222] S. Powell, R. Barnett, R. Sensarma, and S. Das Sarma, Physical Review Letters **104**, 255303 (2010), publisher: American Physical Society.

[223] S. S. Natu, E. J. Mueller, and S. Das Sarma, Physical Review A **93**, 063610 (2016), publisher: American Physical Society.

[224] Y.-F. Song and S.-J. Yang, Journal of Physics B: Atomic, Molecular and Optical Physics **52**, 118001 (2019), publisher: IOP Publishing.

[225] M. Iskin, Physical Review A **91**, 011601 (2015), publisher: American Physical Society.

[226] M. Iskin, Physical Review A **91**, 053606 (2015), publisher: American Physical Society.

[227] R. O. Umucalılar and M. Iskin, Physical Review A **94**, 023611 (2016), publisher: American Physical Society.

[228] D. F. Agterberg, J. S. Davis, S. D. Edkins, E. Fradkin, D. J. Van Harlingen, S. A. Kivelson, P. A. Lee, L. Radzihovsky, J. M. Tranquada, and Y. Wang, Annual Review of Condensed Matter Physics **11**, 231 (2020), publisher: Annual Reviews.

[229] B. Zocher and B. Rosenow, Physical Review B **93**, 214504 (2016), publisher: American Physical Society.

[230] M. R. Sahu, X. Liu, A. K. Paul, S. Das, P. Raychaudhuri, J. Jain, and A. Das, Physical Review Letters **121**, 086809 (2018), publisher: American Physical Society.

[231] J. Schirmer, R. Kumar, V. Bagwe, P. Raychaudhuri, T. Taniguchi, K. Watanabe, C.-X. Liu, A. Das, and J. K. Jain, EPL (Europhysics Letters) **132**, 37002 (2020), publisher: IOP Publishing.

[232] G. Chaudhary and A. H. MacDonald, Physical Review B **101**, 024516 (2020), publisher: American Physical Society.

[233] G. Chaudhary, A. H. MacDonald, and M. R. Norman, Physical Review Research **3**, 033260 (2021).

[234] C. Weeks, G. Rosenberg, B. Seradjeh, and M. Franz, Nature Physics **3**, 796 (2007), publisher: Springer Nature.

[235] L. Wang, H.-H. Hung, and M. Troyer, Physical Review B **90**, 205111 (2014), publisher: American Physical Society.

[236] S. Peotta and P. Törmä, Nature Communications **6**, 8944 (2015), number: 1 Publisher: Nature Publishing Group.

[237] R. O. Umucalılar and M. Iskin, Physical Review Letters **119**, 085301 (2017), publisher: American Physical Society.

[238] M. Iskin, Physical Review A **97**, 013618 (2018), publisher: American Physical Society.

[239] M. Iskin, Physical Review A **99**, 023608 (2019), publisher: American Physical Society.

[240] P. Fulde and R. A. Ferrell, Physical Review **135**, A550 (1964).

[241] A. Larkin and I. Ovchinnikov, Soviet Physics-JETP **20**, 762 (1965).

[242] H. Hu and X.-J. Liu, Physical Review A **73**, 051603 (2006).

[243] D. F. Agterberg and R. P. Kaur, Physical Review B **75**, 064511 (2007), publisher: American Physical Society.

[244] L. Radzihovsky and A. Vishwanath, Physical Review Letters **103**, 010404 (2009), publisher: American Physical Society.

[245] L. Radzihovsky, Physical Review A **84**, 023611 (2011), publisher: American Physical Society.

[246] G. Y. Cho, J. H. Bardarson, Y.-M. Lu, and J. E. Moore, Physical Review B **86**, 214514 (2012), publisher: American Physical Society.

[247] Z. Zheng, M. Gong, X. Zou, C. Zhang, and G. Guo, Physical Review A **87**, 031602 (2013), publisher: American Physical Society.

[248] T. H. Jones and N. B. Willms, Journal of Physics: Conference Series **1047**, 012016 (2018), publisher: IOP Publishing.

[249] M. P. A. Fisher, Physical Review Letters **62**, 1415 (1989), publisher: American Physical Society.

[250] D. A. Huse and H. S. Seung, Physical Review B **42**, 1059 (1990), publisher: American Physical Society.

[251] B. Jacobsen, K. Saunders, L. Radzihovsky, and J. Toner, Physical Review Letters **83**, 1363 (1999), publisher: American Physical Society.

[252] L. Radzihovsky and J. Toner, Physical Review B **60**, 206 (1999), publisher: American Physical Society.

[253] K. Saunders, B. Jacobsen, L. Radzihovsky, and J. Toner, Journal of Physics: Condensed Matter **12**, A215 (2000), publisher: IOP Publishing.

[254] L. Radzihovsky, Physical Review B **104**, 024510 (2021).

[255] X. Chen, Z.-C. Gu, Z.-X. Liu, and X.-G. Wen, Physical Review B **87**, 155114 (2013), publisher: American Physical Society.

[256] T. Senthil, Annual Review of Condensed Matter Physics **6**, 299 (2015), https://doi.org/10.1146/annurev-conmatphys-031214-014740 .

[257] C.-K. Chiu, J. C. Teo, A. P. Schnyder, and S. Ryu, Reviews of Modern Physics **88**, 035005 (2016), publisher: American Physical Society.

[258] A. Altland and M. R. Zirnbauer, Physical Review B **55**, 1142 (1997), publisher: American Physical Society.

[259] S. Ryu, A. P. Schnyder, A. Furusaki, and A. W. W. Ludwig, New Journal of Physics **12**, 065010 (2010), publisher: IOP Publishing.

[260] A. W. W. Ludwig, Physica Scripta **T168**, 014001 (2015), publisher: IOP Publishing.

[261] T. L. Hughes, E. Prodan, and B. A. Bernevig, Physical Review B **83**, 245132 (2011), publisher: American Physical Society.

[262] C.-K. Chiu, H. Yao, and S. Ryu, Physical Review B **88**, 075142 (2013), publisher: American Physical Society.

[263] C.-K. Chiu and A. P. Schnyder, Physical Review B **90**, 205136 (2014), publisher: American Physical Society.

[264] K. Shiozaki and M. Sato, Physical Review B **90**, 165114 (2014), publisher: American Physical Society.

[265] E. Cornfeld and A. Chapman, Physical Review B **99**, 075105 (2019), publisher: American Physical Society.

[266] M. Cheng, M. Zaletel, M. Barkeshli, A. Vishwanath, and P. Bonderson, Physical Review X **6**, 041068 (2016), publisher: American Physical Society.

[267] Y.-M. Lu, Y. Ran, and M. Oshikawa, Annals of Physics **413**, 168060 (2020).

[268] S. Matsuura, P.-Y. Chang, A. P. Schnyder, and S. Ryu, New Journal of Physics **15**, 065001 (2013), publisher: IOP Publishing.

[269] Y. X. Zhao and Z. D. Wang, Physical Review Letters **110**, 240404 (2013), publisher: American Physical Society.

[270] J. Kang and O. Vafek, Physical Review X **8**, 031088 (2018), publisher: American Physical Society.

[271] M. Koshino, N. F. Yuan, T. Koretsune, M. Ochi, K. Kuroki, and L. Fu, Physical Review X **8**, 031087 (2018), publisher: American Physical Society.

[272] N. F. Q. Yuan and L. Fu, Physical Review B **98**, 045103 (2018), publisher: American Physical Society.

[273] B. Andrews and A. Soluyanov, Physical Review B **101**, 235312 (2020), publisher: American Physical Society.

[274] J. C. Y. Teo and T. L. Hughes, Physical Review Letters **111**, 047006 (2013).

[275] W. A. Benalcazar, J. C. Y. Teo, and T. L. Hughes, Physical Review B **89**, 224503 (2014).

[276] M. Levin and Z.-C. Gu, Physical Review B **86**, 115109 (2012).

[277] R. Thorngren and D. V. Else, Physical Review X **8**, 011040 (2018).

[278] L. H. Santos and T. L. Hughes, Physical Review Letters **118**, 136801 (2017).

[279] L. H. Santos, J. Cano, M. Mulligan, and T. L. Hughes, Physical Review B **98**, 075131 (2018).

[280] L. H. Santos, Physical Review Research **2**, 013232 (2020).

[281] R. Sohal, B. Han, L. H. Santos, and J. C. Y. Teo, Physical Review B **102**, 045102 (2020).

[282] J. Alicea and P. Fendley, Annual Review of Condensed Matter Physics **7**, 119 (2016).

[283] M. Barkeshli and X.-L. Qi, Physical Review X **2**, 031013 (2012).

[284] N. H. Lindner, E. Berg, G. Refael, and A. Stern, Physical Review X **2**, 041002 (2012).

[285] D. J. Clarke, J. Alicea, and K. Shtengel, Nature Communications **4**, 1348 EP (2013).

[286] M. Cheng, Physical Review B **86**, 195126 (2012).

[287] A. Vaezi, Physical Review B **87**, 035132 (2013).

[288] M. Barkeshli, C.-M. Jian, and X.-L. Qi, Physical Review B **87**, 045130 (2013).

[289] M. Barkeshli, C.-M. Jian, and X.-L. Qi, Physical Review B **88**, 241103 (2013).

[290] R. S. K. Mong, D. J. Clarke, J. Alicea, N. H. Lindner, P. Fendley, C. Nayak, Y. Oreg, A. Stern, E. Berg, K. Shtengel, and M. P. A. Fisher, Physical Review X **4**, 011036 (2014).

[291] M. N. Khan, J. C. Y. Teo, and T. L. Hughes, Physical Review B **90**, 235149 (2014).

[292] A. J. Leggett, Progress of Theoretical Physics **36**, 901 (1966), https://academic.oup.com/ptp/article-pdf/36/5/901/5256693/36-5-901.pdf .

[293] S. B. Chung, H. Bluhm, and E.-A. Kim, Physical Review Letters **99**, 197002 (2007), publisher: American Physical Society.

[294] D. F. Agterberg and H. Tsunetsugu, Nature Physics **4**, 639 (2008), number: 8 Publisher: Nature Publishing Group.

[295] R. C. Regan, J. J. Wiman, and J. A. Sauls, Physical Review B **104**, 024513 (2021).

[296] G. Röpke, A. Schnell, P. Schuck, and P. Nozières, Physical Review Letters **80**, 3177 (1998).

[297] E. Babaev, Nuclear Physics B **686**, 397 (2004).

[298] C. Wu, Physical Review Letters **95**, 266404 (2005), publisher: American Physical Society.

[299] D. F. Agterberg, M. Geracie, and H. Tsunetsugu, Physical Review B **84**, 014513 (2011), publisher: American Physical Society.

[300] E.-G. Moon, Physical Review B **85**, 245123 (2012), publisher: American Physical Society.

[301] P. A. Lee, Physical Review X **4**, 031017 (2014), publisher: American Physical Society.

[302] E. Fradkin, S. A. Kivelson, and J. M. Tranquada, Reviews of Modern Physics **87**, 457 (2015), publisher: American Physical Society.

[303] Y.-F. Jiang, Z.-X. Li, S. A. Kivelson, and H. Yao, Physical Review B **95**, 241103 (2017), publisher: American Physical Society.

[304] R. M. Fernandes, P. P. Orth, and J. Schmalian, Annual Review of Condensed Matter Physics **10**, 133 (2019), publisher: Annual Reviews.

[305] E. Babaev, Physical Review Letters **89**, 067001 (2002), publisher: American Physical Society.

[306] J. Smiseth, E. Smørgrav, E. Babaev, and A. Sudbø, Physical Review B **71**, 214509 (2005).

[307] G. Chaudhary, A. H. MacDonald, and M. R. Norman, Physical Review Research **3**, 033260 (2021).

[308] Y. Cao, V. Fatemi, S. Fang, K. Watanabe, T. Taniguchi, E. Kaxiras, and P. Jarillo-Herrero, Nature **556**, 43 (2018), number: 7699 Publisher: Nature Publishing Group.

[309] I. Das, C. Shen, A. Jaoui, J. Herzog-Arbeitman, A. Chew, C.-W. Cho, K. Watanabe, T. Taniguchi, B. A. Piot, B. A. Bernevig, and D. K. Efetov, (2021), 10.48550/ARXIV.2111.11341.

[310] A. A. Abrikosov, Sov. Phys. JETP **5**, 1174 (1957).

[311] G. Möller and N. R. Cooper, Physical Review Letters **103**, 105303 (2009).

[312] T. Scaffidi and S. H. Simon, Physical Review B **90**, 115132 (2014), publisher: American Physical Society.

[313] J. Motruk, M. P. Zaletel, R. S. K. Mong, and F. Pollmann, Physical Review B **93**, 155139 (2016), publisher: American Physical Society.

[314] J. Y. Lee, C. Wang, M. P. Zaletel, A. Vishwanath, and Y.-C. He, Physical Review X **8**, 031015 (2018).

[315] B. Andrews and G. MÃ¶ller, Physical Review B **97**, 035159 (2018), publisher: American Physical Society.

[316] E. J. Mueller, Physical Review A **70**, 041603 (2004), publisher: American Physical Society.

[317] M. Lewenstein, A. Sanpera, V. Ahufinger, B. Damski, A. Sen(De), and U. Sen, Advances in Physics **56**, 243 (2007), publisher: Taylor & Francis _eprint: https://doi.org/10.1080/00018730701223200.

[318] N. Goldman, I. Satija, P. Nikolic, A. Bermudez, M. A. Martin-Delgado, M. Lewenstein, and I. B. Spielman, Physical Review Letters **105**, 255302 (2010), publisher: American Physical Society.

[319] F. Gerbier and J. Dalibard, New Journal of Physics **12**, 033007 (2010), publisher: IOP Publishing.

[320] M. Aidelsburger, M. Atala, S. Nascimbène, S. Trotzky, Y.-A. Chen, and I. Bloch, Physical Review Letters **107**, 255301 (2011).

[321] P. Hauke, O. Tieleman, A. Celi, C. Ölschläger, J. Simonet, J. Struck, M. Weinberg, P. Windpassinger, K. Sengstock, M. Lewenstein, and A. Eckardt, Physical Review Letters **109**, 145301 (2012).

[322] A. Celi, P. Massignan, J. Ruseckas, N. Goldman, I. B. Spielman, G. Juzeliūnas, and M. Lewenstein, Physical Review Letters **112**, 043001 (2014).

[323] M. Niemeyer, J. K. Freericks, and H. Monien, Physical Review B **60**, 2357 (1999), publisher: American Physical Society.

[324] A. S. Sørensen, E. Demler, and M. D. Lukin, Physical Review Letters **94**, 086803 (2005).

[325] M. Hafezi, A. S. SÃ¸rensen, E. Demler, and M. D. Lukin, Physical Review A **76**, 023613 (2007), publisher: American Physical Society.

[326] M. O. Oktel, M. Niţă, and B. Tanatar, Physical Review B **75**, 045133 (2007).

[327] P. P. Orth, D. Cocks, S. Rachel, M. Buchhold, K. L. Hur, and W. Hofstetter, Journal of Physics B: Atomic, Molecular and Optical Physics **46**, 134004 (2013), publisher: IOP Publishing.

[328] C. Zeng, T. Stanescu, C. Zhang, V. Scarola, and S. Tewari, Physical Review Letters **123**, 060402 (2019), publisher: American Physical Society.

[329] L. Lin and X. Wu, ESAIM: Mathematical Modelling and Numerical Analysis **55**, 763 (2021), number: 3 Publisher: EDP Sciences.

[330] A. Bille, R. A. Klemm, and K. Scharnberg, Physical Review B **64**, 174507 (2001), publisher: American Physical Society.

[331] P. A. Volkov, J. H. Wilson, and J. H. Pixley, arXiv:2012.07860 [cond-mat] (2020), arXiv: 2012.07860.

[332] P. A. Volkov, S. Y. F. Zhao, N. Poccia, X. Cui, P. Kim, and J. H. Pixley, arXiv:2108.13456 [cond-mat] (2021), arXiv: 2108.13456.

[333] X.-Y. Song, Y.-H. Zhang, and A. Vishwanath, arXiv:2109.08142 [cond-mat] (2021), arXiv: 2109.08142.

[334] Y. Zhu, M. Liao, Q. Zhang, H.-Y. Xie, F. Meng, Y. Liu, Z. Bai, S. Ji, J. Zhang, K. Jiang, R. Zhong, J. Schneeloch, G. Gu, L. Gu, X. Ma, D. Zhang, and Q.-K. Xue, Physical Review X **11**, 031011 (2021), publisher: American Physical Society.

[335] S. Y. F. Zhao, N. Poccia, X. Cui, P. A. Volkov, H. Yoo, R. Engelke, Y. Ronen, R. Zhong, G. Gu, S. Plugge, T. Tummuru, M. Franz, J. H. Pixley, and P. Kim, arXiv:2108.13455 [cond-mat] (2021), arXiv: 2108.13455.

[336] G. G. Naumis, Physics Letters A **380**, 1772 (2016).

[337] D. J. Thouless, Physical Review B **28**, 4272 (1983).

[338] Y. Morita and Y. Hatsugai, Physical Review Letters **86**, 151 (2001).

[339] H. Guo, E. Khatami, Y. Wang, T. P. Devereaux, R. R. P. Singh, and R. T. Scalettar, Physical Review B **97**, 155146 (2018).

[340] E. Fradkin, S. A. Kivelson, and J. M. Tranquada, Reviews of Modern Physics **87**, 457 (2015), publisher: American Physical Society.

[341] M. Christos, S. Sachdev, and M. S. Scheurer, Physical Review X **12**, 021018 (2022), publisher: American Physical Society.

[342] H. Zhou, L. Holleis, Y. Saito, L. Cohen, W. Huynh, C. L. Patterson, F. Yang, T. Taniguchi, K. Watanabe, and A. F. Young, Science **375**, 774 (2022), publisher: American Association for the Advancement of Science.

[343] X. Wang and O. Vafek, arXiv:2112.08620 [cond-mat] (2021), arXiv: 2112.08620.

[344] Y. Sheffer and A. Stern, arXiv:2106.10650 [cond-mat] (2021), arXiv: 2106.10650.